RAMAN STUDIES OF
PHONON DISPERSION IN ZINCBLENDE SEMICONDUCTORS

by

JAMES LLOYD LA COMBE

B.Sc., University of Waterloo, 1965
M.Sc., University of Waterloo, 1966

A DISSERTATION SUBMITTED IN PARTIAL FULFILMENT

OF THE REQUIREMENTS FOR THE DEGREE OF

DOCTOR OF PHILOSOPHY

in the Department

of

Physics

SIMON FRASER UNIVERSITY

SEPTEMBER 1971

APPROVAL

Name: James Lloyd La Combe

Degree: Doctor of Philosophy

Title of Thesis: Raman Studies of Phonon Dispersion in Zincblende Semiconductors

Examining Committee:

Chairman: J.F. Cochran

J.C. Irwin
Senior Supervisor

K.E. Rieckhoff
Examining Committee

R.H. Enns
Examining Committee

K. Colbow
Examining Committee

A. Anderson
External Examiner
Associate Professor
University of Waterloo
Waterloo, Ontario

Date Approved: Sept 24/71

ABSTRACT

The first and second order Raman spectra of ZnSe, ZnTe, and GaP have been investigated. An analysis of the spectra has provided values for the phonon frequencies at the critical points X, L, and W in the Brillouin zone. In carrying out the analysis a theoretical model has been used and the values obtained for the critical point frequencies are consistent with both the experimental results and the theoretical model. The elastic constants have been used as constraints in the determination of the parameters used in the theoretical model. In addition, in the case of ZnSe only, Raman spectra were obtained for various crystal orientations and polarizations of the incident and scattered light. This enabled a comparison to be made between the assignments for ZnSe and group theoretical selection rules. In all cases the results were checked for consistency using the Brout sum rule and regularities previously observed in the phonon spectra of zincblende semiconductors.

The theoretical model has also been used to calculate the phonon frequencies throughout the Brillouin zone. The density of states has been further calculated from these dispersion curves and the results have been compared with information obtained from specific heat and neutron scattering measurements.

TABLE OF CONTENTS

LIST OF TABLES

LIST OF FIGURES

ACKNOWLEDGEMENTS

I wish to thank J. C. Irwin for his constant interest and close support of my work. It has been a pleasure working with him. I would like to acknowledge the excellent equipment which has been made available for my work and the friendliness and cooperation of the members of the faculty and staff of the department.

My thanks must go to V.P. Varshni of the University of Ottawa for supplying to me a copy of his computer program thus saving me a great deal of time and to Hugh Woollam for assisting me with the calculations.

Acknowledgement is made to the National Research Council for financial support in terms of a scholarship for three years, to the Department for several teaching assistantships, and to J. C. Irwin who also provided financial assistance through his grant.

CHAPTER 1

INTRODUCTION

At the present time the only direct means of obtaining the phonon dispersion curves throughout the Brillouin zone (B.Z.) of any material is by the method of neutron scattering. However this method is expensive both with respect to time and equipment. Also this method is not applicable to many materials because of unfavourable neutron-scattering cross-sections or the unavailability of sufficiently large single crystals on which to perform the experiment. This is particularly important for some II-VI and III-V compounds as large single crystals are as yet unavailable. To date only three zincblende materials have been investigated by neutron scattering. Waugh and Dolling (1963) measured the phonon dispersion of GaAs. GaP was studied by Yarnell et al. (1968) and ZnS by Feldkamp, Venkataraman and King (1969). For ZnS, the experimenters had to work with rather small crystals with a volume of about 1.5 cc and in fact the GaP sample investigated was fabricated by gluing together oriented single crystal platelets. For these reasons it is desireable to have an alternate means of obtaining phonon dispersion curves. Several approaches have been used in the past and the various experimental methods are described briefly in Chapter 2.

This work describes an attempt to deduce the phonon dispersion curves for some zincblende semiconductors from a study of the Raman spectra of these materials.

A study of the lattice vibrations of zincblende com-

pounds is also inherently attractive because of their relatively simple crystal structure. This makes an interpretation of the Raman spectra easier than it would be for say wurtzite materials and thus facilitates the comparison of experimental data with the theoretical models which can be applied to the results. In addition a large number of crystals, both semiconducting and insulating, possess this crystal structure.

This work presents a study of the first and second order Raman spectra of these materials: ZnTe, a p-type II-VI semiconductor; ZnSe, an n-type II-VI semiconductor; and GaP an n-type III-V semiconductor. In the past the lattice vibrations and infra-red properties of these materials have been studied by several workers using the techniques of infra-red absorption(a). However, due to the advent of lasers and modern detection methods, Raman scattering now provides an alternate technique which yields additional and complementary information to that obtained from infra-red measurements. In particular the first-order Raman effect gives the values of the phonon vibrational mode frequencies at the B.Z. centre and the second-order Raman effect should provide information on the values of the phonon frequencies at other points of the Brillouin zone.

(a) I.R. studies of ZnTe: Nahory and Fan (1967), Narita et al. (1967) and Riccius (1968); ZnSe, Riccius (1968), Aven et al. (1961) and Mitra (1963); GaP, Barker (1968), Kleinman and Spitzer (1960) and Fray et al. (1969).

The previous Raman experiments on the compounds investigated here have been qualitative in nature and little quantitative information has been obtained. In particular the Raman scattering experiments carried out on both ZnTe and ZnSe (Taylor, 1967, Ushioda et al., 1967, Krauzman, 1967) were devoted to the first order spectrum and a detailed investigation of the second order Raman spectrum was not carried out. The second order spectra of ZnSe has been observed by Krauzman (1969) and Nilsen (1969) but no serious attempt was made to analyse their results and no definitive results were obtained.

The second order Raman spectrum of GaP has undergone the most thorough investigation (Hobden and Russel, 1964 and Russel, 1965). Hobden and Russel were the first experimenters to use a laser as the source for a measurement of first and second order Raman spectra of any crystal. These workers have made assignments to the observed Raman features to be consistent with a chosen set of frequencies at the critical points X, L and W on the B.Z. boundary. The infra-red absorption spectrum of GaP has also been observed (Kleinman and Spitzer, 1960) and a similar analysis made. There is, however, considerable disagreement between these results. The second order Raman spectrum of GaP is again studied in this work, partly to clear up the above discrepancies but mainly to verify the method of analysis presented here by comparing these results to the measured neutron data for GaP.

In interpreting the features of a second order Raman spectrum of a zincblende material, a theoretical model intro-

duced by Banerjee and Varshni (1969) has been used in this work. This model incorporates the short range force model of Smith (1948) to second nearest neighbours and the long range Coulomb force model of Kellerman (1940). This model is referred to as the second neighbour ionic (S.N.I.) model. A set of frequencies is obtained for the zone boundary critical points X, L and W. These frequencies are chosen to fit both the experimental Raman spectrum and the theoretical model using the measured elastic constants as a constraint on the model parameters. A description of the theoretical model is given in Chapter 3.

In the case of ZnSe it has also been possible to investigate the Raman spectrum of ZnSe with regard to its polarization characteristics. The polarization characteristics of the observed Raman features can be compared with the polarizations predicted from group theory. This method of analysing the Raman spectra of zincblende materials has been previously applied to ZnS by Krauzman (1969) and Nilsen (1969a) and is outlined in Chapter 4.

A set of S.N.I. model parameters has been obtained from the analysis of the Raman spectra of ZnTe, ZnSe, GaP and ZnS (Irwin, 1970) and the results are presented in Chapter 6.

The consistency of the frequency assignments is checked in Chapter 7 using the Brout sum rule (Mitra, 1963) and regularities previously observed in the phonon spectra of zincblende semiconductors (Mitra, 1963; Keyes, 1962; and Marshall and Mitra, 1964).

Using the S.N.I. model parameters obtained, the phonon dispersion of ZnTe, ZnSe, ZnS and GaP has been calculated throughout the entire Brillouin zone with the aid of a high speed electronic computor. In addition, the frequency distribution function and specific heats have been calculated and a comparison has been made with the measured values of the specific heat of these materials. For GaP and ZnS, where neutron results are available, a direct comparison of the phonon branches has been made. These results are presented in Chapter 8.

Chapter 9 contains a summary of the results, conclusions, and suggestions for further work.

CHAPTER 2

EXPERIMENTAL METHODS

2.1 Introduction

In the past several experimental methods have been used to obtain information about the vibrational spectra of solids. The methods used differ greatly in their ease of application, expense, and type and amount of information that they provide. The basic principles involved in these experiments and the chief advantages and disadvantages are briefly reviewed in this chapter.

2.2 Thermodynamic Measurements

The early measurements of specific heat were of great importance to the development of lattice dynamics. They showed the inadequacy of the Einstein model, leading to the Debye and Born-Kármán models and later to the lattice models of Blackman (1937), Kellerman (1940) and Smith (1948).

The specific heat, however, depends only on an integral over the frequency distribution, $g(\nu)$, of the vibrational modes of a crystal and thus only provides information about the average of phonon spectrum, and does not tell one about individual modes. Therefore, a detailed study of the phonon dispersion cannot be based on specific heat data.

2.3 Ultrasonic Measurements

The long wavelength acoustic vibrational modes of a solid can be excited by ultrasonic techniques. Longitudinal or transverse elastic waves are excited by a transducer at frequencies up to about 10^{10} Hz and the velocity of the disturbance is determined by measuring the time taken by a pulse to cross a sample crystal. The results provide the slope of the appropriate dispersion curves at long wavelengths and are usually expressed in terms of the elastic constants.

Unfortunately transducers are limited in operation to frequencies $\lesssim 10^{10}$ Hz and thus only the acoustic phonons with small energies near the B.Z. centre can be investigated by this method. Huntington (1958) has given a review of the experimental technique and of many results obtained by ultrasonic measurements.

2.4 X-ray Scattering

X-ray wavelengths are typically about 1 Ångstrom and thus the momentum of an X-ray quantum is comparable to that of phonons in crystals; however, X-ray energies (10 keV) are many times greater than the phonon energies (10 meV) and the energy change on scattering cannot be detected directly. The frequencies of the phonons are obtained by measuring the scattered intensity and comparing it with theoretical expressions for the cross-section (Cochran, 1966). Corrections must be made for Compton scattering and for the scattering by multi-phonon processes. The experiment and analysis are difficult and become more so for crystals with many atoms per unit cell.

Some successful experiments have been performed however, for example, on aluminum (Walker, 1956), and on alkali halides (Buyers and Smith, 1966; Iveronova et al., 1967) but to date no such experiments have been carried out on zincblende materials.

2.5 Neutron Scattering

A direct measurement of the phonon dispersion in crystals is provided by neutron scattering. Thermal neutrons from a reactor have wavelengths and energies about equal to the lattice spacing and vibrational frequencies respectively and the energy change and scattering angle can be measured to provide the frequency and wavevector of the scattering phonon. This makes neutron scattering the most powerful experimental method for the study of phonon dispersion in crystals.

The phonon spectrum is determined by measuring the one-phonon coherent scattering from single crystals. This is done by allowing neutrons of a particular energy to be incident on the specimen and observing the energy of those scattered through a particular angle. One method of doing this is to use a triple-axis crystal spectrometer which was largely developed at Chalk River by Brockhouse (1961).

A schematic diagram of a triple axis crystal spectrometer is shown in Figure 1. The neutrons from a reactor are incident on a single crystal monochromater (XI in Figure 1) and reflected to give a beam of neutrons of particular energy incident on the specimen S. The neutrons scattered from specimen S,

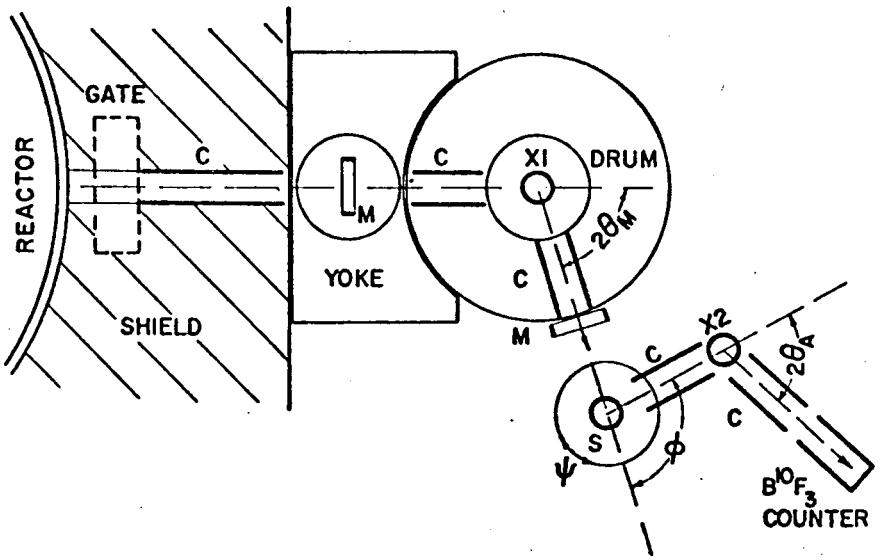

Figure 1. A schematic diagram of a triple-axis crystal spectrometer (Brockhouse, 1961).

are analysed with a second single crystal monochromater X2, and detected by a suitable neutron detector and counter. The parts marked M and C in Figure 1 are monitor counters and collimators, respectively.

Another method of measuring neutron scattering from crystals uses a time of flight technique. However, this technique will not be discussed here.(1) Both these methods have many drawbacks. The neutron beams are not intense and the scattered neutrons provide only about 10 counts per minute. Therefore a great deal of time and expensive equipment are needed adjacent to a neutron source such as a reactor in order to

---

(1) A discussion of time of flight technique and the determination of phonon spectra by neutron scattering has been given by Cowley (1969).

carry out the experiment. The energy resolution is not as good as can be obtained by optical techniques and large samples are required (typically about 50 cm^{-3}). Some materials are not suitable for this method because of high neutron absorption cross-section or too large an incoherent scattering cross-section (Cowley, 1969). For these reasons it is desirable to have alternative methods for obtaining the phonon dispersion of crystalline solids.

2.6 Optical Measurements

Optical methods include the measurement of the absorption and reflection of far infra-red radiation, Raman scattering and Brillouin scattering of light by phonons. In most cases the wavelength of the light used is more than 10^3 times greater than the lattice spacing. Consequently first order optical techniques are limited to momentum transfers which are very small compared to the momenta of most of the phonons. Brillouin scattering provides information about the acoustic phonons near $|\vec{q}| = 0$ whereas the other methods in first order provide measurements of the phonon energies in the optical branches near $|\vec{q}| = 0$.

It would appear that far infra-red absorption and Raman scattering measure the same frequencies; this, however, is not usually the case. Raman scattering depends on the modulation of the polarizability of the crystal by the phonons, whereas infra-red absorption depends on the dipole moment. The symmetry of the polarizability tensor and the dipole moment usually differ and therefore different phonons contribute to the two processes.

The two methods tend to be complimentary, for example, the first order optic modes of alkali halides can be studied by infra-red but not Raman techniques, while for diamond the situation is reversed.

To obtain information on the vibrational frequencies at other points in the B.Z. the second order infra-red and Raman spectra of crystals must be examined. Conservation of momentum requires that the wavevectors of the contributing phonons be approximately equal in magnitude and opposite in direction. The presence of sharp features in the second order spectrum are assumed to be due to critical points in the B.Z. and an interpretation of observed spectra can be made accordingly. In addition an analysis of the symmetry properties of the critical points and the polarization properties of the observed Raman feature allows, in principle, a good deal of information to be obtained about the phonon dispersion of crystals. This latter point will be discussed in more detail in Chapter 4.

Optical techniques are one of the most accurate methods of obtaining information about phonon dispersion and one of the most generally available. In addition there are essentially no restrictions on crystal size, or type, other than that the crystal transmit a portion of the exciting light.

CHAPTER 3

THE LATTICE DYNAMICS OF ZINCBLENDE

3.1 Introduction

In recent years a great deal of effort has been expended by many workers in an effort to obtain a satisfactory theoretical model for the lattice vibrational spectra of compounds which crystallize in the zincblende structure. This work has been stimulated in part by the ever increasing availability of relevant experimental data on these compounds; in addition, many compounds crystallize in this structure and the results of a theoretical calculation would have many applications.

3.2 Theoretical Models

The theoretical models which have been employed in an attempt to explain the lattice vibrational frequencies observed in zincblende materials can be broadly classified in three catagories: (a) conventional force constant models (Born-Kármán, 1912, and Smith, 1948); (b) rigid ion models (Kellerman, 1940; Born and Huang, 1954; Merten, 1958 and 1962); (c) dipole approximation model (Tolpygo, 1961 and Mashkevich and Tolpygo, 1957) and the largely equivalent shell model (Dick and Overhauser, 1958; Cochran, 1959 and Cowley, 1962).

In the Born-Kármán theory of lattice dynamics the motion of the nuclei is determined by an effective potential which depends only on the nuclear coordinates. The electrons

are regarded simply as a medium for exerting internuclear forces, and the wave function of the electrons is taken to be the same at any instant as if the nuclei continually occupied their instantaneous positions(adiabatic approximation). This conventional force constant model has been applied to the diamond-type lattice of germanium to fit the measured disperion curves for that material(Pope, 1965). It was found that in order to fit the data, interactions out to at least fifth neighbours had to be included and that the values deduced for most of the force constants were not statisically significant. Although this model has not been applied to zincblende materials it is felt that such a fit would be of no more significance than for germanium.

In the rigid ion model the ions are assumed to be spherical and rigid meaning that they are not polarizable or deformable, so that regards their Coulomb interaction the ions are equivalent to point charges. The motion of the ions is determined by long range Coulomb forces which extend throughout the crystal. The application of the rigid ion model to zincblend by Merten(1958) has been rather unsuccessful (since the bonding in the zincblende structure is only partially ionic) and is not capable of correlating the large range of available experimental information (Kaplan and Sullivan, 1963).

The shell model is an extention of the Born-Kármán theory of lattice dynamics in which each atom is no longer rigid but is regarded as a charged core consisting of the nucleus and

inner electrons and an oppositely charged shell representing the other electrons. The shell and core are coupled to one another by an isotropic force constant, and each retains spherical symmetry although a dipole moment may be generated by their relative displacements. The shell model thus allows the atom the property of polarizability in an electric field, and of "distortion polarizability" under the influence of short-range forces acting through both cores and shells.

The shell model has been applied to several zincblende materials by Kaplan and Sullivan (1963) using eleven different parameters. They found that it was impossible to get a unique set of parameters to describe the experimental results and concluded that the shell model was too flexible to be of great use in zincblende compounds. Also the "simple" shell model, utilizing only three or four parameters, almost invariably failed to give even an approximate phonon dispersion relation for zincblende crystals (Vetelino and Mitra, 1969). In cases where the shell model has given good agreement with the neutron-scattering data, e.g. GaAs (Waugh and Dolling, 1963) and GaP (Yarnell et al., 1968), the model has employed a large number of parameters which do not have any more physical significance than that of fitting constants to an interpolation formula.

If one wishes to calculate the phonon dispersion in zincblende from restricted information it is necessary to have a

lattice dynamic model limited to a few physically significant parameters. The above models are not suitable for this purpose. Recently, however, a combined force constant and rigid ion model has been introduced. This model has relatively few parameters and these are physically significant. Hence the model lends itself to the purpose of this thesis. The model is called the S.N.I. model and is discussed in the remainder of this chapter.

3.3 The S.N.I. Model

The S.N.I. model was introduced by Banerjee and Varshni (1969) and has been applied to both, III-V zincblende compounds (Banerjee and Varshni, 1969) and II-VI zincblende compounds (Irwin and LaCombe, 1970a and 1970b). The binding in zincblende semiconductors is known to be partially ionic and it is therefore reasonable that the S.N.I. model assign an effective charge e_s^* to the ions. The value of e_s^* for diatomic crystals is defined in terms of experimentally determined quantities by the following relation first derived by Szigeti (1949),

$$\epsilon_s = \epsilon_\infty + \frac{4\pi N(e_s^*)^2}{\mu \omega_t^2} \left(\frac{\epsilon_\infty + 2}{3} \right)^2 \qquad (3.1)$$

where N is the number of ion pairs per unit volume, μ is the reduced mass of an ion pair, $\omega_t/2\pi$ is the experimentally observed transverse resonance absorption frequency, and ϵ_s and ϵ_∞ are the static and optical dielectric constants respectively.

In the S.N.I. model the forces in the crystal are assumed to arise from two contributions: (a) short range forces

described by a conventional force constant model up to and including second neighbours (Smith, 1948) and (b) a long range force due to Coulomb interactions between the ionic charges (Kellerman, 1940). Combining these two forces and taking into account the symmetry of the crystal structure enables one to calculate the elements of the dynamical matrix. This matrix can be diagonalized to obtain the normal mode frequencies of the lattice.

The application of the S.N.I. model to the zincblende lattice is described in detail in section 3.5. As a first step it is necessary to review the structure and geometry of the zincblende type lattice. This is done in the next section.

3.4 The Zincblende Structure

(a) The direct lattice. The III-V and II-VI compounds studied here can be grown in the zincblende structure. This is a two component diamond structure, or rather, two face-centred cubic lattices with, for example, one lattice containing zinc atoms and the other tellurium atoms. The cube side has a length 2a and the two sublattices are displaced from each other along and equal to one quarter of the body diagonal ($\sqrt{3}\,a/2$). This structure is illustrated in Figure 2. The unit cell is a rhombohedral parallelepiped defined by the three basis vectors

$$\vec{a}_1 = a\hat{j} + a\hat{k}$$
$$\vec{a}_2 = a\hat{i} + a\hat{k}$$
$$\vec{a}_3 = a\hat{i} + a\hat{j}$$

The volume of the unit cell is $v_a = |\vec{a}_1 \times \vec{a}_2 \cdot\cdot \vec{a}_3| = 2a^3$

and contains one atom of each element.

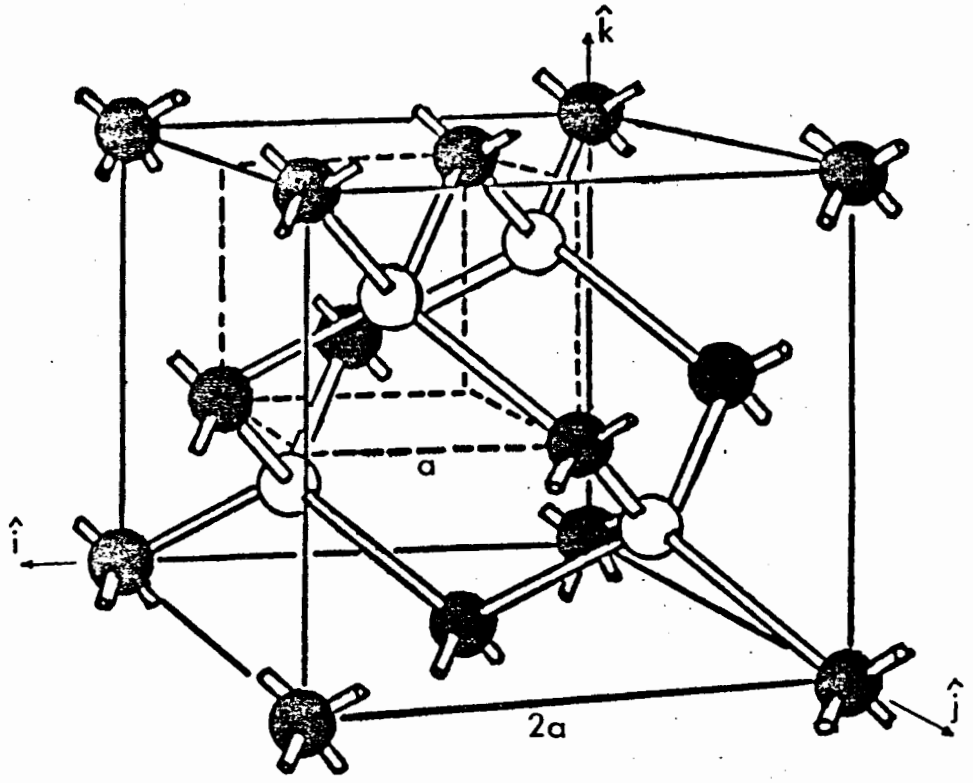

Figure 2. The zincblende lattice structure.

In Figure 2 the lattice structure of zincblende has been drawn so that lattice 1 contains the lighter atoms (black) and lattice 2 contains the heavier atoms (white). The atoms of lattice 1 are located by

$$\vec{r}\begin{pmatrix} \ell \\ 1 \end{pmatrix} = a\left[(\ell_1+\ell_3)\hat{\imath} + (\ell_1+\ell_2)\hat{\jmath} + (\ell_2+\ell_3)\hat{k} \right]$$

where ℓ_1, ℓ_2, ℓ_3 are integers, or one can write correspondingly,

$$\vec{r}\begin{pmatrix} \ell \\ 1 \end{pmatrix} = a(\ell_x, \ell_y, \ell_z)$$

where $\sum \ell_x = 2N$ (N is an integer). Lattice II can be generated by displacing the first lattice through a displacement $\vec{r}_{12}$ where

$$\vec{r}_{12} = -\frac{a}{2}(\hat{i}+\hat{j}+\hat{k})$$

The location of the atoms of lattice II are given by

$$\vec{r}\begin{pmatrix} l \\ 2 \end{pmatrix} = \vec{r}\begin{pmatrix} l \\ 1 \end{pmatrix} - \frac{a}{2}(\hat{i}+\hat{j}+\hat{k})$$

$$= a\left[(l_1+l_3-\tfrac{1}{2})\hat{i} + (l_1+l_2-\tfrac{1}{2})\hat{j} + (l_2+l_3-\tfrac{1}{2})\hat{k}\right]$$

We can also write this as

$$\vec{r}\begin{pmatrix} l \\ 2 \end{pmatrix} = a(m_x, m_y, m_z)$$

where $\sum m_x = 2N - 3/2$. The second lattice is taken as displaced in the negative direction so as to conform with the description of other authors (Kellerman, 1940; Cochran, 1959; Merten, 1959 and Banerjee and Varshni, 1969).

(b) The reciprocal lattice. The reciprocal lattice vectors corresponding to the basis vectors of the direct lattice are given by

$$\vec{b}_1 = \frac{1}{2a}(-\hat{i}+\hat{j}+\hat{k})$$
$$\vec{b}_2 = \frac{1}{2a}(\hat{i}-\hat{j}+\hat{k})$$
$$\vec{b}_3 = \frac{1}{2a}(\hat{i}+\hat{j}-\hat{k})$$

The reciprocal lattice vectors corresponding to the lattice points in the direct lattice are given by

$$\vec{b}_h = \frac{1}{2a}\left[(h_2+h_3-h_1)\hat{i} + (h_3+h_1-h_2)\hat{j} + (h_1+h_2-h_3)\hat{k}\right]$$

$$= \frac{1}{2a}(h_x, h_y, h_z)$$

where h_x, h_y, h_z are either all odd or all even integers. Any vector in reciprocal space can be expressed as

$$\begin{aligned}\vec{q} &= \vec{q}_1\vec{b}_1 + \vec{q}_2\vec{b}_2 + \vec{q}_3\vec{b}_3 \\ &= \frac{1}{2a}\left[(q_2+q_3-q_1)\hat{i} + (q_3+q_1-q_2)\hat{j} + (q_1+q_2-q_3)\hat{k}\right] \\ &= \frac{1}{2a}\,(q_x, q_y, q_z).\end{aligned}$$

where q_x, q_y, q_z are the reduced recrocal lattice coordinates.

The first Brillouin zone for the $\vec{q}$-space of the zincblende lattice is illustrated in Figure 3. The boundaries are given by the equations

$$q_x \pm q_y \pm q_z = \pm\frac{3}{2} \;;\; q_x = \pm 1 \;;\; q_y = \pm 1 \;;\; q_z = \pm 1 \qquad (3.3)$$

The symmetry points

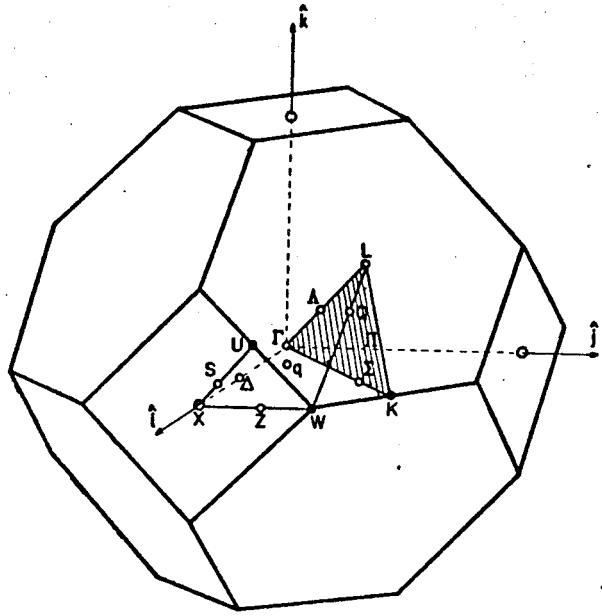

Figure 3. The first Brillouin zone of the zincblende reciprocal lattice.

marked in Figure 3 are expressed in terms of the reduced reciprocal lattice coordinates (q_x, q_y, q_z) in Table I along with the group representation for each point and the number of such points in the Brillouin zone. In Figure 3 q is an arbitrary point, π is a point in the plane defined by $\Gamma\Lambda LK\Sigma$ and the other points are clear from the figure. Although they have been given different designations in Figure 2, points U and K have the same symmetry properties; ξ, h_1, h_2 and h_3 are numbers with values from 0 to 1.

TABLE I

The Symmetry Points of the Reciprocal Lattice of Zincblende.

Symmetry Point	Position (q_x, q_y, q_z)	Group Representation	Number of Points in B.Z.
Γ	(0,0,0)	T_d	1
L	$(\frac{1}{2},\frac{1}{2},\frac{1}{2})$	C_{3v}	4
X	(1,0,0)	D_{2d}	3
W	$(1,\frac{1}{2},0)$	S_4	6
K=U	(3/4,3/4,0)	C_s	12
Λ	(ξ,ξ,ξ)	C_{3v}	4
Δ	$(\xi,0,0)$	C_{2v}	6
Σ	$3/4(\xi,\xi,0)$	C_s	12
Z	$(1,\xi/2,0)$	C_2	12
S	$(1,\xi/4,\xi/4)$	C_s	12
π	(h_1,h_1,h_3)	C_s	12
Q	$\frac{1}{2}(1+\xi,1,1-\xi)$	C_1	24
q	(h_1,h_2,h_3)	C_1	48

3.5 Description of the S.N.I. Model

(a) Equations of motion of a crystalline lattice. Consider small arbitrary displacements, $\vec{u}\,(_{\kappa})$, of the ions from equilibrium where $\kappa = 1, 2$ labels the type of ion. The potential energy of the deformed lattice can be expanded in powers of these displacements. The linear term of this expansion vanishes in equilibrium and the second order term is

$$\Phi_2 = \frac{1}{2} \sum_{l\kappa} \sum_{l'\kappa} \sum_{ij} \Phi_{ij} \begin{pmatrix} l\, l' \\ \kappa\, \kappa' \end{pmatrix} u_i \begin{pmatrix} l \\ \kappa \end{pmatrix} u_j \begin{pmatrix} l' \\ \kappa' \end{pmatrix}$$

where $$\Phi_{ij} \begin{pmatrix} l\, l' \\ \kappa\, \kappa' \end{pmatrix} = \left[\frac{\partial^2 \Phi}{\partial x_i \begin{pmatrix} l \\ \kappa \end{pmatrix} \partial x_j \begin{pmatrix} l' \\ \kappa' \end{pmatrix}} \right]_0$$

$$(i, j = 1, 2, 3)$$

and $x_i(^{l}_{\kappa})$ are the rectangular components of $\vec{u}(^{l}_{\kappa})$. In the harmonic approximation higher order terms in the expansion of Φ are neglected. Φ_{ij} is the dynamical matrix representing the force constants between the ions in the lattice.

The equation of motion of an ion of type κ and mass m_κ is given by

$$m_\kappa \ddot{u}_i \begin{pmatrix} l \\ \kappa \end{pmatrix} + \sum_{l'\kappa'} \sum_{j} \Phi_{ij} \begin{pmatrix} l-l' \\ \kappa\, \kappa' \end{pmatrix} u_j \begin{pmatrix} l' \\ \kappa' \end{pmatrix} = 0 \qquad (3.4)$$

For an independent normal vibration of the lattice this equation has plane wave solutions of the form

$$\vec{u} \begin{pmatrix} l \\ \kappa \end{pmatrix} = \frac{\vec{V}(\kappa)}{\sqrt{m_\kappa}}\, e^{i\omega t}\, e^{i \vec{q} \cdot \vec{r} \begin{pmatrix} l \\ \kappa \end{pmatrix}}$$

then the equation of motion can be written as

$$\omega^2 V_i(\kappa) - \sum_{\kappa'} \sum_{j} C_{ij}\begin{pmatrix}\vec{q}\\ \kappa\kappa'\end{pmatrix} V_j(\kappa') = 0 \qquad (3.5)$$

where

$$C_{ij}\begin{pmatrix}\vec{q}\\ \kappa\kappa'\end{pmatrix} = \frac{1}{\sqrt{m_\kappa m_{\kappa'}}} \Phi_{ij}\begin{pmatrix}l\\ \kappa\kappa'\end{pmatrix} e^{-i\vec{q}\cdot\vec{r}\binom{l}{\kappa}} \qquad (3.6)$$

are the elements of the dynamical matrix in reciprocal space. The equation of motion (3.5) for a wavevector $\vec{q}$ in the reciprocal space of the lattice are a set of six homogeneous equations in the amplitudes $V_i(\kappa)$. The necessary and sufficient condition that this set should have a non-trivial solution is that

$$\left| \omega^2 \delta_{ij}\,\delta_{\kappa\kappa'} - C_{ij}\begin{pmatrix}\vec{q}\\ \kappa\kappa'\end{pmatrix} \right| = 0 \qquad (3.7)$$

In the case of the S.N.I. model the dynamical matrix, $C_{xy}(_{\kappa\,\kappa'}^{\vec{q}})$, is made up of two parts, a short range part ${}^{sr}C_{xy}(_{\kappa\,\kappa'}^{\vec{q}})$ and a long range Coulomb part ${}^{c}C_{xy}(_{\kappa\,\kappa'}^{\vec{q}})$ such that

$$C_{xy}\begin{pmatrix}\vec{q}\\ \kappa\kappa'\end{pmatrix} = \frac{1}{\sqrt{m_\kappa m_{\kappa'}}} \left({}^{sr}C_{xy}\begin{pmatrix}\vec{q}\\ \kappa\kappa'\end{pmatrix} - {}^{c}C_{xy}\begin{pmatrix}\vec{q}\\ \kappa\kappa'\end{pmatrix} \right) \qquad (3.8)$$

(b) Short range forces. From the symmetry of the lattice it may be shown (Merten, 1958) that the force constant matrix for the first neighbours is

$$\begin{bmatrix} \alpha & \beta & \beta \\ \beta & \alpha & \beta \\ \beta & \beta & \alpha \end{bmatrix}$$

and for the second nearest neighbours, assuming central forces (Smith, 1948, and Braunstein, Herman and Moore, 1958)

$$\begin{bmatrix} \lambda_\kappa & 0 & 0 \\ 0 & \mu_\kappa & \mu_\kappa \\ 0 & \mu_\kappa & \mu_\kappa \end{bmatrix}$$

where $\kappa = 1, 2$ labels the type of ion. In terms of these force constants the short range parts of the dynamical matrices are given in q_x, q_y, q_z space by

$$^{sr}C_{xx}(\vec{q}_{\kappa\,\kappa}) = 4\,[\alpha+\lambda_\kappa\{1-\cos\pi q_y\cos\pi q_z\} + \mu_\kappa\,\{2-\cos\pi q_x\cos\pi q_y - \cos\pi q_x\cos\pi q_z\}]$$

$$^{sr}C_{xy}(\vec{q}_{\kappa\,\kappa}) = 4[\mu_\kappa \sin\pi q_x \sin\pi qy] = {}^{sr}C_{yx}(\vec{q}_{\kappa\,\kappa})$$

$$^{sr}C_{xx}(\vec{q}_{\kappa\,\kappa'}) = -\alpha[\exp\pi i/2(q_x+q_y+q_z) + \exp\pi i/2(q_z-q_x-q_y) + \exp\pi i/2(q_y-q_x-q_z) + \exp\pi i/2(q_x-q_y-q_z)]$$

$$^{sr}C_{xy}(\vec{q}_{\kappa\,\kappa'}) = -\beta[\exp\pi i/2(q_x+q_y+q_z) + \exp\pi i/2(q_z-q_x-q_y) - \exp\pi i/2(q_y-q_x-q_z) - \exp\pi i/2(q_x-q_y-q_z)] = {}^{sr}C_{yx}(\vec{q}_{12})$$

The remaining elements are obtained by a cyclic permutation of the indices and by using the fact that

$$C_{xy}\begin{pmatrix}\vec{q}\\ 2\,1\end{pmatrix} = C^{*}_{xy}\begin{pmatrix}\vec{q}\\ 1\,2\end{pmatrix}$$

where $C^{*}_{xy}\begin{pmatrix}\vec{q}\\ 1\,2\end{pmatrix}$ is the hermitian conjugate of $C_{xy}\begin{pmatrix}\vec{q}\\ 1\,2\end{pmatrix}$.

(c) Long range forces. The effective contribution of the long range forces to the dynamical matrixes were obtained by Kellerman (1940) for the NaCl lattice. Cochran (1959) has applied this theory to the diamond lattice and it has been extended to zincblende by Banerjee and Varshni (1969).

From Cochran's paper (1959), the elements of the dynamical matrix of the long range forces due to Coulomb interaction of the ions in the lattice are given by

$$^{c}C_{xy}\begin{pmatrix}\vec{q}\\ 11\end{pmatrix} = Z^2e^2 \lim_{\vec{r}\to 0}\left[\sum_{\ell}{}' \frac{\partial^2 \exp(i\vec{q}.\vec{r}_{\ell})}{\partial x \partial y\,|\vec{r}-\vec{r}_{\ell}|}\right]$$

and

$$^{c}C_{xy}\begin{pmatrix}\vec{q}\\ 12\end{pmatrix} = -Z^2e^2\{\exp(i\vec{q}.\vec{r}_{12})\} \lim_{\vec{r}\to -r_{12}}\left[\sum_{\ell} \frac{\partial^2 \exp(i\vec{q}.\vec{r}_{\ell})}{\partial x \partial y\,|\vec{r}-\vec{r}_{\ell}|}\right]$$

where $\vec{r}_{\ell} = \vec{r}\begin{pmatrix}\ell\\ 1\end{pmatrix}$ and Ze is the effective charge of the ion.

If one takes into account the structure of the zincblende lattice, the elements of the Coulomb dynamical matric $^{c}C_{xy}\begin{pmatrix}\vec{q}\\ \kappa\,\kappa'\end{pmatrix}$ are given by

$$(\nu_a/Z^2e^2)\,{}^{c}C_{xy}(\kappa^{\vec{q}}\kappa') = (4\pi/3)\,\delta_{xy} \quad \text{for } q = 0$$

and for $q \neq 0$ by

$$(\nu_a/Z^2e^2)\,{}^{c}C_{xy}(\kappa^{\vec{q}}\kappa) = -G_{xy}(\kappa\kappa) + H_{xy}(\ell) + (8/3\sqrt{\pi})\,\epsilon^3\delta_{xy}$$

and

$$(\nu_a/Z^2e^2)\,{}^{c}C_{xy}(\kappa^{\vec{q}}\kappa') = G_{xy}(\kappa\kappa) - H_{xy}(m)$$

where v_a is the volume of the unit cell and

$$G_{xy}(\kappa\kappa) = 4\pi\sum_{h}(h_x+q_x)(h_y+q_y)/(\vec{h}+\vec{q})^2\exp[-(\pi^2/4\epsilon^2)(\vec{h}+\vec{q})^2]$$

$$G_{xy}(\kappa\kappa') = 4\pi\sum_{h}(h_x+q_x)(h_y+q_y)/(\vec{h}+\vec{q})^2\exp[-(\pi^2/4\epsilon^2)(\vec{h}+\vec{q})^2 - (\pi i/2)(h_x+h_y+h_z)]$$

$$H_{xy}(\ell) = 2\sum_{\ell}[-f(\ell)\,\delta_{xy}+g(\ell)\ell_x\ell_y/\ell^2]\cos\pi(\vec{q}.\vec{\ell})$$

$$H_{xy}(m) = 2\sum_{m}[-f(m)\,\delta_{xy}+g(m)m_xm_y/m^2]\exp i\pi(\vec{q}.\vec{m})$$

$$f(\ell) = (2\epsilon/\ell^2\sqrt{\pi})\exp(-\epsilon^2\ell^2) + \psi(\epsilon\ell)/\ell^3$$

$$g(\ell) = 3f(\ell) + (4\epsilon^3/\sqrt{\pi})\exp(-\epsilon^2\ell^2)$$

$$\psi(\epsilon\ell) = 1-(2/\sqrt{\pi})\int_0^{\epsilon\ell}\exp(-t^2)dt$$

where ϵ is an arbitrary parameter and ℓ, m, q, h, are appropriate lattice and reciprocal lattice vectors.

The calculated values for $(2/\chi)^{c}C_{xy}(_{\kappa}{}^{\vec{q}}{}_{\kappa'})$ for the critical points X, L and W of the zincblende structure are listed in Table II.

(c) Dynamical matrix and elastic constants for S.N.I. model. The final dynamical matrix element is given by equation 3.8.

$$C_{xy}\left(\begin{smallmatrix}\vec{q}\\ \kappa\,\kappa'\end{smallmatrix}\right) = \frac{1}{\sqrt{m_\kappa m_{\kappa'}}}\left\{{}^{sr}C_{xy}\left(\begin{smallmatrix}\vec{q}\\ \kappa\,\kappa'\end{smallmatrix}\right) - {}^{c}C_{xy}\left(\begin{smallmatrix}\vec{q}\\ \kappa\,\kappa'\end{smallmatrix}\right)\right\}$$

The matrix is Hermitian and can be diagonalized to obtain the normal mode frequencies of the lattice at any point in the B.Z.:

$$\left|\omega^2\,\delta_{xy}\,\delta_{\kappa\kappa'} - C_{xy}\left(\begin{smallmatrix}\vec{q}\\ \kappa\,\kappa'\end{smallmatrix}\right)\right| = 0 \qquad (3.7)$$

In general this equation is a six by six complex determinant whose solution is not simple; however, at the critical points Γ, X, L and W, the determinant factors and relatively simple analytical solution are obtained. These solutions are given below in terms of the seven S.N.I. model parameters α, β, μ_1, μ_2, λ_1, λ_2, and χ.

TABLE II

The values of $(2/\chi)^{c}C_{xy}(_{\kappa}{}^{\vec{q}}{}_{\kappa'})$ in units of 10^3 dynes/cm for the critical points X, L and W.

$(2/\chi)^{c}C_{\alpha\beta}(_{1}{}^{\vec{q}}{}_{1})$	(1) X	(1) L	W
α β	(1,0,0)	$(\frac{1}{2},\frac{1}{2},\frac{1}{2})$	$(1,\frac{1}{2},0)$
1 1	4.330	3.615	-.790
2 2	2.160	3.615	1.568
3 3	2.160	3.615	-.790
1 2	.000	.000	.000
1 3	.000	.000	.000
2 3	.000	.000	.000

$(2/\chi)^{c}C_{\alpha\beta}(_{1}{}^{\vec{q}}{}_{2})$	(1) X	(1) L	W
α β	(1,0,0)	$(\frac{1}{2},\frac{1}{2},\frac{1}{2})$	$(1,\frac{1}{2},0)$
1 1	.000	.000	.000
2 2	.002	.000	.000
3 3	.002	.000	.000
1 2	.000	-4.947+4.947i	8.468
1 3	.000	-4.947+4.947i	.000
2 3	10.617i	-4.947+4.947i	-8.468i

(1) Merten, 1958.

At Γ,

$$\omega_{TO}^2 \ (\Gamma) = [(4\alpha - \frac{2\pi\chi}{3}) \ (\frac{1}{m_1} + \frac{1}{m_2})]$$

$$\omega_{LO}^2 \ (\Gamma) = [(4\alpha + \frac{4\pi\chi}{3}) \ (\frac{1}{m_1} + \frac{1}{m_2})]$$

At X,

$$\omega_{LO}^2 \ (X) = \frac{4}{m_1} [\alpha + 4\mu_1 + .54125\chi]$$

$$\omega_{LA}^2 \ (X) = \frac{4}{m_2} [\alpha + 4\mu_2 + .54125\chi]$$

$$\omega_T^2 \ (X) = \frac{U_1+U_2}{2} \pm \left[\frac{(U_1-U_2)^2}{2} + |X|^2\right]^{\frac{1}{2}}$$

Where

$$U_1 = \frac{4}{m_1} [\alpha + 2\lambda_1 + 2\mu_1 - 0.27\chi]$$

$$U_2 = \frac{4}{m_2} [\alpha + 2\lambda_2 + 2\mu_2 - 0.27\chi]$$

$$XX^* = (4\beta - 5.3085\chi)^2/(m_1 m_2)^{\frac{1}{2}}$$

At L,

$$\omega_L^2(L) = \frac{(U_1+U_2+2V_1+2V_2)}{2} \pm \left[\frac{(U_1-U_2+2V_1-2V_2)^2}{2} + (W+2X)^2\right]^{\frac{1}{2}}$$

$$\omega_T^2(L) = \frac{(U_1+U_2-V_1-V_1)}{2} \pm \left[\frac{(U_1-U_2-V_1+V_2)^2}{2} + (W-X)^2\right]^{\frac{1}{2}}$$

Where

$$U_1 = \frac{4}{m_1}(\alpha + \lambda_1 + 2\mu_1)$$

$$U_2 = \frac{4}{m_2}(\alpha + \lambda_2 + 2\mu_2)$$

$$V_1 = \frac{4}{m_1}(\mu_1 + .4519\chi)$$

$$V_2 = \frac{4}{m_2}(\mu_2 + .4519\chi)$$

$$W = -\alpha\sqrt{2}(1 - i)/(m_1m_2)^{\frac{1}{2}}$$

$$X = (\beta\sqrt{2} - 2.4735\chi)\ (1-i)/(m_1m_2)^{\frac{1}{2}}$$

At W,

$$\omega_1^2 = C_1$$

$$\omega_2^2 = C_2$$

$$\omega_{3,4}^2 = \frac{C_2 + D_1}{2} \pm \left[\left(\frac{C_2 + D_1}{2} \right)^2 - (C_2 D_1 - 2A^2) \right]^{\frac{1}{2}}$$

$$\omega_{5,6}^2 = \frac{C_1 + D_2}{2} \pm \left[\left(\frac{C_1 + D_2}{2} \right)^2 - (C_1 D_2 - 2A^2) \right]^{\frac{1}{2}}$$

Where

$$C_1 = \frac{4}{m_1} (\alpha + \lambda_1 + 3\mu_1 + 0.09874\chi)$$

$$C_2 = \frac{4}{m_2} (\alpha + \lambda_2 + 3\mu_2 + 0.09874\chi)$$

$$D_1 = \frac{4}{m_1} (\alpha + 2\lambda_1 + 2\mu_1 - 0.1960\chi)$$

$$D_2 = \frac{4}{m_2} (\alpha + 2\lambda_2 + 2\mu_2 - 0.1960\chi)$$

$$A = (2\sqrt{2}\beta - 4.2336\chi) / (m_1 m_2)^{\frac{1}{2}}$$

One can also deduce the relation between the coupling parameters of the model and the elastic constants of a crystalline material (Born and Huang, 1954). These calculations have been carried out by Blackman (1958) and the results, verified by Merten (1958) are given by

$$c_{11} = 0.1255\ Z^2e^2/2a^4 + (\alpha+4\mu_1+4\mu_2)/2a$$

$$c_{12} = -1.324\ Z^2e^2/2a^4 + \{2\beta-\alpha-2(\lambda_1+\lambda_2)+2(\mu_1+\mu_2)\}/2a$$

$$c_{44} = -0.063\ Z^2e^2/2a^4 + (1/2a)\{\alpha+2(\mu_1+\mu_2)+2(\lambda_1+\lambda_2)\}-A^2/B$$

where $$A = 2.519\ Z^2e^2/2a^5-\beta/a^2$$

and $$B = \frac{4\alpha-4\pi Z^2e^2/6a^3}{2a^3}$$

In the evaluation of ${}^{c}C_{xy}(\kappa\,\vec{q}\,\kappa')$ and the elastic constants the actual charge Ze is considered as a parameter and is represented by $\chi = Z^2e^2/a^3$. This gives a measure of the ionicity of the crystal.

The S.N.I. model can be fitted to the critical point frequencies deduced from the observed Raman scattering data using the equations for the normal mode frequencies at the critical points Γ, X, L, W. The elastic constants are used as a constraint of the values of the model parameters obtained

and therefore also constrain the assignments of the observed Raman features. The application of the S.N.I. model to the analysis of the Raman spectra of the zincblende materials studied in this work is found in Chapter 6.

In order to make the first tentative assignments to the features of an observed Raman spectrum it is necessary to know the processes contributing to these features. To this end the theory of Raman scattering in zincblende materials is reviewed briefly in Chapter 4. Since it desirable to compare the polarization characteristics of the observed Raman features with the polarizations predicted from group theory, the relavent group theory and method of analysis is also presented in the following Chapter.

CHAPTER 4

RAMAN SCATTERING IN ZINCBLENDE CRYSTALS

4.1 The Raman Effect

The Raman effect can be viewed quantum mechanically in the following way. Electromagnetic radiation of energy $\hbar\omega_i$, wave vector $\vec{k}_i$ and polarization vector $\hat{e}_i$ is incident on a crystal interacts with the electrons in the crystal through its polarizability, and a photon is absorbed, thereby exciting a transition from an initial electronic ground state to a virtual intermediate state. A second photon ($\hbar\omega_s$, $\vec{k}_s$, $\hat{e}_s$) is emitted with an accompanying transition from the virtual intermediate state back to the initial electronic ground state. At the same time there are accompanying changes in the vibrational states of the lattice and one or more phonons ($\hbar\Omega$, $\vec{q}$, $\hat{e}$) are created or destroyed (Burstein, 1964).

The mechanics of the Raman scattering process are illustrated in Figures 4 and 5. In Figure 5, n_e and n_ν designate the electronic and vibrational energy levels respectively, while n_j is the quantum mechanical occupation number of the phonon energy states of the crystal.

The requirement of conservation of energy and momentum are expressed for one phonon by

$$\vec{k}_i = \vec{k}_s \pm \vec{q} \qquad (3.1)$$

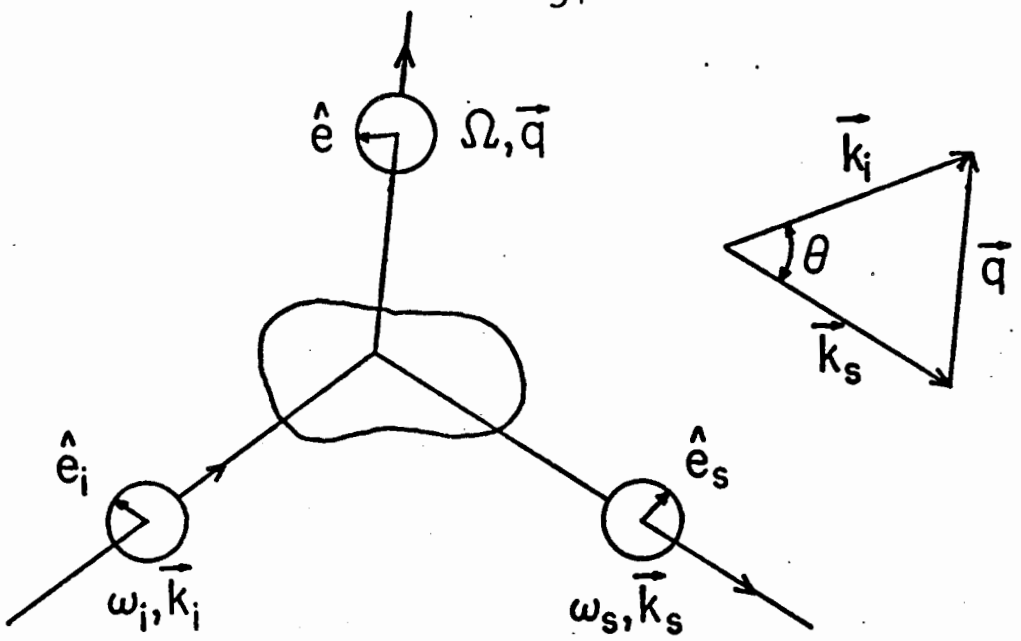

Figure 4. Raman scattering geometry and corresponding wave-vector diagram.

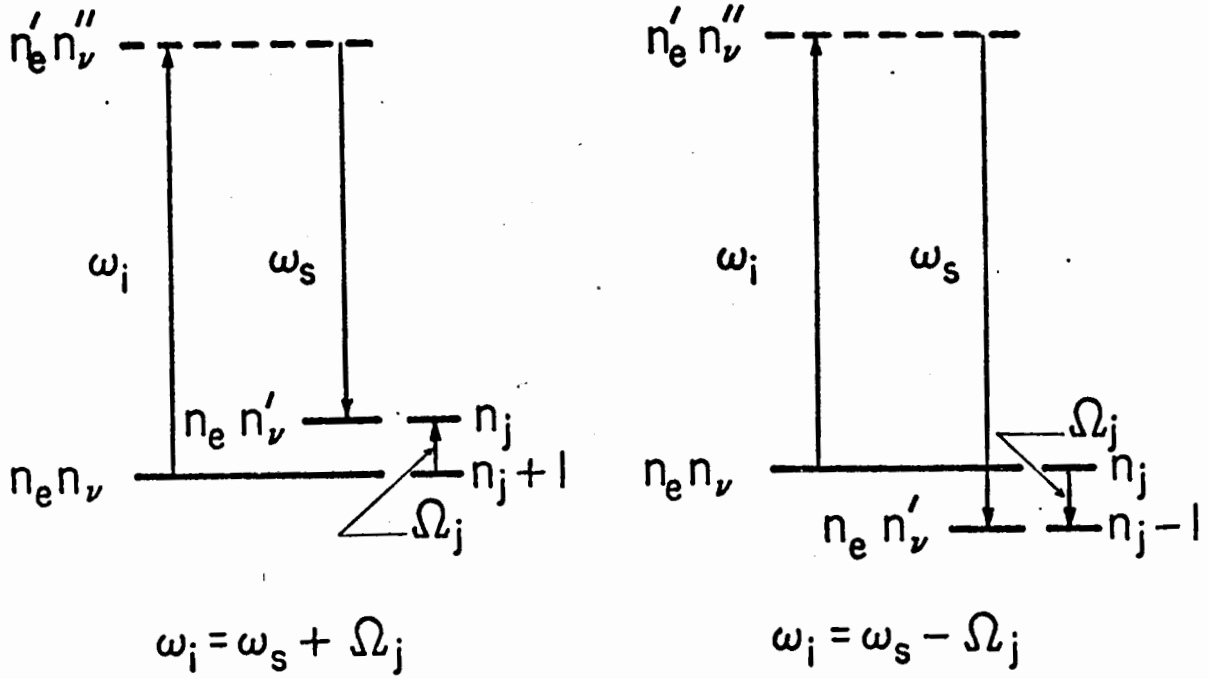

Figure 5. The electronic and vibrational transitions which occur in Stokes and anti-Stokes Raman scattering.

and $$\hbar\omega_i = \hbar\omega_s \pm \hbar\Omega \qquad (3.1)$$

where the + sign refers to the creation of a phonon and the - sign to the annihilation of a phonon. Since

$$\vec{k}_i \cong \vec{k}_s \ll \frac{1}{a}$$

then $$|\vec{q}| \simeq 0$$

This requires that the phonon created or destroyed in the Raman process must have a wavevector corresponding to a point near the Brillouin zone centre.

For two phonons

$$\vec{k}_i = \vec{k}_s \pm \vec{q}_1 \pm \vec{q}_2$$

$$\hbar\omega_i = \hbar\omega_s \pm \hbar\Omega_1 \pm \hbar\Omega_2 \qquad (3.2)$$

and again, since

$$\vec{k}_i \cong \vec{k}_s \ll \frac{1}{a}$$

then $$|\pm q_1 \pm q_2| \simeq 0$$

and the wavevector of the two phonons must be approximately equal in magnitude and opposite in direction.

The electric field of the incident radiation interacts directly with the electrons in the crystal and indirectly with the lattice via the electrons. The incident radiation can be characterized by $\vec{E}_i = \hat{e}_i E_i \exp\left[i\,(\vec{k}_i \cdot \vec{r} - \omega_i t)\right]$. This field when incident on the crystal induces a dipole moment $\vec{M}$ proportional to the polarizability tensor α_{ij} of the crystal.

$$M_i = \sum \alpha_{ij} E_j \qquad (3.3)$$

Scattered light is produced by re-radiation of energy by the induced dipole moment $\vec{M}$. The intensity depends on the state of polarization of the incident and scattered radiation and the electronic polarizability tensor:

$$I_s\ (W_s,\ \hat{e}_s) \propto \omega_s^4\ |\ \hat{e}_s \cdot \vec{\vec{d\alpha}} \cdot \hat{e}_i\ |\ E_i^2 \qquad (3.4)$$

where $\vec{\vec{d\alpha}}$ represents the change in $\vec{\vec{\alpha}}$ associated with the creation or destruction of the phonons. This change, $\vec{\vec{d\alpha}}$ can be written in terms of the ionic displacements (Loudon, 1964):

$$d\alpha_{ij} = \alpha_{ij} - \alpha_o = \frac{\partial \alpha_{ij}}{\partial u_k(q)}\, du_k(q) + \frac{\partial^2 \alpha_{ij}}{\partial u_k(q)\, \partial u'_\ell(q)}\, du_k(q)\, du'_\ell(q) + \cdots \qquad (3.5)$$

where $u_k(q)$, $u'_\ell(q)$ represents the displacement of the atoms and the subscripts indicate the vibrational branch. The first term on the right of equation (3.5) is responsible for first-order (or one-phonon) scattering, the second is responsible for second-order (or two-phonon) scattering, and so on.

The first-order polarizability coefficient $\frac{\partial \alpha_{ij}}{\partial u_k(q)}$, is a third-rank tensor, the non-zero components of which are determined by the symmetry of the phonons. These Raman tensors have been worked out for the symmetries of the vibrational modes which occur in zincblende by Loudon (1964) and are found in Table III. The tensor components are referred to the cubic crystallographic axes $\hat{i}$, $\hat{j}$ and $\hat{k}$ of Figure 2. The normal vibrations of the zincblende lattice which are Raman active are illustrated in Figure 6a. The normal mode vibrations with Γ_{15} symmetry species are also infrared active and the direction of polarization of each mode is indicated in brackets beside Γ_{15} in Figure 6a.

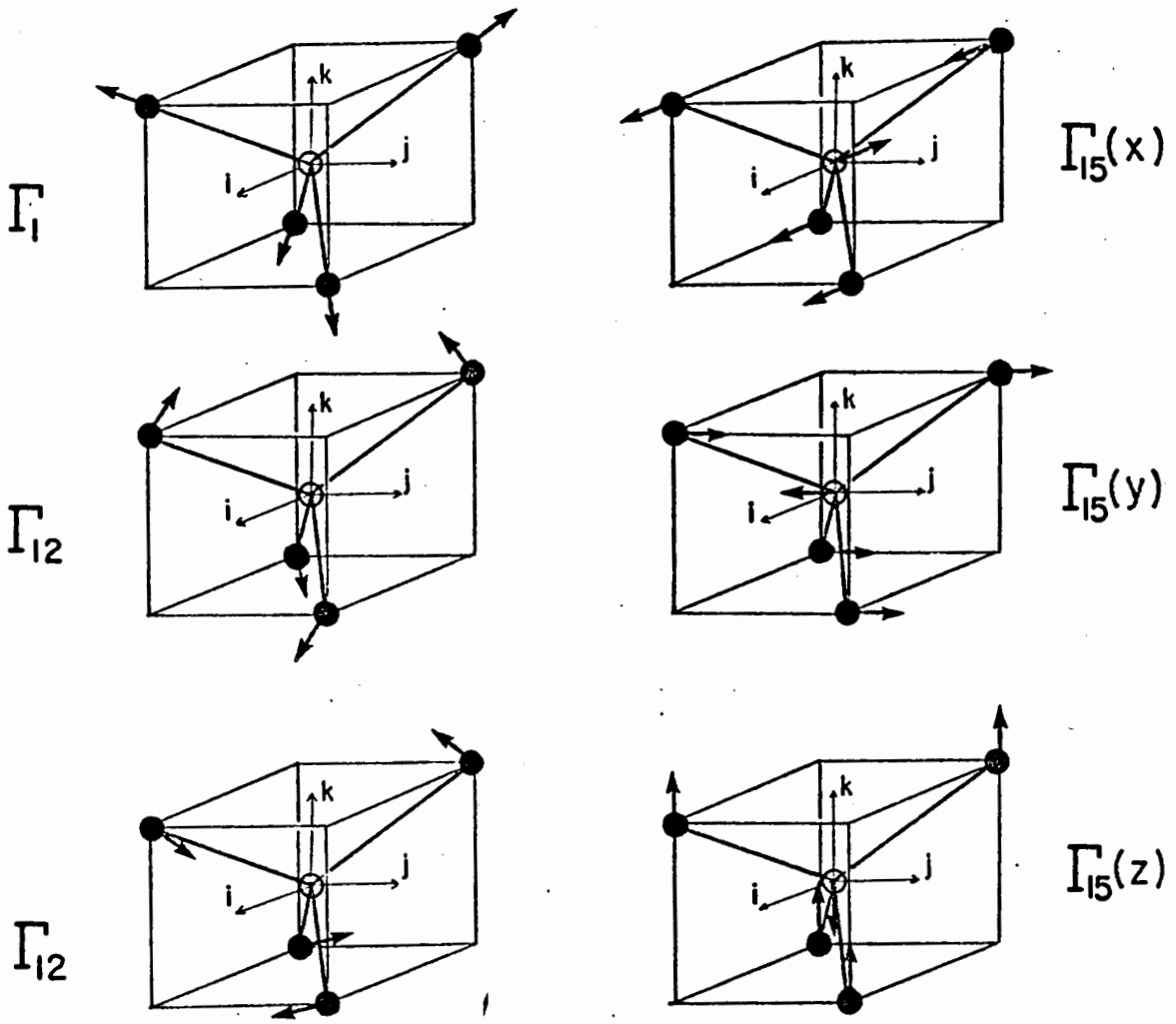

Figure 6a - Some normal modes of vibration for the tetrahedral molecule with T_d symmetry. The tetrahedral molecule has nine internal degrees of freedom and thus nine normal modes of vibration; however, only the six which are shown here participate in either first or second order Raman processes(Loudon,1964).

TABLE III

The Raman tensors for zincblende.

Irreducible Representation	Raman Tensor	Irreducible Representation	Raman Tensor
Γ_1 •••	$\begin{pmatrix} a & o & o \\ o & a & o \\ o & o & a \end{pmatrix}$	$\Gamma_{15}(x)$ •••	$\begin{pmatrix} o & o & o \\ o & o & d \\ o & d & o \end{pmatrix}$
Γ_{12} •••	$\begin{pmatrix} b & o & o \\ o & b & o \\ o & o & -2b \end{pmatrix}$	$\Gamma_{15}(y)$ •••	$\begin{pmatrix} o & o & d \\ o & o & o \\ d & o & o \end{pmatrix}$
Γ_{12} •••	$\begin{pmatrix} -\sqrt{3}b & o & o \\ o & -\sqrt{3}b & o \\ o & o & o \end{pmatrix}$	$\Gamma_{15}(z)$ •••	$\begin{pmatrix} o & d & o \\ d & o & o \\ o & o & o \end{pmatrix}$

4.2 The Temperature Dependence of Raman Processes

The scattering intensity of Raman processes are temperature dependent through the mean occupation number, $\bar{n}$, of the phonon states involved.

$$\bar{n}(\tilde{\nu}, T) = \frac{1}{e^{\frac{hc\tilde{\nu}}{kT}} - 1} \qquad (3.6)$$

where $\tilde{\nu}$ is the wave number $\tilde{\nu} = \frac{\nu}{c} = \frac{\omega}{2\pi c}$ of the phonon state, h is Planck's constant, c is the velocity of light, k is the Boltzman constant and T is the temperature. The temperature dependent factors for the various Raman processes are listed in Table IV for both Stokes and anti-Stokes radiation.

TABLE IV

The Temperature Dependence of Raman Processes.

Processes	Frequency	Stokes	Anti-Stokes
1st Order	$\tilde{\nu}$	$\bar{n}(\tilde{\nu},T)+1$	$\bar{n}(\tilde{\nu},T)$
Overtones	$2\tilde{\nu}_1$	$(\bar{n}(\tilde{\nu}_1,T)+1)^2$	$(\bar{n}(\tilde{\nu}_1,T))^2$
Sums	$\tilde{\nu}_1+\tilde{\nu}_2$	$(\bar{n}(\tilde{\nu}_1,T)+1)(\bar{n}(\tilde{\nu}_2,T)+1)$	$(\bar{n}(\tilde{\nu}_1,T))(\bar{n}(\tilde{\nu}_2,T))$
Differences	$\tilde{\nu}_1-\tilde{\nu}_2$	$(\bar{n}(\tilde{\nu}_1,T)+1)(\bar{n}(\tilde{\nu}_2,T))$	$(\bar{n}(\tilde{\nu}_1,T))(\bar{n}(\tilde{\nu}_2,T)+1)$

4.3 Selection Rules for the First Order Raman Effect

It has been seen in Section 4.1 that the phonons created or destroyed in the first order Raman process have almost zero wavevector. These phonons are non-propagating and do not see the translational properties of the lattice, thus, only the point group of the unit cell rather than the space group of the crystal need be considered to derive the selection rules for first order Raman activity. It is found that for the zinc-blende structure at the zone centre, both the acoustic and optic modes have symmetry species Γ_{15} and are triply degenerate by group theory (Nilsen, 1969b).

In addition to crystal symmetry considerations Poulet (1955) has shown that in polar crystals there is a macroscopic electric field associated with the longitudinal optical (LO) mode giving it a higher energy than the transverse optical (TO) mode. Thus the degeneracy of the optical branch is partly re-

moved leaving a LO mode and a doubly-degenerate TO mode. The LO and TO frequencies near the B.Z. centre obey a relation established by Lyddane, Sachs and Teller (1941)

$$\left[\nu(\mathrm{LO})/\nu(\mathrm{TO})\right]^2 = \epsilon_s/\epsilon_\infty \qquad (3.7)$$

where ϵ_s is the static dielectric permittivity and ϵ_∞ is the dielectric permittivity at frequencies sufficiently high that the ions cannot respond to the electric field of the radiation.

The Raman tensors for the Γ_{15} vibrational modes (see Table III) are transformed so that the polarizability tensor is expressed in terms of the coordinates q_l, which is parallel to the wavevector of the phonon, and q_{t_1} and q_{t_2} which are mutually perpendicular to the phonon wavevector. In this way the tensors refer to purely longitudinal and transverse phonons. The tensors are then transformed to the laboratory reference frame. In order to obtain quantities proportional to the Raman intensity the elements of the resulting tensors are squared and the results for the TO modes are added together. The scattering intensity matrices for the two crystal orientations which result are given by (Poulet, 1955)

$$\Theta_{LO}(100) = E_i^2\begin{pmatrix} 0 & \frac{1}{2} & 0 \\ \frac{1}{2} & 0 & \frac{1}{2} \\ 0 & \frac{1}{2} & 0 \end{pmatrix} \quad ; \quad \Theta_{TO}(100) = E_i^2\begin{pmatrix} 0 & \frac{1}{2} & 1 \\ \frac{1}{2} & 0 & \frac{1}{2} \\ 1 & \frac{1}{2} & 0 \end{pmatrix}$$

where E_i refers to the electric field intensity of the incident light, and

$$\Theta_{LO}(110) = E_i^2\begin{pmatrix} 0 & \frac{1}{2} & 0 \\ \frac{1}{2} & 0 & \frac{1}{2} \\ 0 & \frac{1}{2} & 0 \end{pmatrix} \quad ; \quad \Theta_{TO}(110) = E_i^2\begin{pmatrix} 1 & \frac{1}{2} & 0 \\ \frac{1}{2} & 0 & \frac{1}{2} \\ 0 & \frac{1}{2} & 1 \end{pmatrix}$$

The single crystals investigated here were prepared having two particular orientations. These two crystal orientations are designated (100) and (110). The (100) crystal is cut and polished with all 100 faces; whereas, the (110) crystal is cut with four 110 faces and two 100 faces. In both cases the crystals are in the shape of rectangular parallopipeds.

Figure 6b shows the crystal orientation relative to the scattering geometry used in the Raman scattering experiments. In all cases the incident light was directed along the laboratory Z axis and the scattered light detected along the laboratory X axis.

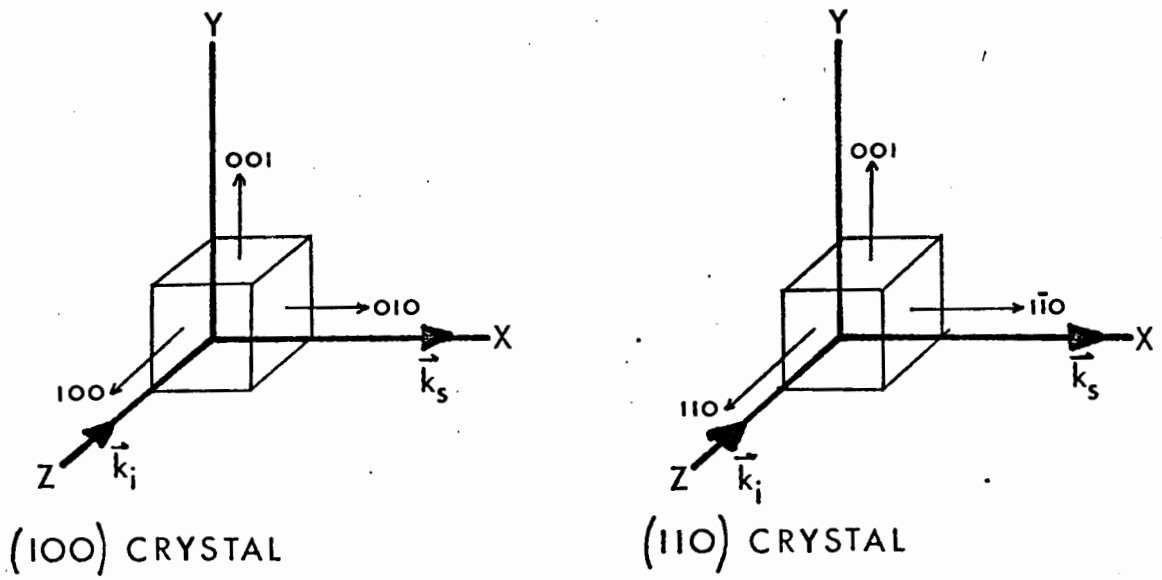

Figure 6b - The scattering geometry and single crystal orientations used in the Raman scattering experiments.

In order to designate the polarization and direction of the incident and scattered lights the following notation will be used: the first and last letters in Z(YY)X indicate the direction of propagation for the incident and scattered light, respectively; the first and last letters inside the parenthesis indicate the polarization directions of the incident and scattered light, respectively. For example, for a (100) crystal and polarizations Z(XZ)X one would expect from the intensity matrices above a very weak longitudinal optical peak and a strong transverse optical phonon peak in the Raman spectrum. For the same experimental set up but using a (110) crystal one would expect both very weak LO(Γ) and TO(Γ) lines where the symbol in the bracket refers to that point of the B.Z. with which the phonon is associated.

4.4 Selection Rules for the Second Order Raman Effect

The second order Raman effect involves two phonons; because of this the conservation of momentum does not require that the scattering process take place near the B.Z. centre. Indeed, second order Raman scattering can originate from every point in the B.Z. However, the density of two phonon states tends to become greater for larger phonon wavevectors and thus most second order Raman scattering take place near the B.Z. boundary. Even though the scattering events may be assumed to

occur near the B.Z. boundary an interpretation of the Raman spectrum as such would be impossible if it were not for the existence of critical points in the B.Z. (Van Hove, 1953 and Phillips, 1956).

Critical points for the zincblende reciprocal lattice occur at X(1, 0, 0), L($\frac{1}{2}$, $\frac{1}{2}$, $\frac{1}{2}$) and W(1, $\frac{1}{2}$, 0) on the B.Z. boundary (Parmenter, 1955). These points locate regions of high phonon density of states.

Scattering from phonons at these critical points is believed to be responsible for the sharp features in the second order Raman spectra and many researchers have interpreted their Raman spectra accordingly. It should be noted that Γ(0, 0, 0) is also a critical point due to the flattening of the dispersion curves at the B.Z. centre but Γ does not have the high density of states associated with the zone boundary critical points.

The second order Raman selection rules have been derived for the zincblende crystal structure by Birman (1963). The procedure used to obtain these selection rules is briefly outlined in the Appendix. These selection rules are summarized in Table V. In Table V, Column 2 gives the irreducible representations of the Raman active modes at each critical point. Column 3 gives the polarization of these modes where distinguishable by group theory. Column 4 lists the possible two phonon processes possible at each critical point. Columns 5 and 6 express the infra-red and Raman activity, respectively, in terms of the irreducible representations of the

TABLE V

The selection rules for the zincblende structure.

Critical Point	Irreducible Representation	Polarization	Sums and Overtones	I.R. Activity	Raman Activity
L	L_3	TA(L)	LA⊗LO	Γ_{15}	$\Gamma_1+\Gamma_{15}$
	L_1	LA(L)	LA⊗TO=TA⊗LO	Γ_{15}	$\Gamma_{12}+\Gamma_{15}$
	L_3	TO(L)	TA⊗LA=TO⊗LO		
	L_1	LO(L)	TA⊗TO	$2\Gamma_{15}$	$\Gamma_1+\Gamma_{12}+\Gamma_{15}$
			2LA=2LO	Γ_{15}	$\Gamma_1+\Gamma_{15}$
			2TA=2TO	$2\Gamma_{15}$	$\Gamma_1+\Gamma_{12}+2\Gamma_{15}$
W	W_1		$W_1\otimes W_2=W_3\otimes W_4$	Γ_{15}	$\Gamma_{12}+\Gamma_{15}$
	$2W_2$		$W_1\otimes W_3=W_1\otimes W_4$	Γ_{15}	Γ_{15}
	$2W_3$		$W_2\otimes W_3=W_2\otimes W_4$		
	W_4		$W_2\otimes W_2=W_3\otimes W_3$	Forbidden	$\Gamma_1+\Gamma_{12}$
			$2W_1=2W_2$	Forbidden	$\Gamma_1+\Gamma_{12}$
			$2W_3=2W_4$		
X	X_5	TA(X)	LA⊗LO	Γ_{15}	Γ_{15}
	X_1	LA(X)	TA⊗LA=LA⊗TO	Γ_{15}	Γ_{15}
	X_5	TO(X)	TA⊗LO=TO⊗LO		
	X_3	LO(X)	TA⊗TO	Γ_{15}	$\Gamma_1+2\Gamma_{12}+\Gamma_{15}$
			2LA=2LO	Forbidden	$\Gamma_1+\Gamma_{12}$
			2TA=2TO	Γ_{15}	$\Gamma_1+2\Gamma_{12}+\Gamma_{15}$
Γ	Γ_{15}	Degenerate			
	Γ_{15}	LO(Γ)	LO($\vec{q}\sim 0$)	Forbidden	Γ_{15}
		TO(Γ)	TO($\vec{q}\sim 0$)	Γ_{15}	

point group T_d (Birman, 1963 and Krauzman, 1969). It can be seen from the table that all two phonon processes are Raman active. Also it should be noted that the 2LA(L) and 2LO(L) two phonon processes are forbidden in infra-red absorption.

4.5 Polarization Properties of the Second Order Raman Spectrum

In order to distinguish which symmetry species are present in a Raman spectrum it is necessary to know the scattering intensity matrices for the irreducible representations of the Raman active vibrations. The Raman tensors corresponding to the three irreducible representations Γ_1, Γ_{12} and Γ_{15} of the polarizability tensor are given in Table III relative to the cubic cell axis $\hat{i}$, $\hat{j}$ and $\hat{k}$. By transforming these matrices from the crystal orientation under examination to the laboratory coordinates X, Y and Z and squaring the element of the transformed tensors one obtains the Raman scattering intensity matrices for the irreducible representations (Nilsen, 1969b):

$$\Gamma_1(100) = a^2 \begin{pmatrix} 1 & 0 & 0 \\ 0 & 1 & 0 \\ 0 & 0 & 1 \end{pmatrix} \qquad \Gamma_1(110) = a^2 \begin{pmatrix} 1 & 0 & 0 \\ 0 & 1 & 0 \\ 0 & 0 & 1 \end{pmatrix}$$

$$\Gamma_{12}(100) = b^2 \begin{pmatrix} 4 & 0 & 0 \\ 0 & 4 & 0 \\ 0 & 0 & 4 \end{pmatrix} \qquad \Gamma_{12}(110) = b^2 \begin{pmatrix} 1 & 0 & 3 \\ 0 & 4 & 0 \\ 3 & 0 & 1 \end{pmatrix}$$

$$\Gamma_{15}(100) = d^2 \begin{pmatrix} 0 & 1 & 1 \\ 1 & 0 & 1 \\ 1 & 1 & 0 \end{pmatrix} \qquad \Gamma_{15}(110) = a^2 \begin{pmatrix} 1 & 1 & 0 \\ 1 & 0 & 1 \\ 0 & 1 & 1 \end{pmatrix}$$

The Γ_{15} matrices for each crystal orientation may be obtained from the sum of Raman scattering intensities for the LO and TO modes given in section 3.4.

The intensity matrices predict which irreducible representations are present in a Raman spectrum. For example consider a Z(XZ)X spectrum for a (110) crystal; only the Γ_{12} vibrational species are present in the spectra. Similarly a Z(XY)X spectrum for a (110) crystal contains only Γ_{15} species in second order and the LO and TO modes in first order (referring to section 2.4). The features in the Raman spectra which contain Γ_1 species can be obtained indirectly from spectra containing both Γ_1 and Γ_{12} species and comparison with a spectrum containing only the Γ_{12} species. A knowledge of the polarizability representations present in each feature of the Raman spectra should give some indication as to which critical point contributes to each feature. This method of analysis should, in principle, be of great assistance in making assignments to the various features observed in the second order Raman spectrum.

CHAPTER 5

EXPERIMENTAL

5.1 Apparatus

Raman scattering experiments have been carried out by several experimenters for many years now. Industry has responded to this and the activity of related fields of physics to produce equipment particularly suited to the needs of Raman spectroscopists (monochromators, lasers and photomultiplier tubes).

Figure 7 shows a schematic diagram of the experimental apparatus used in this study. Experiments were carried out over a four year period on different compounds and some changes in equipment occurred. These variations are summarized in Table VI.

TABLE VI

Summary of changes in experimental apparatus.

Compound	Laser λ(Å)	Electronics	PM Tube	Temperature Varied
ZnTe	6328	PAR	EMI 9558	Yes
ZnSe(1)	4880 5145	PAR	ITT FW 130	Yes
ZnSe(2)	4880 5145	Photon Counting	Cooled FW 130	No
GaP	6328	Photon Counting	Cooled FW 130	No

(1) Polycrystal. (2) Oriented single crystals.

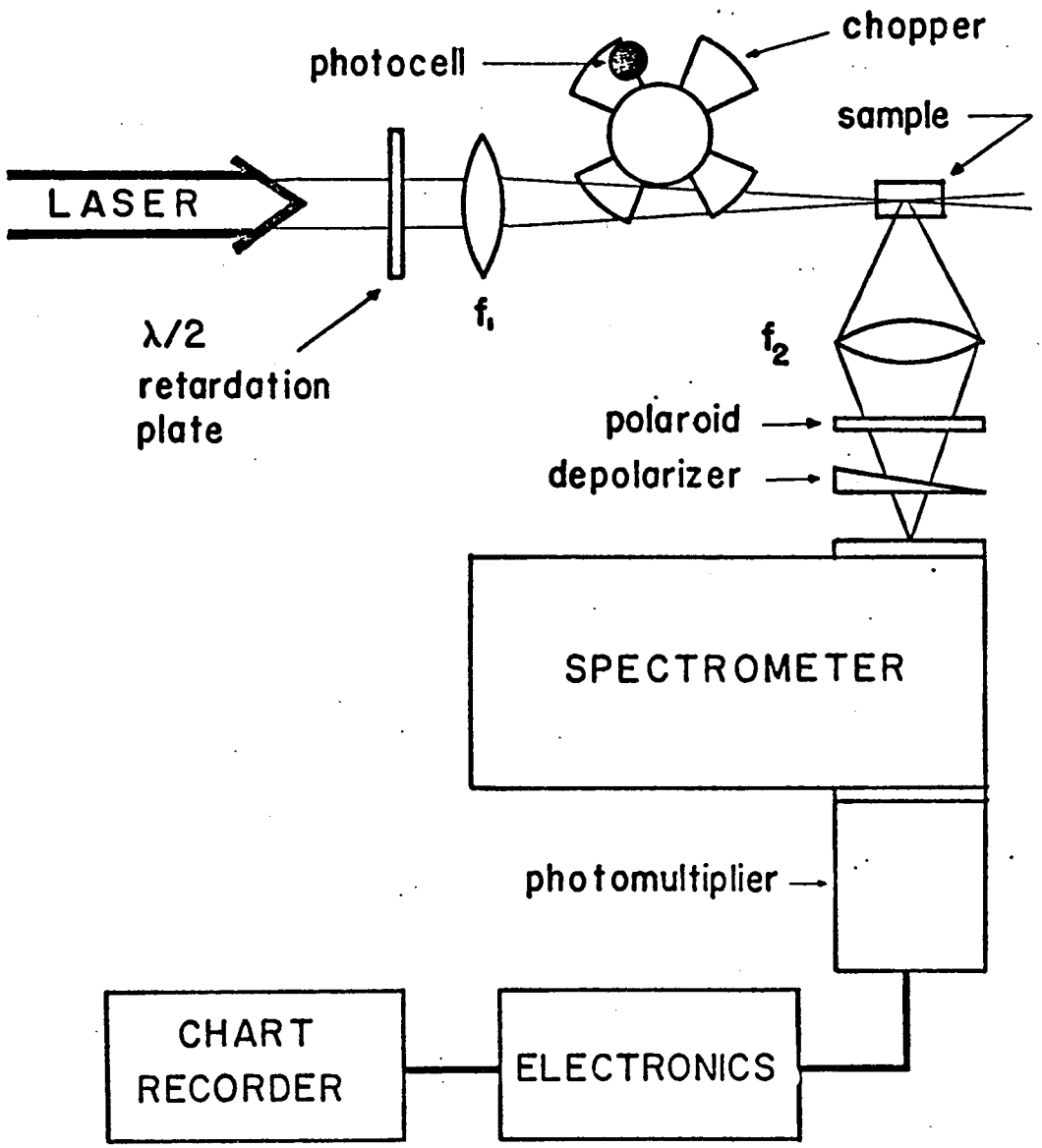

Figure 7. A schematic diagram of experimental set up.

In general, however, the Raman spectra were excited with either an argon ion laser operating at 4880Å or 5145Å at powers between 20 and 200 milliwatts or a He-Ne laser operating at 6328Å with an output power of about 50 milliwatts. A 90 degree scattering geometry was employed; that is the scattered light was collected in a direction perpendicular to the incident beam. The sample was mounted on a goniometer and could be carefully aligned in all orientations.

The spectra were analysed using a Spex double monochromator (model 1400). The laser output was highly polarized and its orientation was varied using a half-wave retardation plate. A polaroid sheet was used to select the desired polarization component of the scattered light. A quartz wedge was used to depolarize the light entering the monochromator ensuring a monochromator response independent of the polarization of the scattered light.

Two different detection systems were used: (a) the incident light was chopped at 40 Hz and the Raman signal analysed with a lock-in amplifier (Princeton Applied Research, model HR 8) or (b) the photomultiplier was cooled to dry ice - alcohol temperature and the scattered photons were counted using a preamplifier, pulse height analyser and ratemeter (Ortec). Two different photomultiplier tubes were used, a EMI 9558 and a ITT FW-130, both of S-20 response. The effective cathode size of the ITT photomultiplier used was 0.1 inches in diameter. This tube when cooled to dry ice - alcohol temperature had a dark count of about 1 per second.

The incident laser beam was focused onto the sample using a 180 mm lens and the scattered light was collected by a f/2, 55 mm focal length lens. This lens was matched to the f number of the entrance slit of the spectrometer.

The first order spectra were measured with a slit width giving a resolution of about 1 cm^{-1} and the second order spectra with a slit width giving a resolution of about 4 cm^{-1}. The spectral lines from a neon Geissler tube were superimposed on the spectra for purposes of calibration.

The Raman spectra of ZnTe and ZnSe were measured at temperatures between 4°K and 300°K. A helium-cooled variable temperature dewar manufactured by Andonian Associates Inc. served as the cryostat in these experiments.

5.2 Acquisition and Preparation of Samples

(a) ZnTe. Past experiments on ZnTe have been made difficult by strong luminescence. For this reason several ZnTe crystals were studied in this work. These came from three sources:

(i) One which came from Harshaw Chemical Company and showed no luminescence.

(ii) A crystal received from P.C. Eastman and L. Bradfield of the University of Waterloo. This crystal was grown in a carbon crucible from the melt and showed no luminescence.

(iii) Crystals grown by the author from the vapour using the technique of Piper and Polich (1961). Briefly a

stoichemetric mixture of Zn and Te was heated in an rf furnace with a peak temperature of 1150°C to 1175°C. Some of these crystals showed luminescence and some did not.

It should be mentioned that luminescence in ZnTe occurred in spite of the fact that the laser energy (1.955 eV) is much less than the bandgap (~ 2.25 eV at room temperature).

The luminescence consisted of a broad band centered at about 1.88 eV. Previous workers (Hopfield, Thomas and Lynch, 1960) have identified such a band and have attributed it to oxygen impurities substituted isoelectronically in the crystal. Raman spectra were obtained from all of these crystals.

Two oriented single crystals of ZnTe were cut and polished with faces (100), (010) and (001) for the crystal designated (100) and with faces (110), ($\bar{1}$10) and (001) for the crystal designated (110).

The orientation, or cut, of the crystals studied here was carried out to within one degree accuracy. The crystals were polished flat to an optical finish using Logitech polishing equipment. Because of the softness of the materials, tin lapping plates were used.

(b) ZnSe. Two sets of experiments were carried out on ZnSe. The first was performed on a large polycrystalline sample of ZnSe obtained from Harshaw Chemical Company. It measured 4 mm

x 8 mm x 8 mm in size. The second was performed on two single crystals obtained from the original polycrystalline ZnSe. The crystals for the second experiment were cut and polished with sides (100), (010), (00$\bar{1}$) for the crystal designated (100) and with sides (110), ($\bar{1}$10), (001) for the crystal designated (110). These two crystals measured about 2 mm x 2 mm x 4 mm in size.

Some luminescence was observed in the ZnSe material. At room temperature the luminescence occurred as a broad band around 6400Å; however, there was no visible luminescence in the spectral region around 4880Å and 5145Å where the Raman scattering experiments were carried out. When the sample temperature was lowered to temperatures below 100°K the ZnSe crystals luminesced quite strongly and the luminescence tended to completely mask the second order spectrum. Kr and He-Ne laser lines were used in an effort to avoid the luminescence problem but these attempts were not very successful. Despite the luminescence the major features of the Raman spectrum were studied with regard to their relative intensity to determine whether difference frequency modes were present.

(c) GaP. The GaP material studied here was obtained from two sources:

(i) single crystal platelets from Dr. Konrad Colbow of this department originally obtained from Semi-Elements Inc. and

(ii) single crystal platelets from Dr. Peter Barnes at

Bell Telephone Laboratories, Murray Hill, New Jersey.

Although there was no difference in the two materials in their Raman spectra, the results reported here were taken with a single crystal from source (ii).

The single crystal material studied showed no luminescence in the region of the spectrum observed. The crystal size available at this time did not permit the cutting of oriented single crystals for a study of the polarization properties of the Raman spectrum of GaP.

CHAPTER 6

RESULTS

6.1 Introduction

In this chapter the Raman spectra of ZnTe, ZnSe and GaP are presented. The resulting spectra are analysed using the S.N.I. model. In section 6.4 the polarization properties of the Raman spectrum of ZnSe are also presented. These results are compared with the assignments made to the Raman features based on the S.N.I. model. In section 6.5 the Raman spectrum of GaP is analysed with the purpose of comparing the results with the directly measured values of the lattice mode frequencies obtained from neutron scattering experiments.

6.2 Zinc Telluride

The Raman spectrum of ZnTe for a nonluminescent crystal at room temperature is shown in Figure 8. The first order modes have been labelled by the letters A and B and their frequencies have been measured to be

A: $\tilde{\nu} = 208.3 \pm 0.5 \text{ cm}^{-1}$

B: $\tilde{\nu} = 177.5 \pm 0.5 \text{ cm}^{-1}$

The phonon frequencies were independent of the crystal used to within experimental error and thus are not strongly influenced by impurities. The impurity concentrations in the ZnTe crystals used varied from 5×10^{16} to 5×10^{17} cm^{-3}. At these concentrations plasma effects (Mooradian and Wright, 1966) are negligible in ZnTe. The first order Raman spectrum of ZnTe was also observed

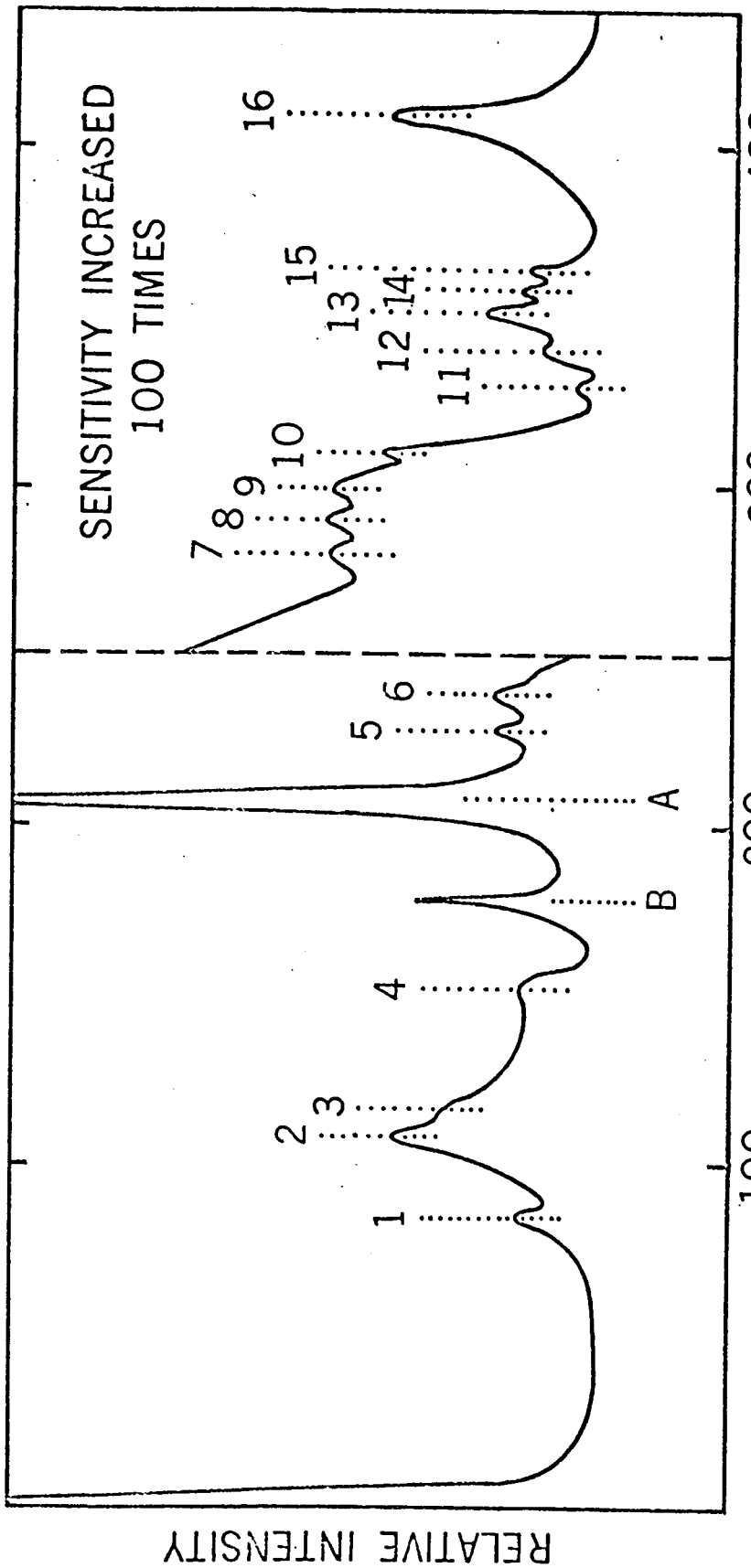

Figure 8 - The Raman spectrum of ZnTe at room temperature.

as a function of crystal orientation (using (100) and (110) single crystals) and incident and scattered light polarizations.

The results for the first order modes were in good agreement with the predictions of Poulet (1955) and the selection rules derived from Loudon's (1964) polarizability tensors.

The values obtained for the zone center frequencies can be compared to the dielectric constant by using the Lyddane-Sachs-Teller (LST) relation of equation (4.7). Agreement was obtained between the frequencies and the published dielectric constant to about 3%. In Table VII are found the published dielectric constants and the measured room temperature values of the first order Raman frequencies and the percentage agreement between the two for ZnTe, ZnSe and GaP.

TABLE VII

A comparison of the measured room temperature first order Raman frequencies to the measured dielectric constants using the LST relation.

Material	$\tilde{\nu}_{LO}(cm^{-1})$	$\tilde{\nu}_{TO}(cm^{-1})$	ϵ_o	ϵ_∞	Agreement
ZnTe	208.3±.5	177.5±.5	10.4[a]	7.3[b]	3%
ZnSe	250. ±1	203. ±1	9.10[c]	5.90[d]	1%
GaP	402.8±1	366.6 ±1	10.18[e]	8.46[e]	1%

(a) Nahory and Fan (1967); (b) Aten et al. (1962);
(c) Berlincourt et al. (1963); (d) Marpole (1964);
(e) Barker (1968).

The numbers in Figure 8 designate the observed features in the second order spectrum and Table VIII contains a list of the frequencies corresponding to these features. Column four of Table VIII gives the mode assignments made to these features. Column three lists for comparison purposes the frequencies of the second-order features measured by Narita et al. (1967).

The assignments have been made on the following basis. It will be noticed that a Raman peak has been observed at 364cm^{-1} which is missing from Narita's infrared spectrum. This peak has been assigned to 2LO(X) since its particular overtone is forbidden in infrared absorption but allowed in Raman scattering (see Table V).

The features below 160^{-1} could be due to combinations of transverse acoustic phonons (sums and overtones) or to differences such as LA(X)-TA(X). The differences are ruled out for two reasons. Firstly, the intensity of features due to differences decreases much more rapidly with temperature than the intensity of sums and overtones (see Table IV). Secondly, differences which combined a longitudinal mode and a transverse mode should be depolarized (Birman, 1963). The intensity of all the features below 100 cm^{-1} were observed to decrease at the same rate with decreasing temperature, and in addition were

TABLE VIII

The frequencies and assignments of the observed Raman features of ZnTe.

Feature Number from Figure 8	Frequency Shift (cm^{-1}) Here	Frequency Shift (cm^{-1}) I.R.(a)	Assignment	Frequency Shift Calculated for Table XIX	Error
1	90		2TA(L)	94	+4
2	108		2TA(X)	104	-4
3	116		$2W_1$	110	-6
4	156		W_1+W_2	159	+3
5	228		TO(X)+TA(X)	226	-2
6	240		LO(X)+TA(X)	235	-5
		253	$W_2+(W_3$ or $W_4)$	250, 1	-2
7	282	282	2LA(X)	282	0
8	290	289	$2W_3$, W_3+W_4, $2W_4$	292, 3, 4	+2,+3,+4
9	300	302	2LA(L)	306	+6
10	310	313	TO(X)+LA(X)	315	+5
11	329	332	TO(L)+LA(L)	327	-2
12	340	337	2LO(L),LO(L)+TO(L)	338, 342	-2,+2
13	349	351	2TO(L), 2TO(X)	346, 8	-3,-1
14	358	359	2TO(Γ),LO(X)+TO(X)	356, 7	-2,-1
15	364		2LO(X)	366	+2
16	412	414	2LO(Γ)	416	+4

(a) Narita et al. (1967).

strongly polarized. On the basis of these observations the low-energy features were assigned to overtones and sums of transverse acoustic phonons. The S.N.I. model described in section 3.5, was employed in making the remainder of the assignments. The seven parameters α, χ, β, μ_1, μ_2, λ_1, λ_2 were determined in the following manner. α and χ were evaluated from the frequencies at Γ, μ_1 from the value of LO(X) and μ_2 using the elastic constant C_{11}. The elastic constants C_{12} and C_{44} were then used to estimate β and $\lambda_1 + \lambda_2$. The values of β, λ_1 and λ_2 were then varied to obtain a good fit of the calculated zone boundary frequencies to the experimental results. Agreement was obtained with the elastic constants to better than 5%.

The values of the parameters used in applying the S.N.I. model to ZnTe and to the other materials studied are found in Table IX. The elastic constants calculated using these parameters, the measured values of the elastic constants and other relevant data are also found in Table IX. The normal mode frequencies calculated from the S.N.I. model for ZnTe at the critical points are found in column 3 of Table X. Columns 4, 5, and 6 of Table X gives the average zone boundary frequencies estimated by Narita et al. (1967), Nahory and Fan (1967) and Nilsen (1969a), respectively. On comparison one can see that a major discrepancy between this work and theirs is that their values for the LA mode are 20 cm^{-1} or more lower; however, it was found that a value of less than 140 cm^{-1} is inconsistent with the S.N.I. model, leading to exhorbitant errors in the calculated elastic constants. Nilsen (1969a) has interpreted the

TABLE IX

S.N.I. model parameters for materials studied.

Material	ZnTe	ZnSe	ZnS[1]	GaP
α (dynes/cm.)	22,836.	25,459.	28,596.	45,344.
β (dynes/cm.)	22,600.	25,200.	33,000.	26,500.
μ_1 (dynes/cm.)	1,740.	4,750.	4,060.	3,200.
μ_2 (dynes/cm.)	3,000.	0.	1,120.	3,500.
λ_1 (dynes/cm.)	-7,700.	2,200.	2,000.	4,000.
λ_2 (dynes/cm.)	7,900.	-2,200.	-4,000.	-16,500.
χ	4,668	7,144.	10,178.	5,726.
m_1 (10^{-22} gms.)	1.085	1.085	0.5321	1.157
m_2 (10^{-22} gms.)	2.118	1.310	1.085	1.243
a (Å)	3.052	2.834	2.705	2.725
C_{11} Calculated	6.944	8.001	9.353	13.37
Measured	7.13[2]	8.10[2]		14.11
C_{12} Calculated	4.139	4.407	7.078	7.057
Measured	4.07[2]	4.88[2]		6.187
C_{44} Calculated	3.066	3.955	3.108	4.513
Measured	3.12[2]	4.41[2]		7.043

(1) Irwin, (1970).

(2) Berlincourt et al., (1963).

TABLE X

Critical point frequencies (in cm^{-1}) for ZnTe.

Critical Point	Mode	S.N.I. Model	Narita et al.	Nahory & Fan	Nilsen
Γ	LO	208	206	210	205
	TO	178	179	178	177
X	LO	183	157	177	204
	TO	174	175	177	204
	LA	141	126	129	54
	TA	52	73	56	54
L	LO	169			
	TO	173			
	LA	154			
	TA	47			
W	W_1	55			
	W_2	103			
	W_3	146			
	W_4	147			
	W_5	169			
	W_6	185			

2LO(Γ) mode as an overlap of the boundary optical overtones and feature 2 of the Raman spectrum (see Figure 8) as an overlap of the acoustic modes. These assignments disagree strongly from those presented here.

The frequencies in Table X have been used to calculate the proposed assignments and these figures are given in column 5 of Table VIII. The difference between the observed and calculated values is given in column 6 of Table VIII. It can be seen that the maximum difference is 6 cm^{-1} which implies a difference of about 3 cm^{-1} in the actual frequency. This corresponds to an uncertainty of less than 3% in the frequency concerned.

6.3 Zinc Selenide (unoriented polycrystal)

The Raman spectrum of an unoriented ZnSe sample at room temperature is shown in Figure 9. The two first order vibrational modes are again labelled A and B and these frequencies at room temperature have been measured to be

A: $\tilde{\nu}_{LO} = 250.0 \pm 1.0\ cm^{-1}$

B: $\tilde{\nu}_{TO} = 203.0 \pm 1.0\ cm^{-1}$

The values are in good agreement with those obtained by Krauzman (1969) and Nilsen (1969a) but disagree somewhat with those reported by Taylor (1967) and Riccius (1968) (see Table XIII).

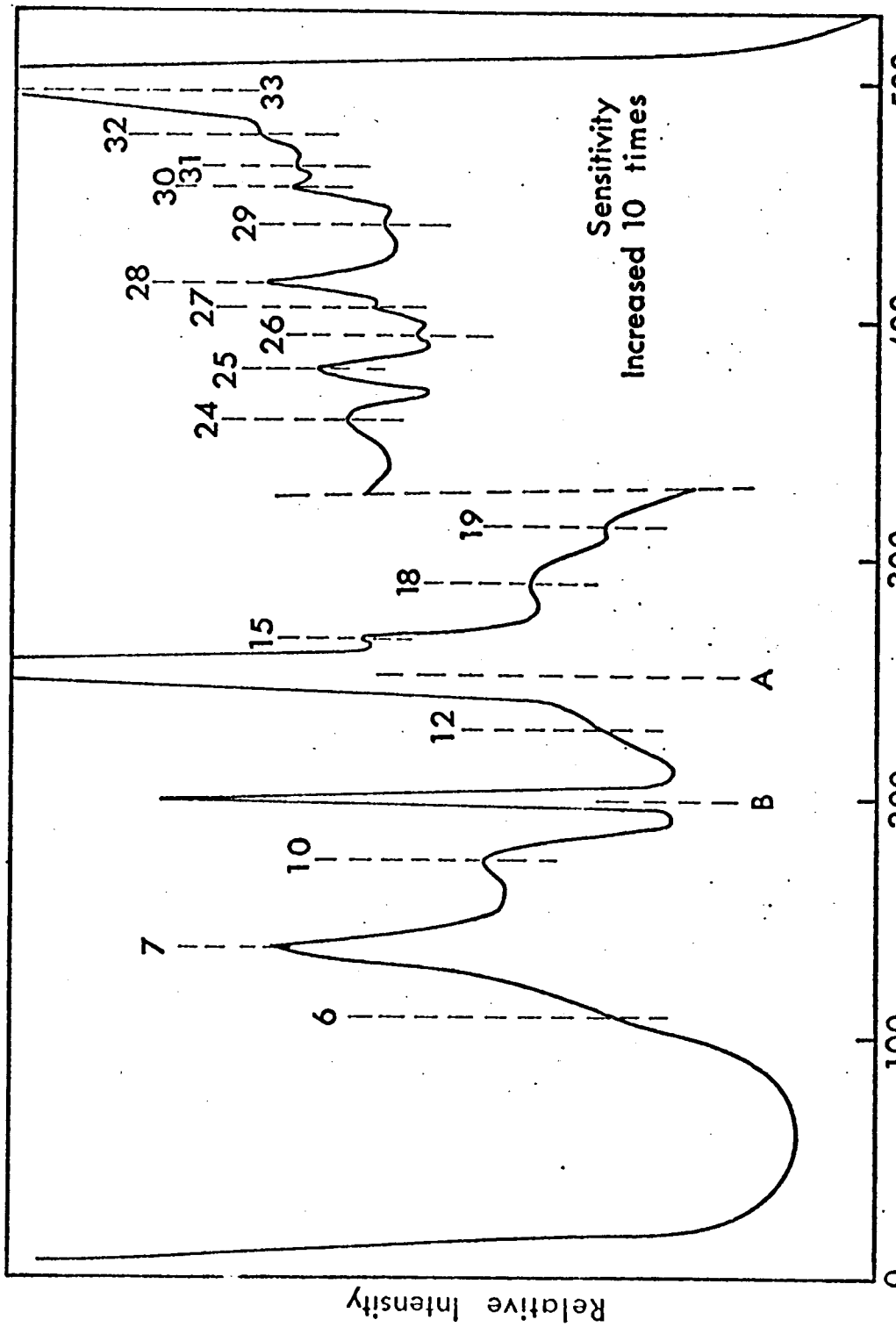

Figure 9 - The Raman spectrum of ZnSe at room temperature.

TABLE XI

A comparison of measured first order Raman frequencies of ZnSe.

	Here	Krauzman (1969)	Nilsen (1969a)	Taylor (1967)	Riccius (1968)
$\tilde{\nu}_{LO}(cm^{-1})$	250.0	251.	250.	254.	255.
$\tilde{\nu}_{TO}(cm^{-1})$	203.0	204.	205.	205.	209.

Applying the LST relation to the first order mode frequencies better than 1% agreement was obtained between the predicted and observed ratios (see Table VII).

The features of the Raman spectrum of the unoriented ZnSe polycrystal which have been attributed to second order processes are designated numerically in Figure 9. Their frequencies are listed in Table XII with the corresponding mode assignments.

Some assumptions have been made in the interpretation of the second order Raman spectrum. The degree of ionicity of the material studied can be calculated using the Szigeti relation (3.9). This equation can be solved for effective electronic charge e_s^* and gives $|e_s^*| = .8$ implying that the binding in ZnSe is quite ionic. On this basis it has been assumed that the LO and TO branches do not cross and therefore $\tilde{\nu}_{LO}$ is greater than $\tilde{\nu}_{TO}$ at the zone boundary. This point will be discussed in greater detail in Chapter 7.

TABLE XII

The frequencies and assignments of various Raman features of ZnSe.

Feature from Figure 10	Frequency Shift Here	Frequency Shift Mitra (1963)	Assignment	Frequency Shift from Table XVII	Difference
6	117		TO(X)-TA(X)	120	+3
7	139		2TA(L)	136	-3
10	189		2TA(X)	190	+1
12	228		LA(L)+TA(L)	228	0
		250	LO		
15	270		TO(L)+TA(L)	275	+5
18	296		LO(L)+TA(L)	302	+6
19	317		2LA(X),2LA(L)	320	+3
24	368	371	TO(L)+LA(L)	367	-1
25	381		LO(X)+LA(X)	383	+2
26	396		LO(L)+LA(L)	394	-2
27	407		2TO(Γ)	406	-1
28	414	420	2TO(L)	414	0
29	431		2TO(X)	430	-1
30	448		2LO(X)	448	0
31	455		TO(Γ)+LO(Γ)	453	-2
32	464		2LO(L)	468	+4
33	503	501	2LO(Γ)	500	-3

Certain features in the spectrum could be identified rather quickly. For example the peaks at 501 and 407 cm^{-1} were assumed to be resonances of $\tilde{\nu}_{LO}(\Gamma)$ and $\tilde{\nu}_{TO}(\Gamma)$ respectively. The features around 450 cm^{-1} were attributed to LO overtones from X and L and the features around 415 cm^{-1} to TO overtones from X and L. The strong peaks around 150 cm^{-1} were tentatively attributed to TA overtones. The other possibility is that they could be due to differences between the optic and acoustic modes. Theoretically, from Table II, it can be expected that for a change in temperature from 300°K to 75°K, if these features were sums or overtones their intensities would decrease by about a factor of 6, and if they were difference frequencies, about a factor of 11 while the first order modes would decrease only by a factor of 1.4. From observations of the spectrum at 75°K it was found that the relative intensity of the 139 cm^{-1} and 189 cm^{-1} features did not differ significantly from the other second order features of the spectrum. These two features were therefore tentatively assigned to TA overtones at X and L.

To make a more quantitative interpretation of the spectrum the S.N.I. model was applied to the data. The seven parameters were determined in the following way. α and χ were determined from the zone centre frequencies $\tilde{\nu}_{LO}$ and $\tilde{\nu}_{TO}$. μ_1 and μ_2 were determined from the frequencies $\tilde{\nu}_{LO}(X)$ and $\tilde{\nu}_{LA}(X)$. In this case they were not known but, based on the above discussion, an estimate of $\tilde{\nu}_{LO}(X)$ was made and μ_1 determined. The elastic constant C_{11} was then used to get an estimate of μ_2 and this should have given a reasonable value of $\tilde{\nu}_{LA}(X)$. Similarly β,

λ_1, and λ_2 were estimated from the elastic constants C_{12} and C_{44} and then used in the computation of $\tilde{\nu}_{TO}(X)$ and $\tilde{\nu}_{TA}(X)$. When it was felt that a reasonable set of parameters had been obtained the frequencies at L and W were calculated. These were then checked for a fit with the experimental values and if agreement was not obtained the parameters were varied and a new set of values was calculated. The only constraints placed upon the parameters was that they give reasonable agreement with the elastic constants. Thus one is essentially choosing a set of critical point frequencies which are consistent with both the experimental results and the S.N.I. model. The measured elastic constants used in this fit and the set of parameters arrived at for the case of ZnSe are found in Table IX. The resulting frequencies at the critical points Γ, X, L and W are tabulated in the third column of Table XIII. These frequencies have been used to determine the assignments given in column 3 of Table XII. These listed frequencies are accounted for entirely by phonons from X and L. However it should be noted that in several cases the same peaks could be accounted for by combinations of phonons from W. These have been left out of the table on the assumption that the scattered intensity from W will be somewhat weaker than that from L and X because of decreased symmetry and degeneracy (Johnson, 1965).

It should be mentioned that the differences in column 6 of Table XII are quite small indicating very good agreement between the assignments made on the basis of the experimental results and those predicted from the S.N.I. model. In fact

TABLE XIII

Critical point frequencies for ZnSe in cm^{-1}.

Critical Point	Mode	S.N.I. Model	Mitra (1963)	Nilsen (1969a)
Γ	LO	250		
	TO	203		
X	LO	224	208	252
	TO	215	212	252
	LA	159	162	76
	TA	95	87	76
L	LO	234		
	TO	207		
	LA	160		
	TA	68		
W	W_1	106		
	W_2	116		
	W_3	143		
	W_4	210		
	W_5	216		
	W_6	223		

this agreement must be considered to be fortuitous in that the measured values are only accurate to ± 4 cm^{-1} and one would not expect much better than 5% agreement of the theoretical model with the actual frequencies. Table XIII contains the average zone boundary frequencies obtained by Mitra (1963) and those found by Nilsen (1969). As is seen the agreement with the results is not particularly good in either case but the values of Mitra give the best comparison. Nilsen's results do not seem to be compatible with the results presented here or the theoretical model.

6.4 Zinc Selenide (oriented single crystals)

The Raman spectra of oriented single crystals of ZnSe are shown in Figures 10 to 17. Each figure includes the crystal orientation, either (100) or (110) as defined earlier, the polarization of the incident and scattered light intensities, and the symmetry species predicted from group theoretical considerations. More detail was observed in these spectra of ZnSe because (a) photon counting electronics were used giving a higher signal-to-noise ratio than obtained with a lock-in-amplifier and (b) the contributing modes in the spectra were separated out better by varying the polarization and orientation of the single crystal samples. The first order vibrational modes have again been designated as A and B in Figures 10 to 17, and the other features of the spectra have been numbered to be consistent both with the results of this section and with the spectrum reported in section 6.2. The observed features have been listed in Table XIV. The numbers which appear in these

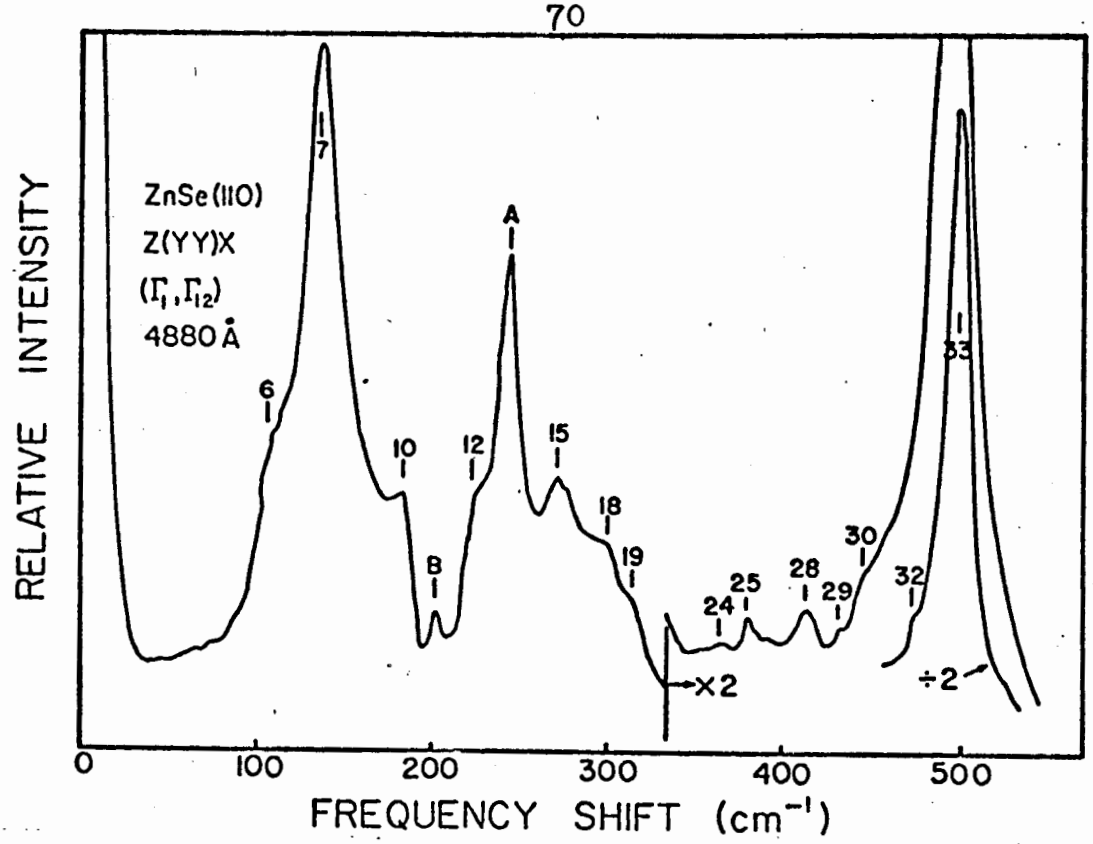

Figure 10 - The Raman spectrum of a ZnSe (110) crystal with Z(YY)X polarization.

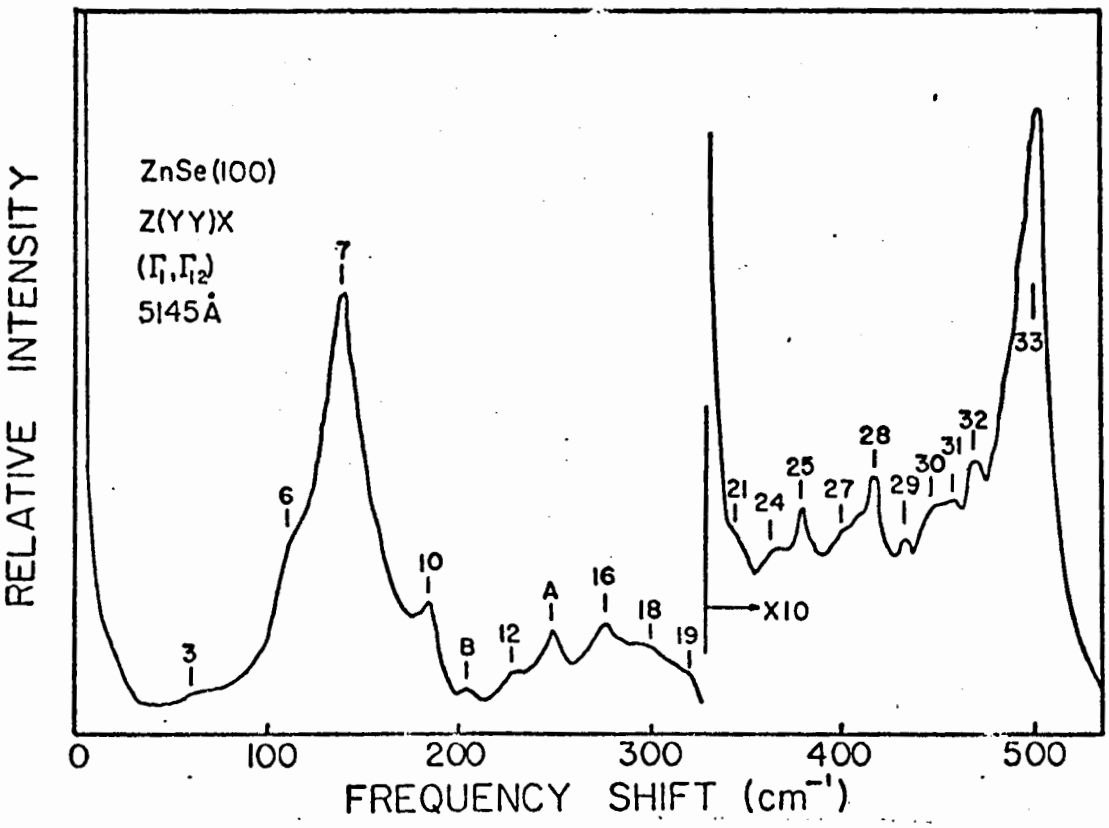

Figure 11 - The Raman spectrum of a ZnSe (100) crystal with Z(YY)X polarization.

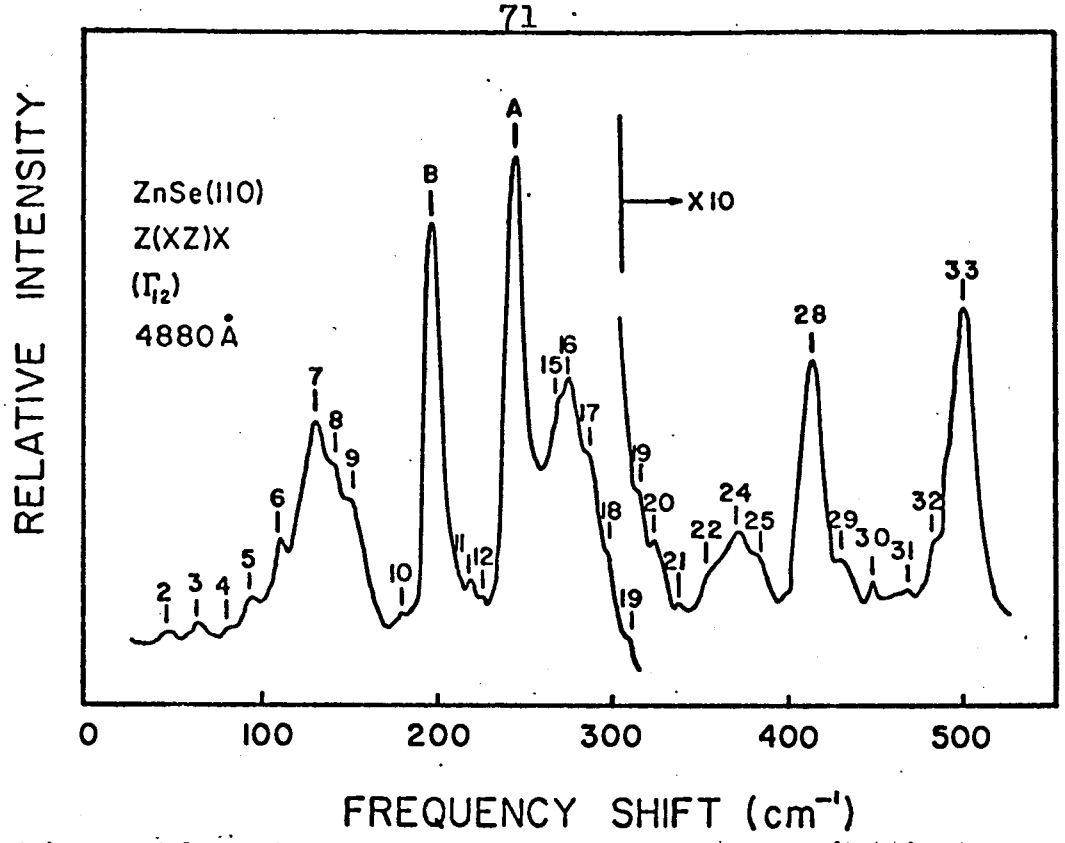

Figure 12 - The Raman spectrum of a ZnSe (110) crystal with Z(XZ)X polarization.

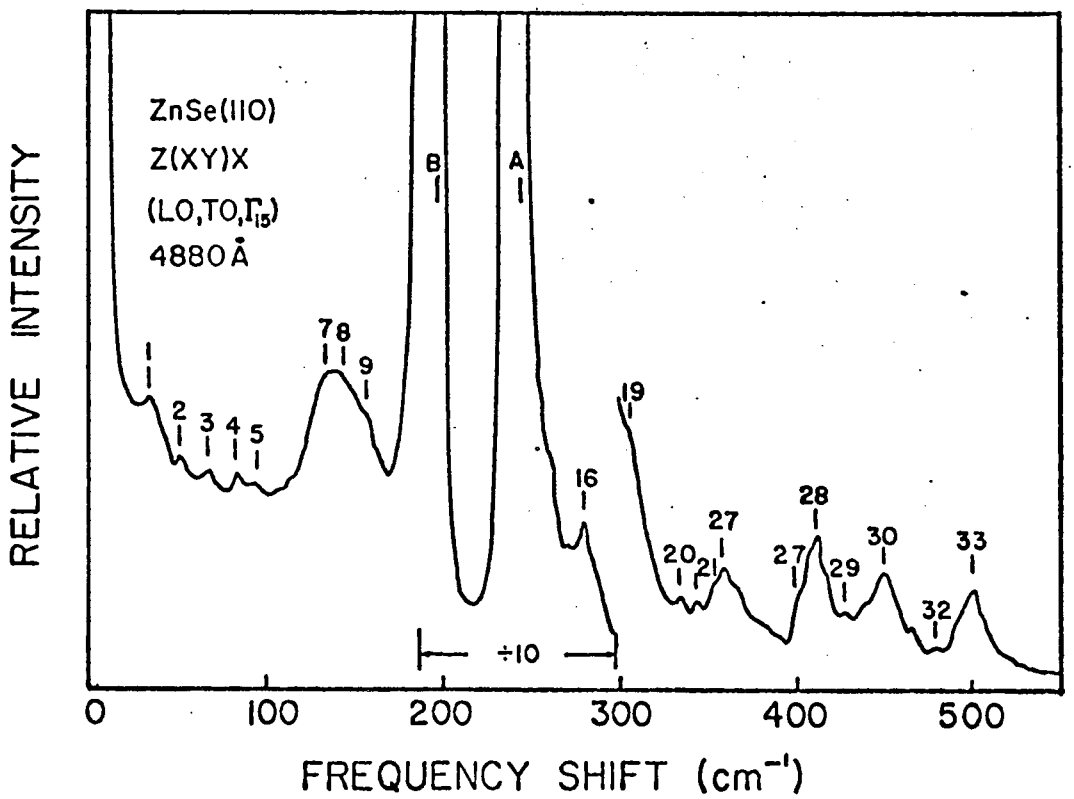

Figure 13 - The Raman spectrum of a ZnSe (110) crystal with Z(YZ)X polarization.

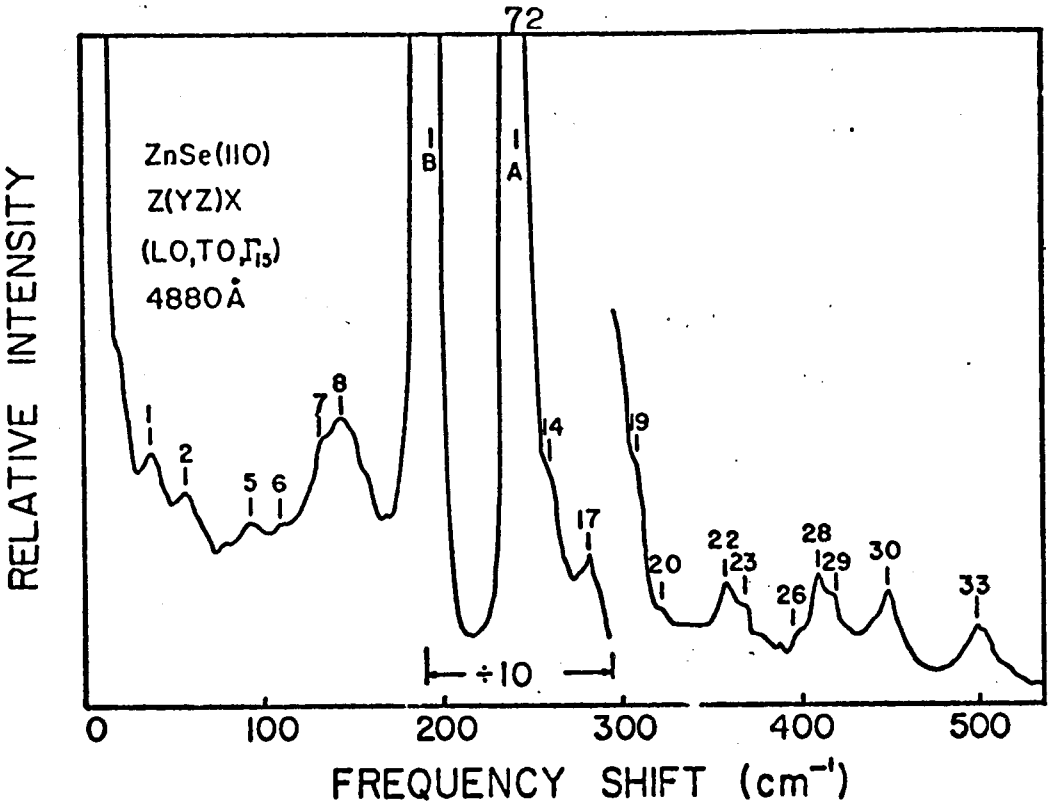

Figure 14 - The Raman spectrum of a ZnSe (110) crystal with Z(XY)X polarization.

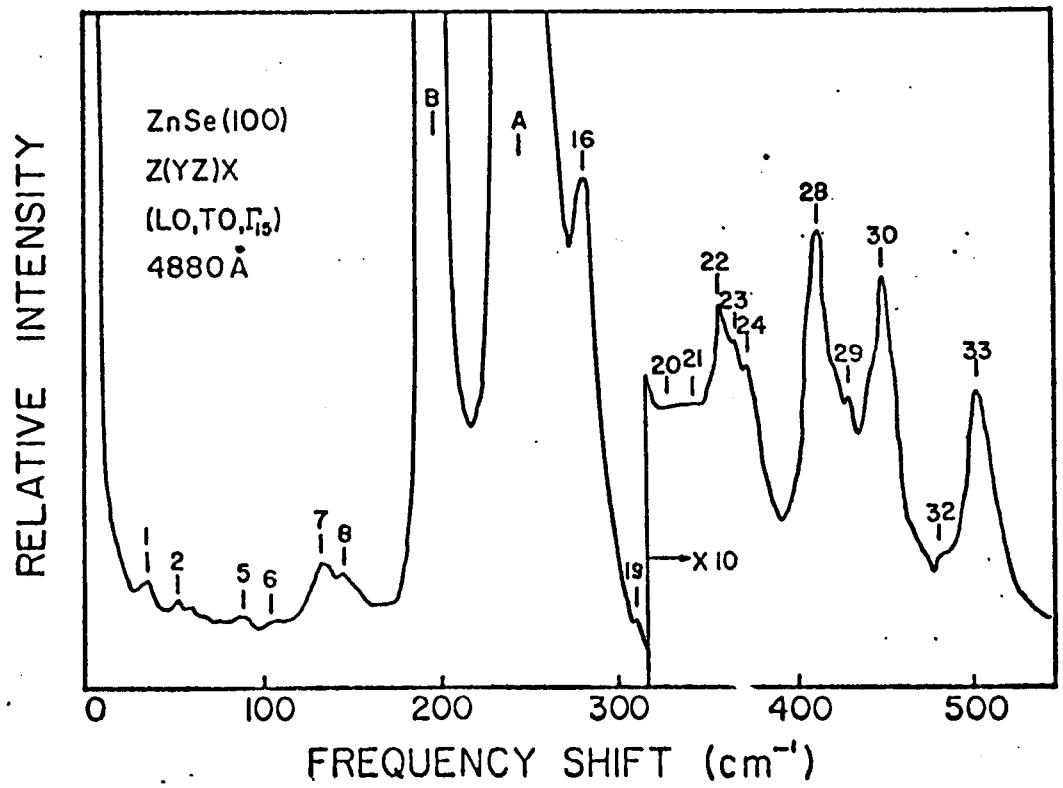

Figure 15 - The Raman spectrum of a ZnSe (100) crystal with Z(YZ)X polarization.

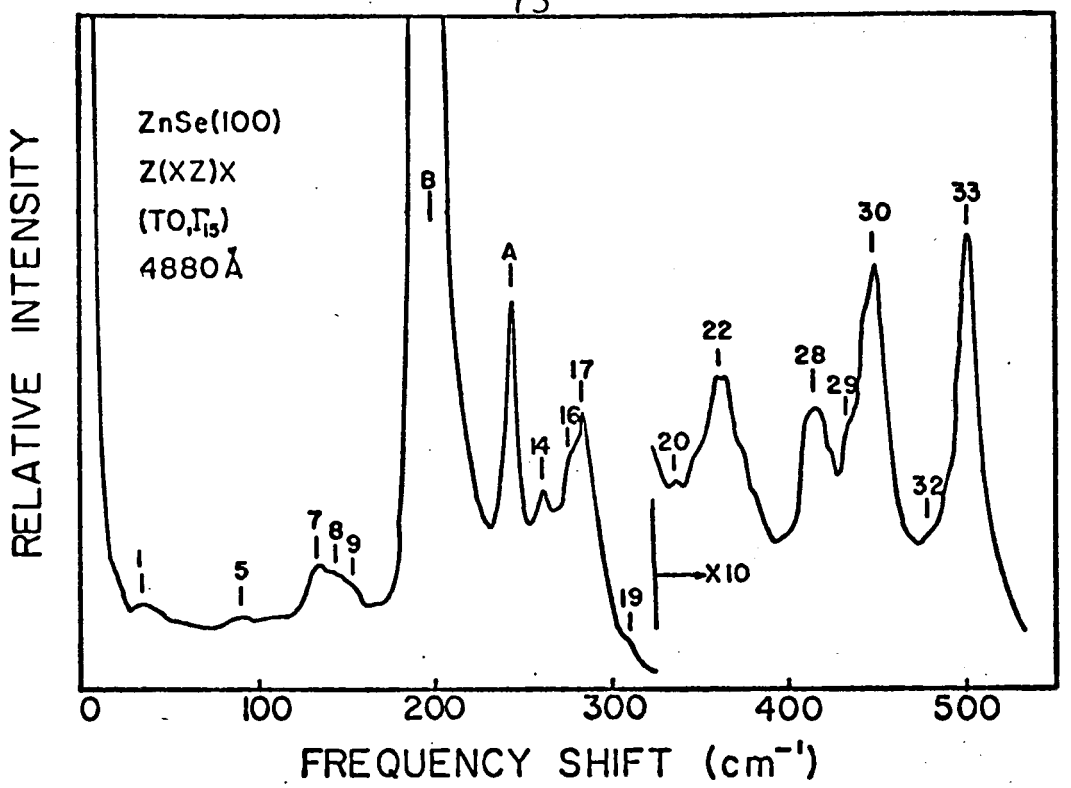

Figure 16 - The Raman spectrum of a ZnSe (100) crystal with Z(XZ)X polarization.

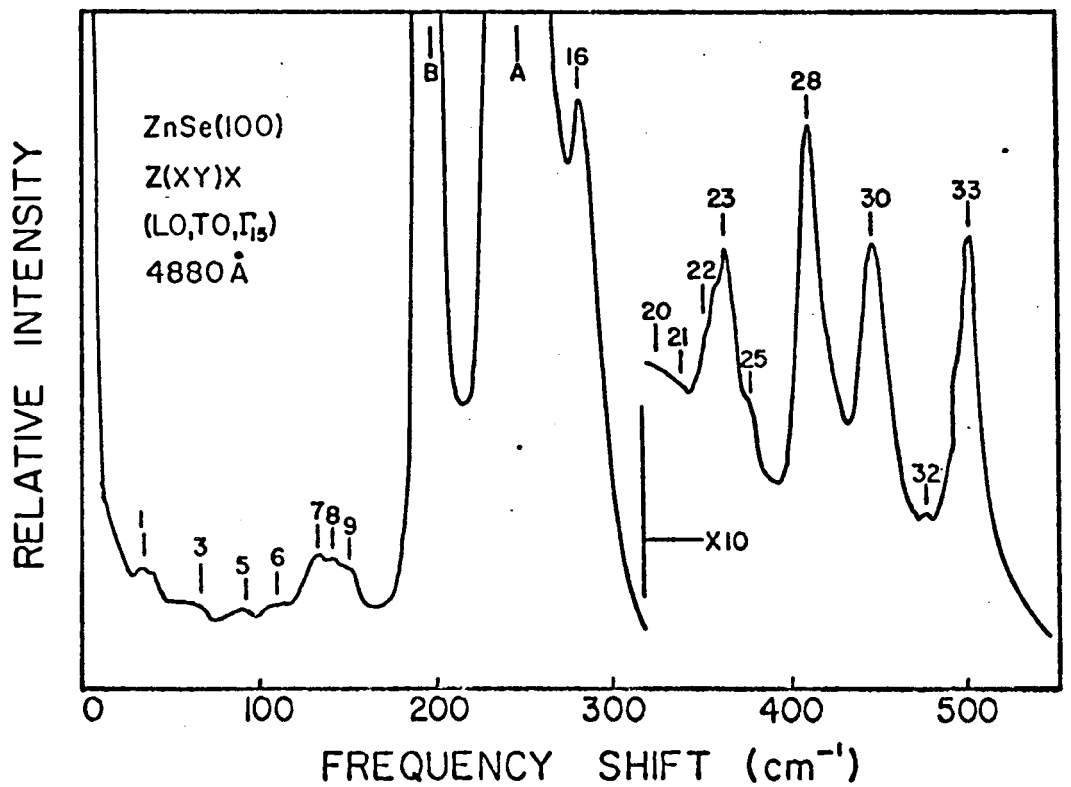

Figure 17 - The Raman spectrum of a ZnSe (100) crystal with Z(XY)X polarization.

TABLE XIV

The observed frequencies (cm^{-1}), assignments and predicted polarization characteristics of Raman features in ZnSe.

	Γ_1, Γ_{12}	Γ_{12}	Γ_{15}	S.N.I.	Assignment	Predicted Polarization Characteristics
1			38	37	W_3-W_1	Γ_{12}
2		50	50	47	TO-IA(L)	$\Gamma_{12}+\Gamma_{15}$
3	62	65	63	65	LO-IA(X), W_4-W_2	$\Gamma_1+\Gamma_{15}, \Gamma_{12}$
4		89	92	93	IA-TA(L)	$\Gamma_{12}+\Gamma_{15}$
5		106	108	107	W_6-W_2	
6	116	116	116	120	TO-TA(X)	$\Gamma_1+2\Gamma_{12}+\Gamma_{15}$
7	140	138	139	136/9	2TA(L), TO-TA(L)	$\Gamma_1+\Gamma_{12}, \Gamma_1+2\Gamma_{12}+\Gamma_{15}$
8		~154	154		?	
9		163	162	166	LO-TA(L)	$\Gamma_{12}+\Gamma_{15}$
10	186	186		190	2TA(X)	$\Gamma_1+2\Gamma_{12}+\Gamma_{15}$
B			TO		TO(Γ)	
11		220		222	W_1+W_2	Γ_{12}
12	228	230		228	IA+TA(L)	$\Gamma_{12}+\Gamma_{15}$
A			LO		LO(Γ)	
14			263	254	TA+IA(X)	Γ_{15}
15	269	272	} ?	275	TO+TA(L)	$\Gamma_1+\Gamma_{12}+2\Gamma_{15}$
16	279	277	280 }			
17		288	286	286	$2W_3$	$\Gamma_1+\Gamma_{12}$
18	298	294		302	LO+TA(L)	$\Gamma_{12}+\Gamma_{15}$
19	311	311	312	310	TO+TA(X)	$\Gamma_1+2\Gamma_{12}+\Gamma_{15}$
20		326	326	318/20	2IA(X), 2IA(L)	$\Gamma_1+\Gamma_{12}, \Gamma_1+\Gamma_{15}$
21	338	340	338(?)	339	W_2+W_6	Γ_{12}
22		356	356	354	W_3+W_4	Γ_{12}
23			363	367	TO+IA(L)	$\Gamma_{12}+\Gamma_{15}$
24	370	367	371	374	TO+IA(X)	Γ_{15}
25	381	381		383	LO+IA(X)	Γ_{15}
26			394(?)	394	LO+IA(L)	$\Gamma_1+\Gamma_{15}$
27	403		403(?)	406	2TO(Γ)	$\Gamma_1+\Gamma_{12}+\Gamma_{15}$
28	411	412	412	414	2TO(L)	$\Gamma_1+\Gamma_{12}$
29	430	430	430	430	2TO(X)	$\Gamma_1+2\Gamma_{12}+\Gamma_{15}$
30	446	446	448	448	2LO(X)	$\Gamma_1+\Gamma_{12}$
31	457	457		453	LO+TO(Γ)	$\Gamma_1+\Gamma_{12}+\Gamma_{15}$
32	468/72	466	472	468	2LO(L)	$\Gamma_1+\Gamma_{15}$
33	502	500	500	500	2LO(Γ)	$\Gamma_1+\Gamma_{12}+\Gamma_{15}$

figures do not necessarily correspond to distinct peaks in every spectrum; for example, numbers 22 to 25 designate detail in one feature in Figures 12 to 17, but numbers 24 and 25 appear as separate peaks in Figures 10 and 11.

The critical point frequencies obtained earlier for ZnSe (Table XIII) have been used to make the assignments which appear in column 5 of Table XIV. Column 7 lists the theoretical polarization characteristics of the assignments. It should be noted that there have been no changes in the assignments made to the Raman features reported in section 6.3.

The eight observed spectra have been divided into three groups: the group containing both symmetry species Γ_1 and Γ_{12} (Figures 10 and 11), the group containing the symmetry species Γ_{12} (Figure 12) and the group containing the symmetry species Γ_{15} (Figures 13 to 17). It can be seen that apart from the first order features, A and B, the spectra within a group are very similar and that there are distinct differences between the spectra of the three groups. Because of this the features are listed in Table XIV in three columns under the heading of each group of spectra. It must be noted that mere reference to Table XIV is not sufficient to draw any conclusion concerning the polarization characteristics of the various features; in addition it is necessary to study the eight spectra of Figures 10 to 17 and to note the relative intensities which do not appear in the table. Also the presence of a strong feature will tend to mask a weak feature located close to it.

With the greater sensitivity new features have been observed. All but two of these new features have been assigned, namely features 8 and 16. Features 15 and 16, although differentiated in this treatment, may very well be the same peak in that they are only 8 cm^{-1} apart and the accuracy with which the measurements have been made in about ± 4 cm^{-1}. Features 21 and 22 are weak and appear in the hollow between a shoulder and a larger peak. These features were assigned as sum frequencies at the critical point W.

The Z(YY)X spectra for crystals (100) and (110), Figures 10 and 11 are identical except for the LO(Γ) contribution. Here the (110) crystal spectrum has been shown using 4880Å excitation and the (100) crystal spectrum has been shown using 5145Å excitation. The LO(Γ) and 2LO(Γ) lines were stronger relative to the other features for the 4880A excitation. Although not shown here the 3LO(Γ) and 4LO(Γ) features have also been observed using 4880A excitation. The occurance of these strong peaks is thought to arise from a resonant Raman effect (Loudon, 1964 and Malm and Haering, 1971).

In comparing the observed and theoretically predicted polarization characteristics of the Raman features, it can be seen that there is good agreement in most cases, and apparent disagreement in a few other cases. Consider for example feature 7. This feature has all three polarization characteristics and is particularly strong in Γ_1. This feature has been assigned as 2TA(L) which has the polarization properties $\Gamma_1+\Gamma_{12}$. However

the presence of feature 7 in Γ_{15} spectra can be accounted for by a superposition of the TO(L)-TA(L) mode with its Γ_{15} content on the 2TA(L) peak.

There are other examples of apparent disagreement. In particular feature 25 does not appear distinctly in the Γ_{15} spectrum and yet the assignment has only a Γ_{15} prediction. The absence of a peak in a particular spectrum is not too significant since one has no way of predicting the intensity. More significant is the presence of a feature with unpredicted polarization properties. This occurs for example for features 28 and 30. Here however it is believed that since they appear weakly their existence in the Γ_{15} spectra could possibly be attributed to effects in the crystal.

In general, with the exception of a few weak features, the polarization properties of the Raman spectra agree well with the chosen assignments. These results tend to reinforce the work on the polycrystalline ZnSe and one must conclude that the polarization data provide a useful aid in obtaining data from second order Raman spectra. The disadvantages involved in the procedure will be discussed more fully in section 7.4.

6.5 Gallium Phosphide

The Raman spectra of an unoriented single crystal of GaP at room temperature is shown in Figure 18. The first order Raman modes have been labelled by the letters A and B and their frequencies were found to be

A: $\tilde{\nu}_{LO} = 402.8 \pm 1\ cm^{-1}$

B: $\tilde{\nu}_{TO} = 366.6 \pm 1\ cm^{-1}$

These measurements are in reasonable agreement with other Raman determinations of the fundamental mode frequencies and also with the frequencies determined by far infra-red techniques. These frequencies are listed in Table XV.

Applying the LST relation to the first order mode frequencies, one obtains, using Barker's (1968) values for ε_o and ε_∞, better than 1% agreement between the predicted and observed ratios (see Table VII).

TABLE XV

Experimental determinations of $\tilde{\nu}_{LO}(\Gamma)$ and $\tilde{\nu}_{TO}(\Gamma)$ for GaP in cm^{-1}.

Mode	Raman			Infra-red	
	Here	Russel (1965)	Fray et al. (1969)	Kleiman & Spitzer (1920)	Barker (1968)
$\tilde{\nu}_{LO}(\Gamma)$	402.8	402.	403.0	402.3	404.
$\tilde{\nu}_{TO}(\Gamma)$	366.6	366.	367.3	366.0	366.

The features of the Raman spectrum of GaP which have been attributed to second order processes are numbered numerically in Figure 18 and are listed in Table XVI with the mode assignments which have been made to them.

In interpreting the spectrum the ionicity of the material was considered first. The effective charge of the ions in GaP were calculated using the Szigeti relation and was found

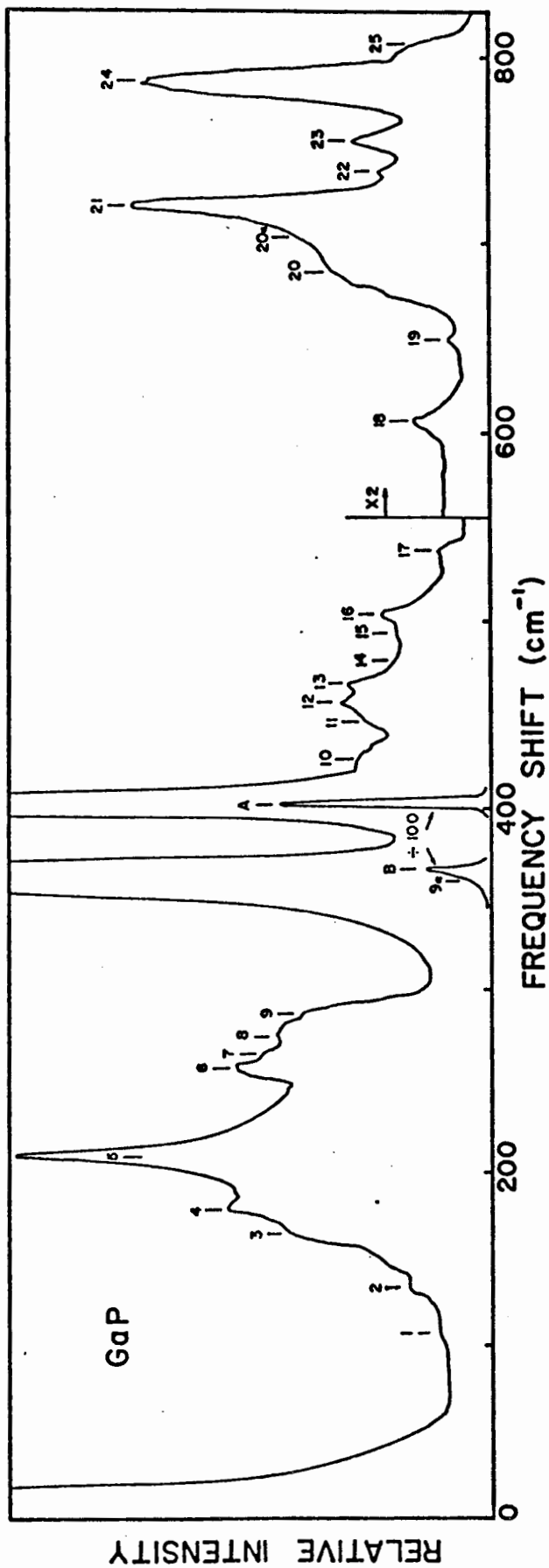

Figure 18 - The Raman spectrum of GaP at room temperature.

TABLE XVI

The frequencies (in cm^{-1}) and assignments of the Raman feature of GaP.

Feature Number from Figure 18	Frequency Shift Here	Frequency Shift I.R.(a)	Assignment	Frequency Shift Calculated for Table XIX	Error
1	105				
2	134		TO(L)-LA(L)	142	+12
3	166		LO(L)-LA(L)	171	+15
4	180		2TA(L)	186	+6
5	211		2TA(X)	208	-3
6	258		(LO(X)or TO(X))-TA(X)	262	+4
7	265		TO(L)-TA(L)	267	+2
8	276				
9	287		LO(L)-TA(L)	292	+5
9a	~355		TA(X)+LA(X)	350	-5
10	428	426	2LA(X)	428	0
11	446	446			
12	452		TO+TA(L)	453	+1
13	465		(LO(X)or TO(X))+TA(X)	470	+5
14	480	471	LO(L)+TA(L)	478	+2
15	495	493	2LA(L)	492	-3
16	504				
17	537	538	W_8+W_4	539	+2
		559			
		575	TO(L)+LA(L)	574	-1
18	606	604	(TO(X)or LO(X))+LA(X)	612	+8
19	649				
20	685				
20a	702	707	TO(L)	720	-13
21	720	722	2TO(X)	732	+12
22	738	738	$2W_8$, $2W_4$	618	0
23	754	754	LO(L)+TO(L)	745	-9
24	786	784	2LO(L)	770	-16
25	804	806	2LO(Γ)	806	+2

(a) Kleinman and Spitzer.

to be ($|e_s| = 0.64e$). This means that the binding in GaP is not very ionic. By considering the trends observed by Keyes (1962) which will be discussed later in section 7, the optic modes were expected to be approximately equal to each other at the zone boundary, or they might perhaps even cross. As a start the optic modes have been assumed to be equal at the critical point X and have been tentatively assigned as features 21 in Figure 18.

Since the laser frequency was well below the band gap of GaP strong $2\tilde{\nu}_{LO}(\Gamma)$ resonance was not expected as was observed in ZnTe and ZnSe. A relatively weak $2\tilde{\nu}_{LO}(\Gamma)$ mode was observed as feature 25. The features 20 to 24 were assigned to optic mode overtones and sums from X and L. The features numbered 4 and 5 were tentatively assigned to the overtones of TA(L) and TA(X) respectively. The features between 400 and 500 cm^{-1} were considered to be LA overtones and sums between the optic and acoustic modes.

To make a more quantitative interpretation the S.N.I. model has again been used to treat the data. The analysis follows the same line indicated for the case of ZnSe discussed in section 6.3. The measured elastic constants used in this fit and the set of parameters arrived at for the case of GaP have been listed in Table IX. The resulting frequencies at the critical points in GaP are tabulated in column 3 of Table XVII. These frequencies have been used to determine the assignments given in column 3 of Table XVI. One can see from Table XVI that the fit as a whole is fairly good. A couple of weak fea-

TABLE XVII

Critical point frequencies for GaP in cm^{-1}.

Critical Point	Mode	S.N.I. Model	Neutron[1]	I.R.[2]	I.R.[3]	Raman[4]
Γ	LO	402.8		405		402
	TO	366.6		366.5		366
X	LO	366	366	395	378	358
	TO	366	353	366	361	393
	LA	246	249	255	197	235
	TA	104	106	104	115	104
L	LO	385	373		378	360
	TO	360	357		361	378
	LA	214	212		197	236
	TA	93	85		66	76
W	W_1	109				
	W_2	178				
	W_3	197				
	W_4	361				
	W_5	368				
	W_6	369				

([1]) Yarnell et al, 1968. ([2]) Dean, 1967. ([3]) Kleinman and Spitzer, 1960. ([4]) Russel, 1965.

tures, numbers 1 and 19, were not accounted for by the model. Features 2, 3, 6, 7 and 9 were assigned as difference frequencies. Also no assignment has been given for feature 20 on the shoulder of feature 21.

The agreement of the calculated elastic constants with those measured, C_{11}, C_{12} and C_{44} are 5%, 15% and 35%, respectively. This agreement is not as close as obtained for ZnSe or ZnTe; however, it should also be noted that GaP is less ionic than either ZnSe or ZnTe; also GaP is the only III-V compound investigated here.

The critical point frequencies reported by other authors for GaP are also listed in Table XVII. Russel (1965) has assumed a strong crossing of the optical modes in the X direction; this is inconsistent with the S.N.I. model. Both Kleinman and Spitzer (1960) and Russel (1965) assigned TA(L) much lower than reported here. Dean (1967) and Kleinman and Spitzer (1960) in their far infra-red studies of GaP assigned LO(X) higher than TO(X) in contrast to the results presented here. Also listed in Table XVII are the critical point frequencies measured directly by neutron scattering by Yarnell et al. (1968). The assignments made using the S.N.I. model agree reasonably well with these values. The largest difference occurs for the TA(L) mode where the discrepancy is about 9%. Otherwise the agreement between the measurements is within 4%.

CHAPTER 7

DISCUSSION

7.1 Introduction

In this chapter the consistency of the frequency assignments made to the Raman features observed for ZnTe, ZnSe and GaP are checked against regularities that have been previously observed in the phonon spectra of zincblende semiconductors. The Brout sum rule is applied to these results as a test of their consistency. Also the application of the S.N.I. model to the analysis of the Raman spectrum of zincblende materials and the information obtainable from polarization studies of the Raman spectrum will be discussed.

7.2 Regularities in Zone Boundary Phonon Spectra

The phonon spectra of several zincblende semiconductors have been analyzed by Keyes (1962), Mitra (1963) and Marshall and Mitra (1964). Most of these spectra were obtained from infra-red absorption spectra and the frequencies obtained represent some average of the zone boundary frequencies from the various critical points. They have found certain regularities in the various spectra and the assignments made here can be checked by comparing them to these regularities.

Keyes (1962) and Mitra (1963) found a strong correlation between the ratio $(\nu_{LO}/\nu_{TO})^2$ at the zone boundary and the ionicity or effective charge ratio (e_s^*/e) squared. The qualitative origin of this correlation is illustrated in Figure

19 taken from Mitra (1963). Figure 19(a) is typical of silicon in which $e_s^*/e=0$: here the zone centre optic modes are degenerate and $\tilde{\nu}_{TO} < \tilde{\nu}_{LO}$ throughout the remainder of the Brillouin zone.

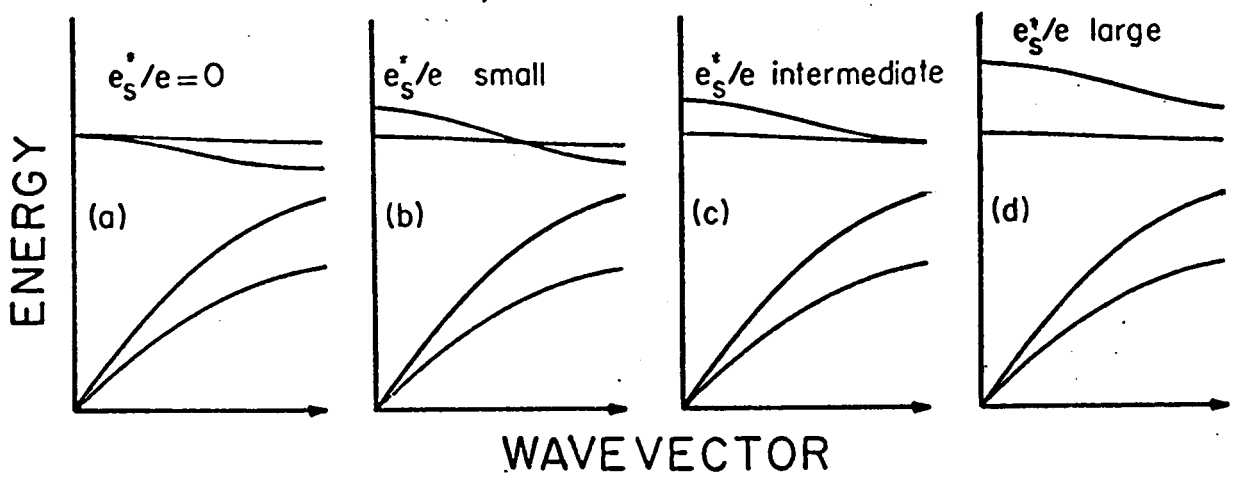

Figure 19 - A qualitative illustration of the effect of ionicity on the phonon dispersion of a diatomic lattice.

For e_s^*/e small, the degeneracy at Γ is partially removed but the optic modes cross within the B.Z. as in Figure 19 (b). At some intermediate ionicity, $e_s^*/e \cong 0.7$, the optic modes are degenerate at the zone boundary and for large ionicity the optic modes do not cross within the B.Z. This correlation has been used in making tentative assignments of the optic modes in the Raman spectra. Figure 20 is a graph of the correlation for several zincblende materials taken from a paper by Marshall and Mitra (1964) in which asterisks have been placed corresponding to the results obtained here. The ionicity of the compounds studied were calculated using equation (3.1) and the dielectric constants of Table VII. One can see that the asterisks fit well on this graph. Two other graphs have been taken from a paper by Mitra (1963) and the corresponding asterisks added to them. The

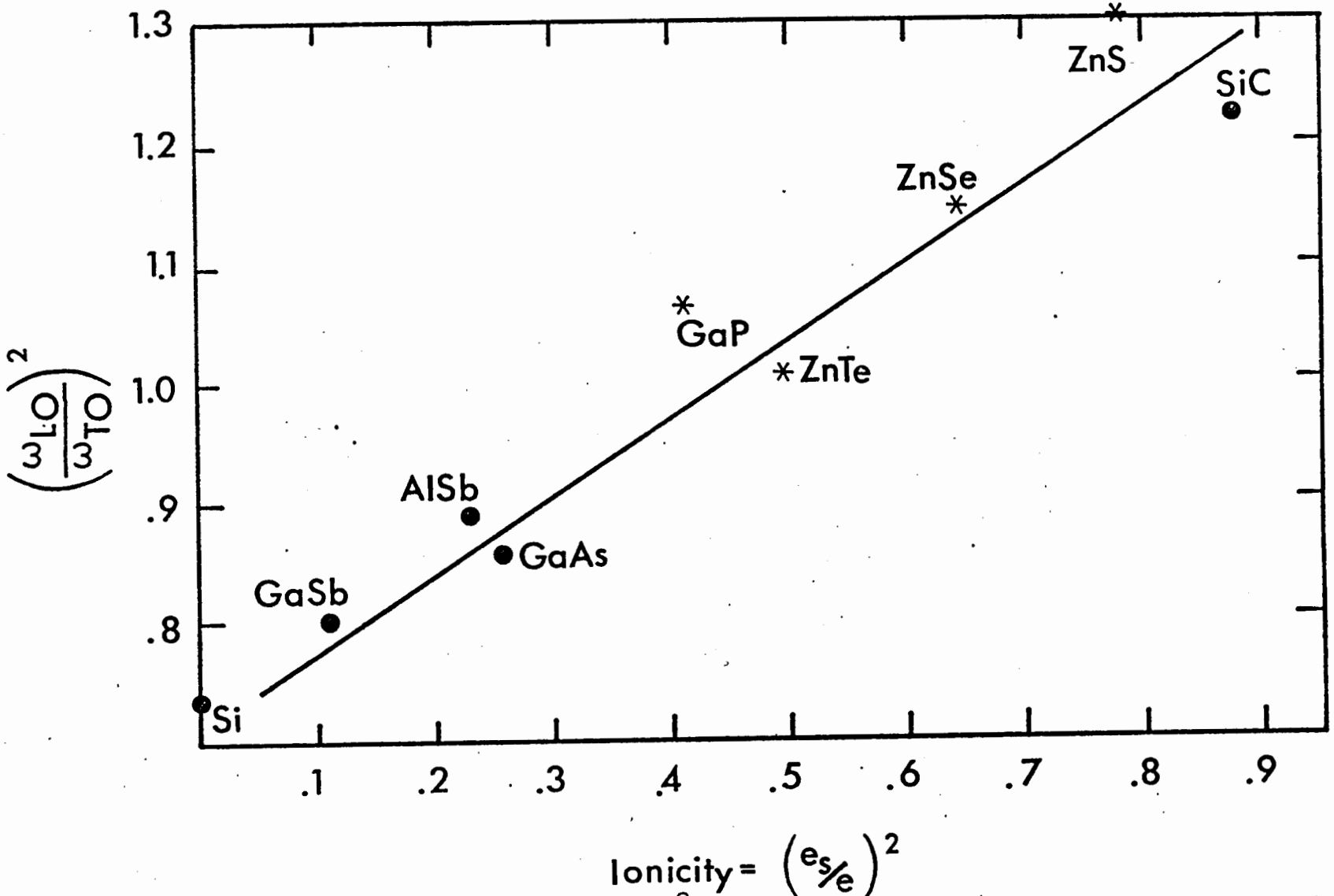

Figure 20 - A plot of $(\tilde{\nu}_{LO}/\tilde{\nu}_{TO})^2$ versus ionicity for some zincblende semiconductors (from Marshall and Mitra, 1964).

The first of these (Figure 21) is a plot of $\tilde{\nu}_{LA}$ versus $\tilde{\nu}_{TO}$ and the second (Figure 22) is a plot of $\tilde{\nu}_{TA}$ versus $\tilde{\nu}_{LO}$. It should be mentioned that the reproductions of these graphs do not contain all the points given by Mitra (1963) and Marshall and Mitra (1964) but only representative points since the data which have been plotted represent averages of the values at the critical points X and L. It can be seen that the values obtained here correlate well with the results obtained for other zincblende compounds.

The effective charge calculated from Szigeti's formula is compared to that obtained from the S.N.I. model for the four materials studied here (Table XVIII). It can be seen that there is a close agreement between the two determinations of effective charge, the largest difference being 9%. The agreement is best for the most ionic material ZnS and poorest for the least ionic materials.

TABLE XVIII

The ionicity of some zincblende compounds calculated from the Szigeti equation and from the S.N.I. model.

Effective Charge Ratio	ZnTe	ZnSe	ZnS	GaP
e_s^*/e	.71	.80	.88	.64
Z	.76	.83	.91	.57
Difference	7%	4%	3%	9%

7.3 The Sum Rule

A sum rule initially introduced by Brout (1959) for

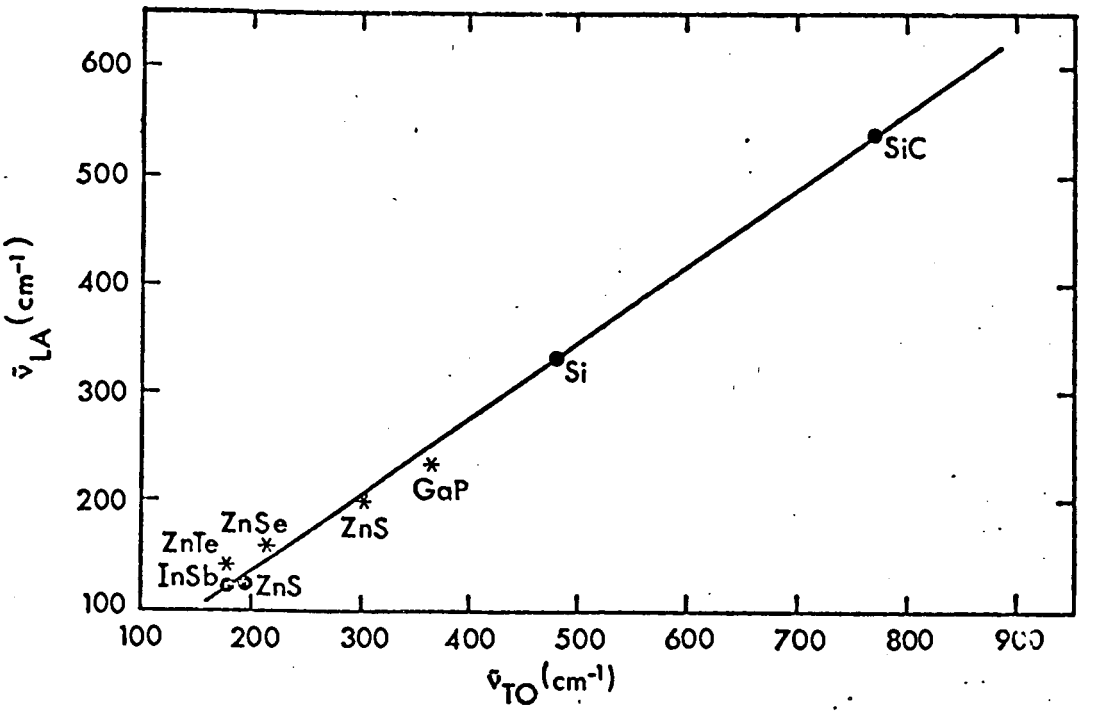

Figure 21 - A plot of $\tilde{\nu}_{LA}$ versus $\tilde{\nu}_{TO}$ for several zincblende semiconductors (from Mitra, 1963).

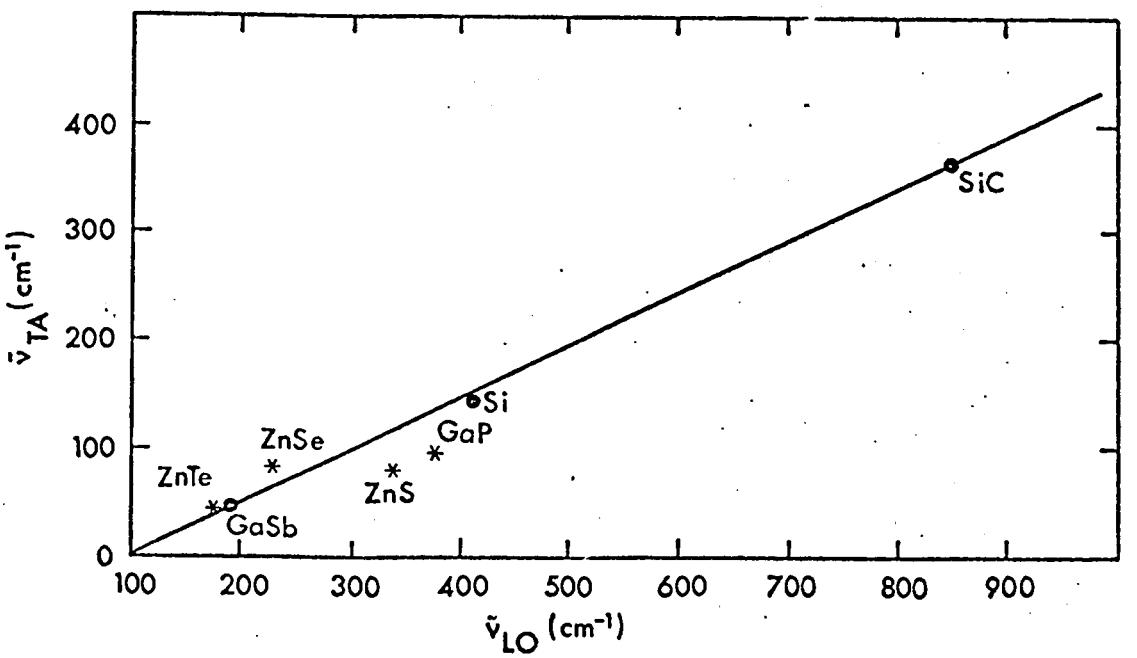

Figure 22 - A plot of $\tilde{\nu}_{TA}$ versus $\tilde{\nu}_{LO}$ for some zincblende semiconductors (from Mitra, 1963).

ionic diatomic crystals with the NaCl structure has been extended by Rosenstock (1963&1965) and Rosenstock and Blanken (1966) to include any n-atomic lattice of any structure. Rosenstock has stated the sum rule in the following form:

$$\sum_{i=1}^{n} \omega_i^2(\vec{q}) = \text{constant} + \sum_k \beta_k \Psi^k(\vec{q}) \qquad (7.1)$$

The sum on the left is taken over the n-phonon branches at point $\vec{q}$ in the Brillouin zone and the sum on the right is over the k forces acting between atoms in the crystal. $\Psi^k(\vec{q})$ thus represents the $\vec{q}$ dependent contribution of the k^{th} force. Rosenstock has shown that the only forces contributing to the $\vec{q}$ dependent part of the sum are nonelectrostatic and act on like atoms. Thus first neighbour interactions and long range Coulomb forces do not contribute to $\Psi(\vec{q})$ and only second and more distant neighbour forces prevent the sum from being a constant.

In this work a second neighbour theoretical model has been applied to the lattice vibrations of zincblende materials and a set of frequencies has been obtained from this model which agree quite closely with those necessary to describe the second-order spectrum for each material studied. With this close agreement one can expect good accord between these results and the predictions of Rosenstock for the second neighbour force contribution to the sums at the zone boundary. The sums at the zone boundary will thus be somewhat higher than they are at the center and although the difference is not quantitatively predicted by Rosenstock's theory it is perhaps of interest to calculate

$$\Delta(\vec{q}) = \frac{\sum \omega_i^2(q) - \sum \omega_i^2(\Gamma)}{\sum \omega_i^2(\Gamma)} \qquad (7.2)$$

at the zone boundary. This has been done and the values obtained along with the Brout sums at the critical point are listed in Table XXI. For comparative purposes the neutron work on GaP by Yarnell et al. (1968), and the work on GaAs by Waugh and Dolling (1963) have been included in Table XIX. It can be seen from the table that in all cases $\Delta(X) \cong \Delta(W)$ and the value of $\Delta(L)$ is about 3/4 that of $\Delta(X)$. The sums calculated from the analysis of the Raman spectra are somewhat larger than the sums calculated from the neutron data. Also it appears that the more ionic compounds ZnSe and ZnS have larger second neighbour force contributions to the sums at the zone boundary than the less ionic compounds ZnTe and GaP. This analysis of the Raman spectra of zincblende compounds appears to give reasonable values for the Brout sums at the zone boundaries and also adds weight to previous observations (Waugh and Dolling, 1963 and Rosenstock and Blanken, 1966) that second neighbour forces are essential for an adequate treatment of the lattice dynamics of zincblende materials.

TABLE XIX

The Brout sums at the critical points.

Material	$\sum \omega_i^2(\vec{q})$ ($\times 10^{27}$ sec.$^{-1}$)							
	Γ	X	L	W	Δ(X)	Δ(L)	Δ(W)	Z
ZnTe	3.79	4.25	4.14	4.25	.12	.09	.11	.76
ZnSe	5.15	6.60	6.24	6.6	.28	.21	.28	.83
ZnS(a)	9.62	12.4	11.68	12.4	.29	.21	.31	.91
GaP	15.3	17.2	16.73	17.0	.12	.09	.11	.70
GaP(b)	15.3	16.6	16.16		.08	.05		.70
GaAs(c)	7.95	8.89	8.68		.12	.09		.57

(a) Irwin, 1970; (b) Yarnellet al., 1968; (c) Waugh and Dolling, 1963.

7.4 Methods of Analysis and Discussion

In the past the Raman spectra of zincblende compounds have been analysed by assigning the Raman features largely by guess-work. Researchers assumed that essentially all the scattering took place at the B.Z. boundary and interpreted their results in terms of a set of four average frequencies at the zone boundary. Obviously the results of such an exercise were not unique and often several possible sets of values were given.

In this thesis a theoretical model, the S.N.I. model, has been applied in making the assignments to the features observed in the Raman spectra of ZnTe, ZnSe and GaP. There are only seven parameters in this model and by using the measured elastic constants as a constraint there is a limited range of possible fits of the model to the observed Raman features. By

varying the parameters of the model a "best fit" was obtained and the assignments to the Raman features were made accordingly. These assignments were checked and found consistent with regularities in the phonon spectra observed by previous authors. The assignments were also found consistent with the Brout sum rule.

The S.N.I. model was found suitable for such an application to the zincblende structure: (a) it takes into account an effective charge of the ions of the material (b) it includes second neighbour interactions found necessary from an application of the Brout sum rule (c) it involves only seven physically significant parameters such that when constrained by the lattice constants of a material it allows only a limited range of possible solutions.

Another method used to analyse the Raman spectra of zincblende materials is the study of the polarization properties of oriented single crystalline samples. However if one attempts to make assignments to the Raman features based upon the observed polarization properties, one is immediately confronted with difficulties: from Table V it can be seen that for the critical points X and L there are twenty possible second order modes for which there are only five distinguishable polarization selection rules ($\Gamma_1+\Gamma_{12}$, $\Gamma_1+\Gamma_{15}$, $\Gamma_1+\Gamma_{12}+\Gamma_{15}$, $\Gamma_{12}+\Gamma_{15}$ and Γ_{15}). This lack of discernment together with the similarity of the observed polarization characteristics of the spectrum makes this method of assigning the Raman features by itself rather dubious.

For example, Nilsen (1969) and Krauzman (1969) have each analyzed the Raman spectrum of ZnS by this method. If one compares their results one finds rather poor agreement in their assignments. Nevertheless, the observation of oriented single crystalline samples with particular incident and scattered light polarization allows a better separation to be made of the contributing processes in the Raman spectrum.

Thus to obtain definitive information from a second order Raman spectrum it has been found necessary to use an appropriate lattice dynamic model. In this way it is believed that a reliable set of values can be obtained for the critical point vibrational frequencies. Also, even though polarization studies are not sufficient in themselves, they should be used whenever possible to aid in the interpretation of the results.

CHAPTER 8

PHONON DISPERSION

8.1 Introduction

In this chapter the S.N.I. model parameters obtained above are used to calculate the phonon dispersion (section 8.2), the frequency distribution (section 8.3) and the specific heat (section 8.4) for ZnTe, ZnSe, ZnS and GaP. Comparisons are made with measured results where possible.

8.2 Phonon Dispersion Curves

The parameters of the S.N.I model derived from treating the second order spectrum have been used to calculate the phonon dispersion throughout the B.Z. In doing this it is necessary to consider only that region $\mathcal{R}$ in the B.Z. defined by

$$0 \leq q_z \leq q_y \leq q_x \leq 1 \quad ; \text{ and } \quad q_x + q_y + q_z \leq 3/2$$

The application of the symmetry properties of the zincblende structure to $\mathcal{R}$ will generate the entire B.Z.

It is convenient to introduce the numbers P_x, P_y, P_z such that $P_x = 40 q_x$, $P_y = 40 q_y$, $P_z = 40 q_z$ so that possible $\vec{q}$ vectors in reciprocal space are given by

$$\vec{q} = \frac{\pi}{2a} \cdot \frac{1}{40} \left(P_x, P_y, P_z \right)$$

An even sampling of points in $\mathcal{R}$ is obtained by letting P_x, P_y, P_z be integers, either all odd or all even to account for the lattice geometry and such that

$$0 \leq P_z \leq P_y \leq P_x \leq 40 \; ; \text{ and } \; P_x + P_y + P_z \leq 60.$$

There are 1685 sets of numbers of this type representing wavevectors evenly distributed throughout the region $\mathbb{R}$ possessing all the symmetry properties of the reciprocal space. Equation (3.7) is solved for the vibrational mode frequencies at each of these wavevectors. This has been done using a high speed computor and a program obtained from Dr. V. P. Varshni of the University of Ottawa. The phonon dispersion of ZnTe, ZnSe, ZnS and GaP have been calculated and plotted in Figures 23 to 26 respectively. ZnS has been included because of its similarity to the other zincblende compounds studied here. The S.N.I. model parameters which were used for ZnS were obtained from Irwin (1970). In Figures 23 to 26 not only have the frequencies and wavevectors been included between Γ and the critical points X, L and W but also the zone boundary values between the symmetry points X, L, W and K. The abcissa axis is linear in wavevector magnitude between the symmetry points. One can see that there is a strong similarity in the phonon dispersion of the four materials as can be expected from materials of the same structure.

The neutron scattering data for the acoustic lattice vibrations in ZnS was measured by Feldkamp et al. (1969) and has been included in the phonon dispersion curves of Figure 25. Only partical agreement has been found between the calculated results and those measured by neutron scattering. Unfortunately Feldkamp et al.(1969) did not include any statement indicating the accuracy of these measurements; however, they did say that they had only a small crystal of 1.44 cm^3 volume and that there

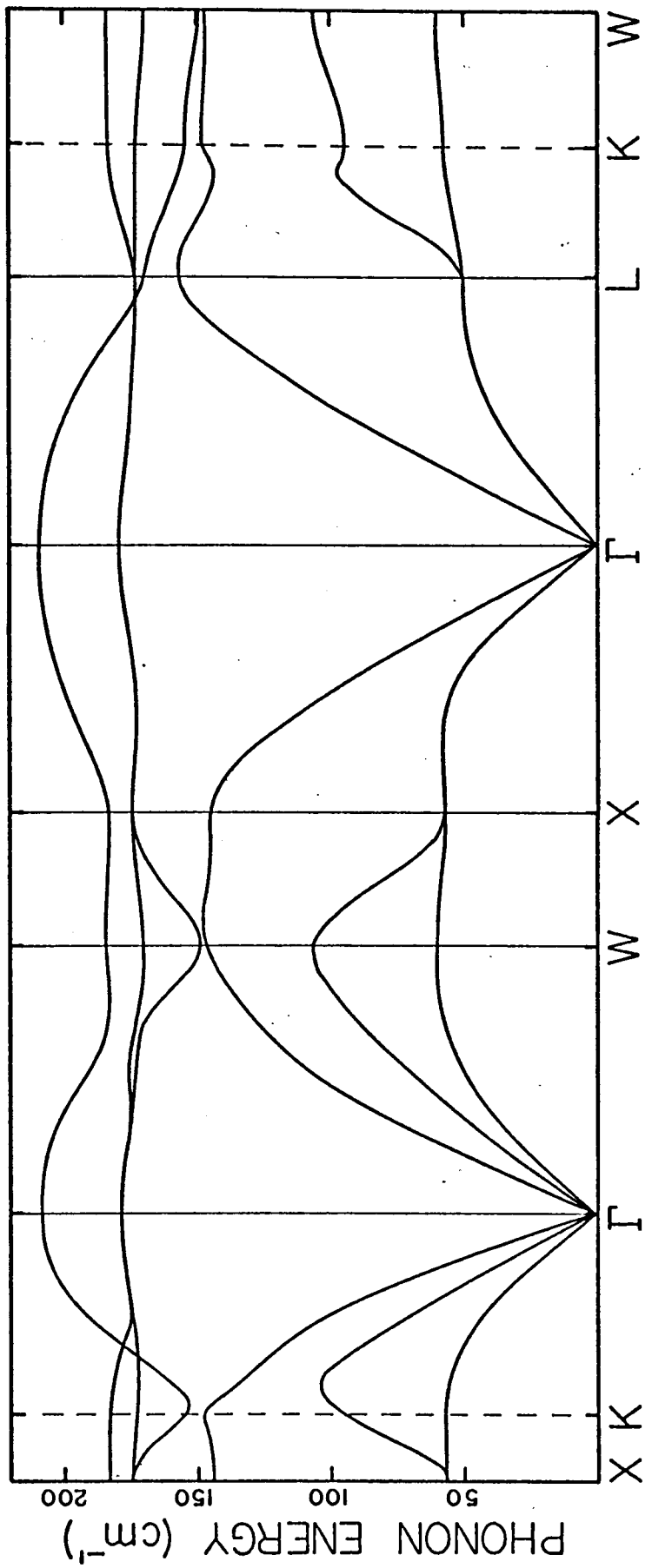

Figure 23 - The phonon dispersion of ZnTe.

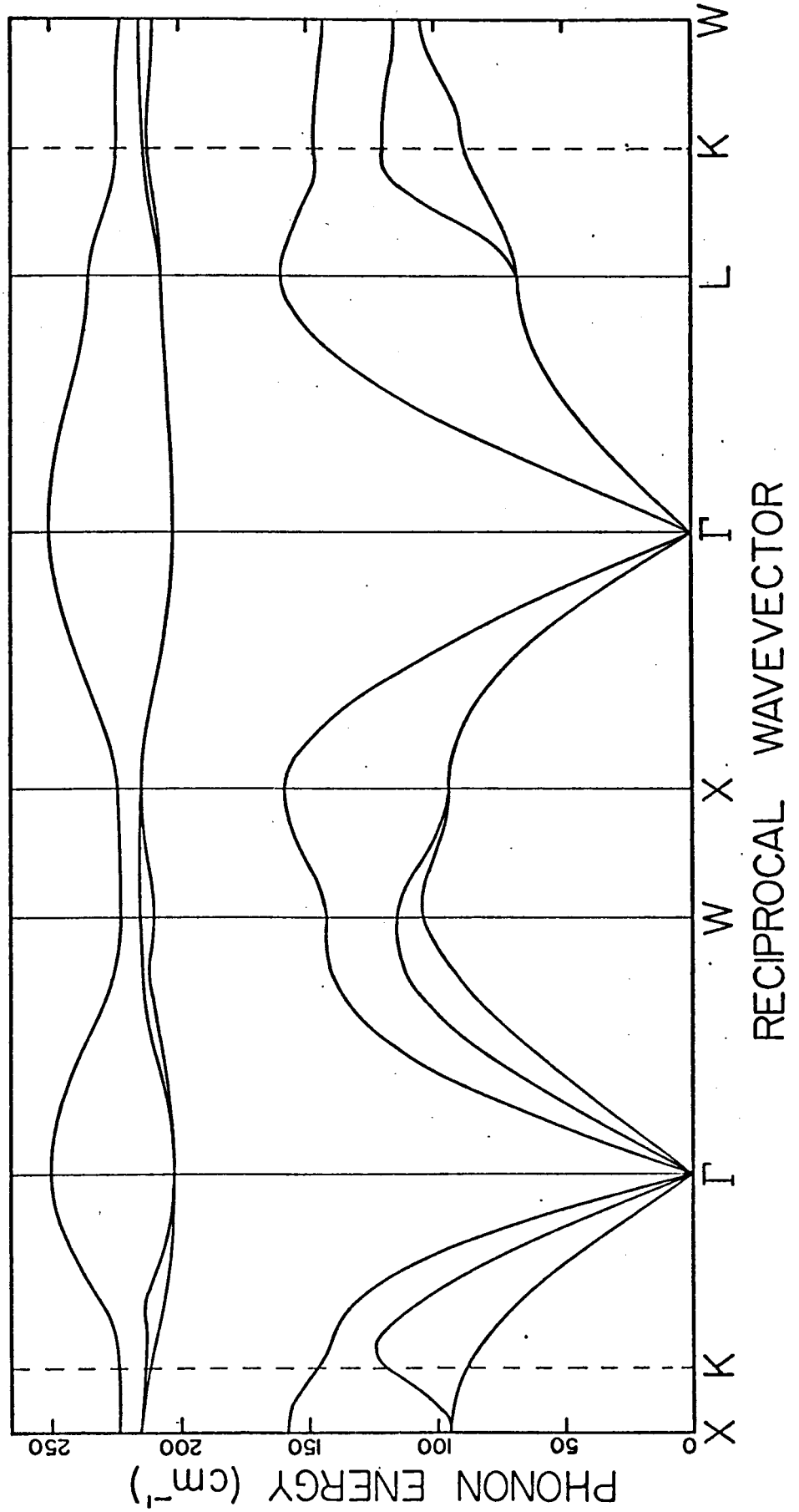

Figure 24 - The phonon dispersion of ZnSe.

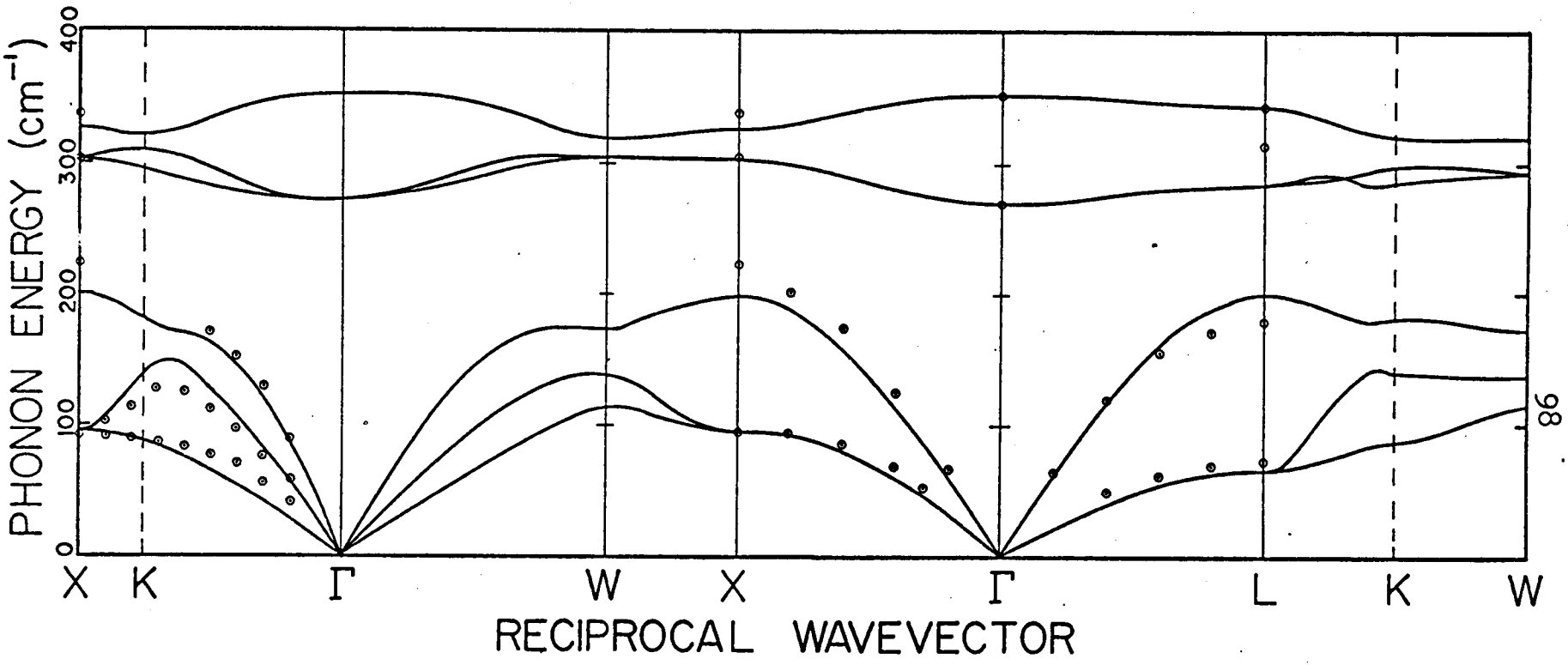

Figure 25 - The phonon dispersion of ZnS.

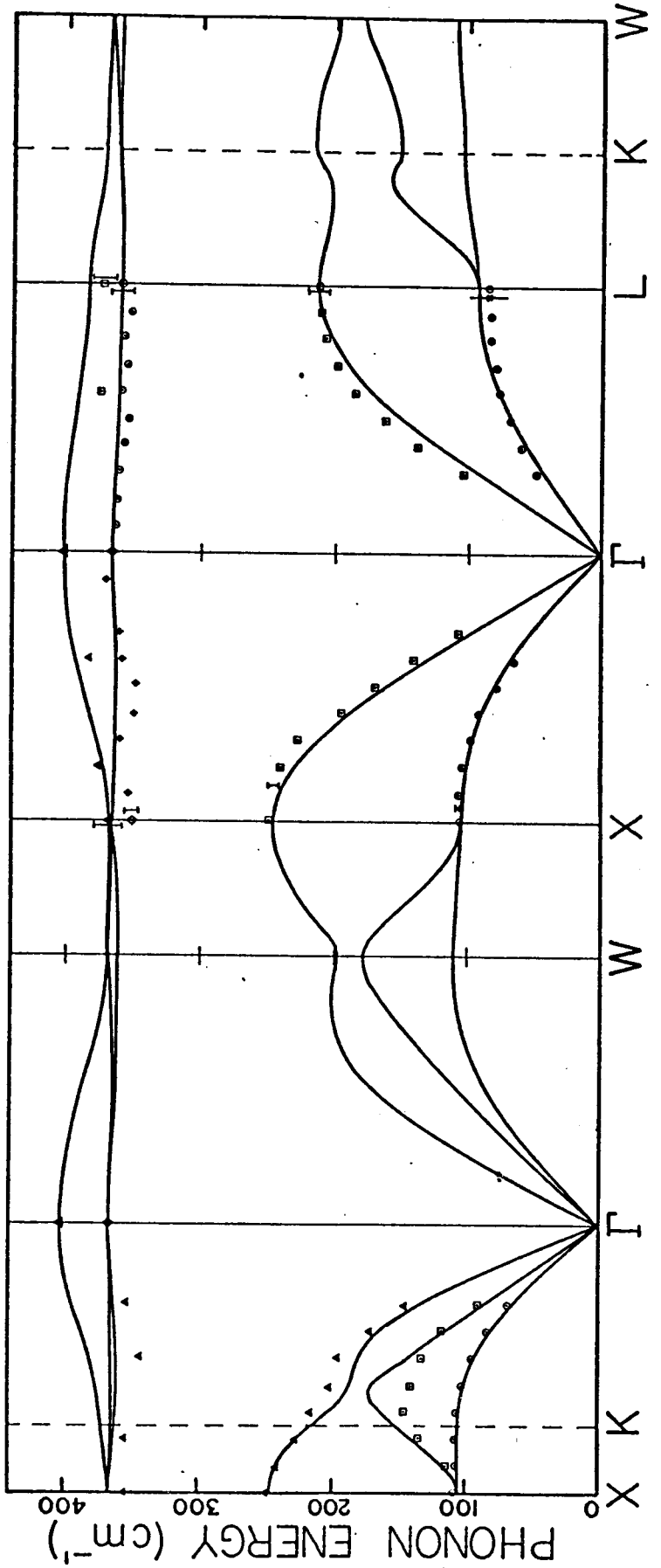

Figure 26 - The phonon dispersion of GaP.

was insufficient intensity to measure the optical mode frequencies. Because of this the accuracy of their results must be held suspect and cannot be considered as a test of the calculated dispersion curves.

In figure 26 the neutron scattering data from measurements on GaP by Yarnell et al.(1968) have been included. Error bars have also been included to indicate the accuracy stated by Yarnell et al. The agreement between calculated and measured dispersion curves is reasonably good although parts of the calculated curves fall outside the stated experimental accuracy of the neutron data. However, it is felt that the accuracy of this scattering data must be held suspect too. Consider the strong feature 24 in the GaP Raman spectrum of figure 18. This is a 2LO mode which has been assigned to the critical point L. This feature implies a vibrational mode of 393±5 cm^{-1}. The neutron data is unable to account for a vibrational mode frequency this large other than at the zone centre. However the contribution from the zone centre LO mode to the Raman spectra is clearly feature 25. Also it should be noted that although the sample of GaP studied had a volume of ~9 cm^3, the sample was a composite of 36 single crystal platelets oriented and glued together. For these reasons it is felt that the experimental error in the neutron scattering data stated by the authors is perhaps too small and could easily be twice as large.

8.3 The Frequency Distribution of the Vibrational Modes

In order to calculate the frequency distribution of the vibrational modes of a material, the mode frequencies cal-

culated using equation (3.7) and the values of p_x, p_y, p_z above must be weighted according to the number of similar points in the whole Brillouin zone. The frequency distribution, $g(\nu)$, can be derived from the calculated frequencies by dividing the range of values of ν into equal intervals $\Delta\nu$ and counting the number of frequencies in each interval. The frequency distribution for ZnTe, ZnSe, GaP and ZnS have been calculated and the results appear in Figures 27 to 30 respectively. One must bear in mind that these frequency distribution functions are only approximations. Because of the discrete sampling of modes (for example, there are only twenty wavevectors sampled between Γ and X), one does not get a true picture of (a) the higher density of states due to the volumetric effect of increasing wavevector, and (b) the high density of state due to the flattening of the dispersion curves at or near the critical points. To illustrate this the density of states function for ZnS has been calculated using only values of $p_x + p_y + p_z = 60$ and 59, i.e. zone boundary and near zone boundary frequencies. The results reflect the high density of states for large wavevector and are illustrated in Figure 31. Comparing Figures 30 and 31 one sees the major difference is the zone center optical frequencies and the frequencies near K inside the zone edge. These regions should have a low density of states compared to the zone boundary. In order to obtain a more accurate frequency distribution function it would be necessary to divide the range of $\vec{q}$ into much finer points to do the calculation. However, this rapidly becomes prohibitive in computer time, and negates this approach.

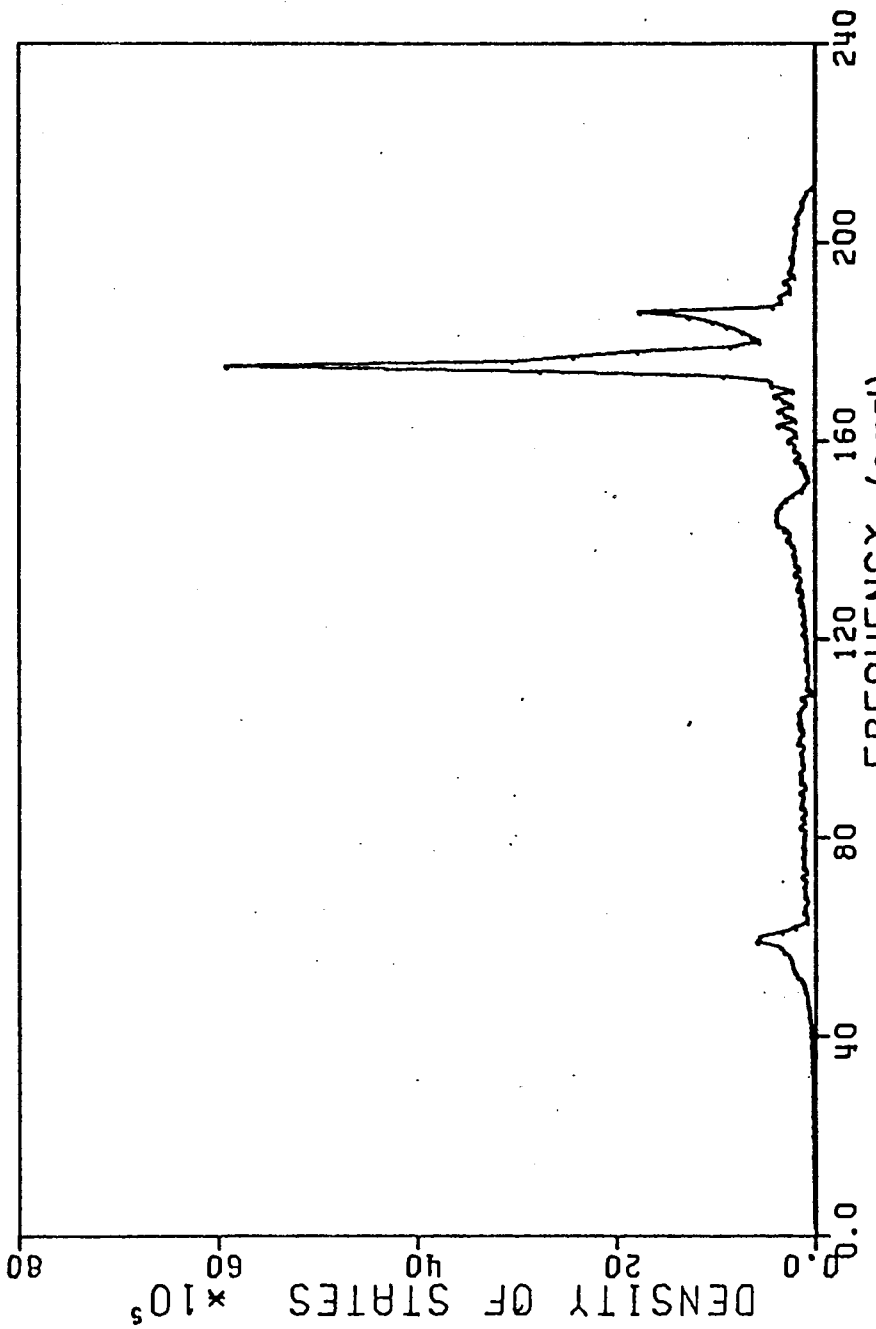

Figure 27 - The frequency distribution of vibrational modes in ZnTe.

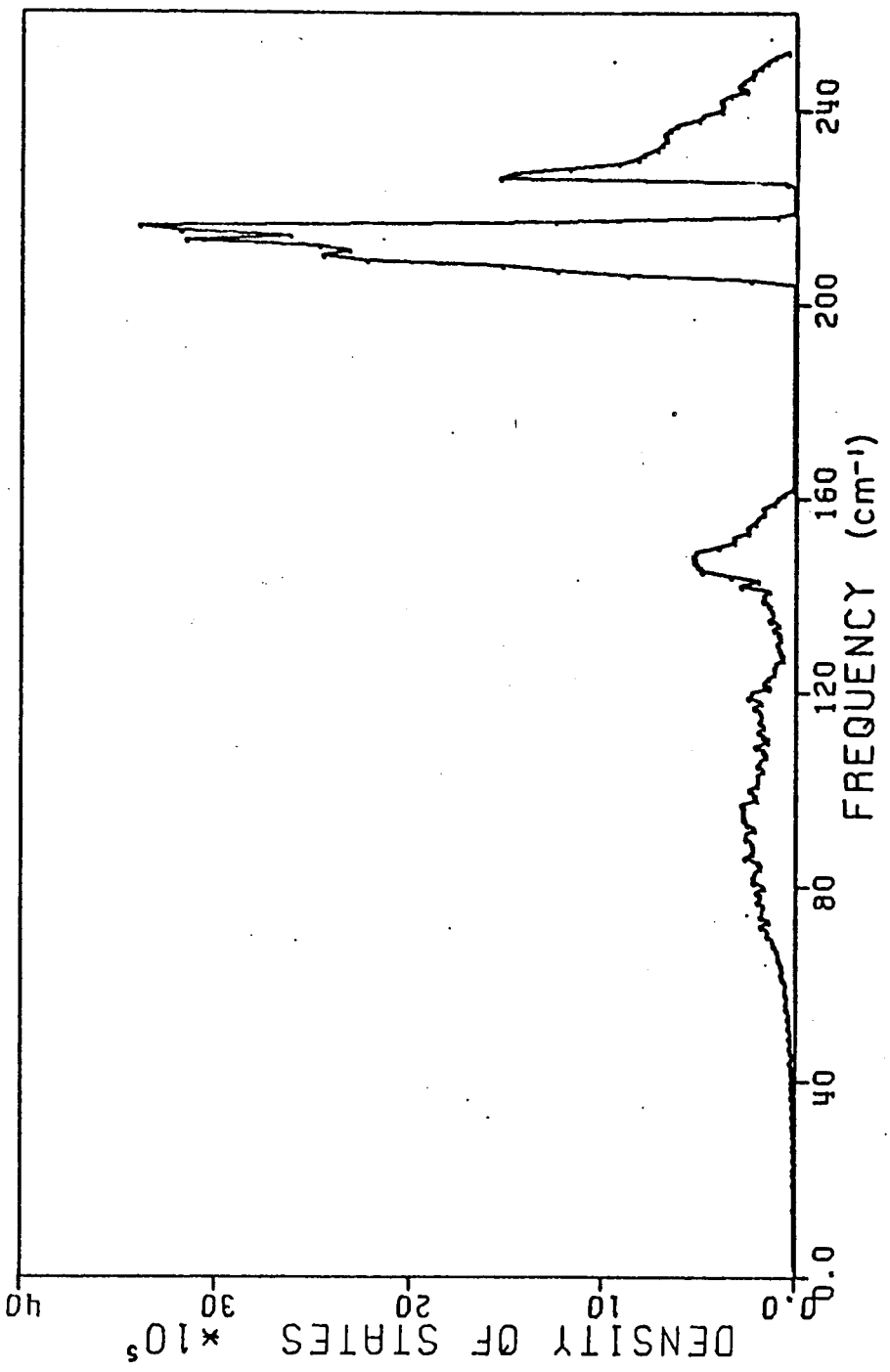

Figure 28 - The frequency distribution of vibrational modes in ZnSe.

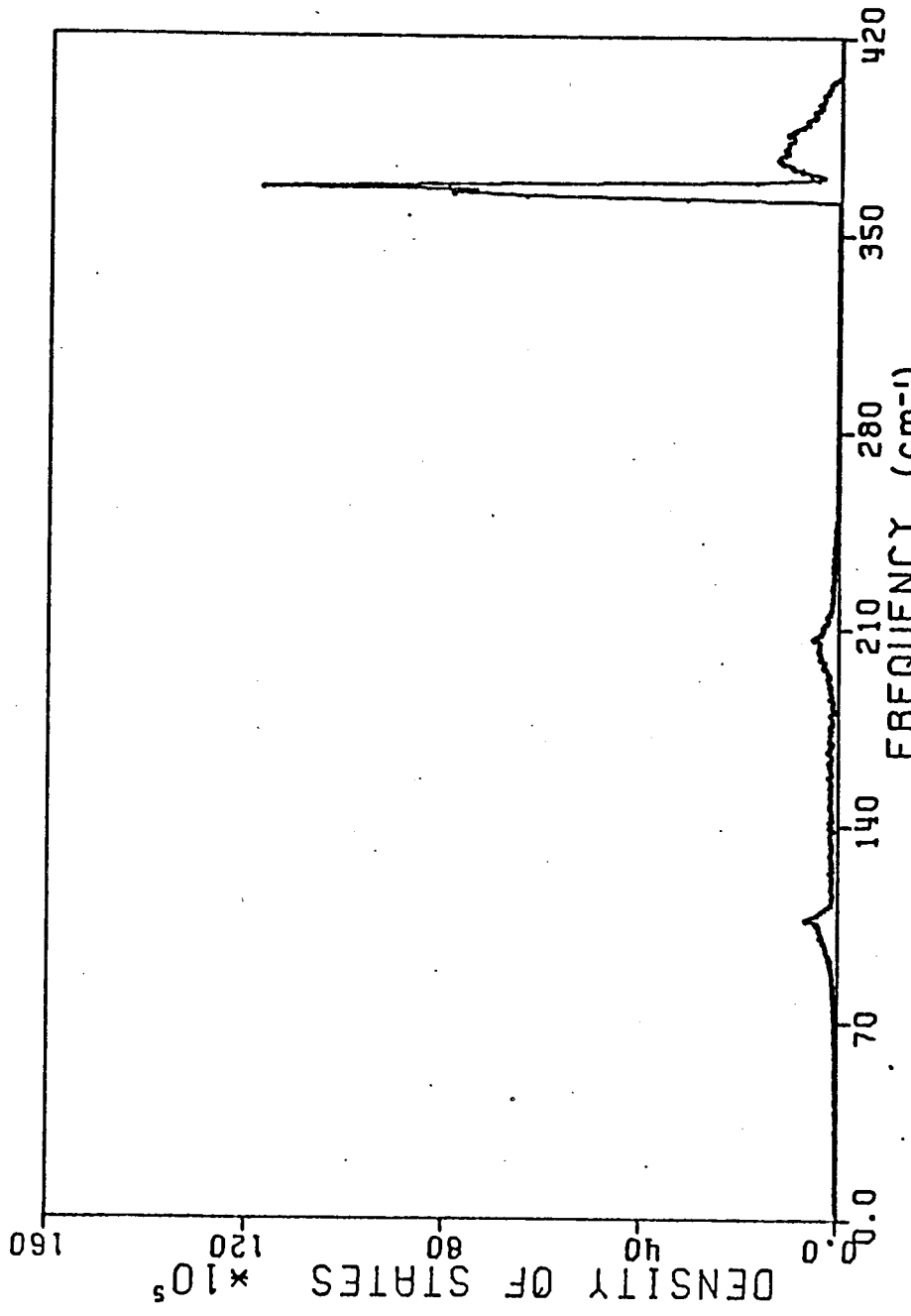

Figure 29 - The frequency distribution of vibrational modes in GaP.

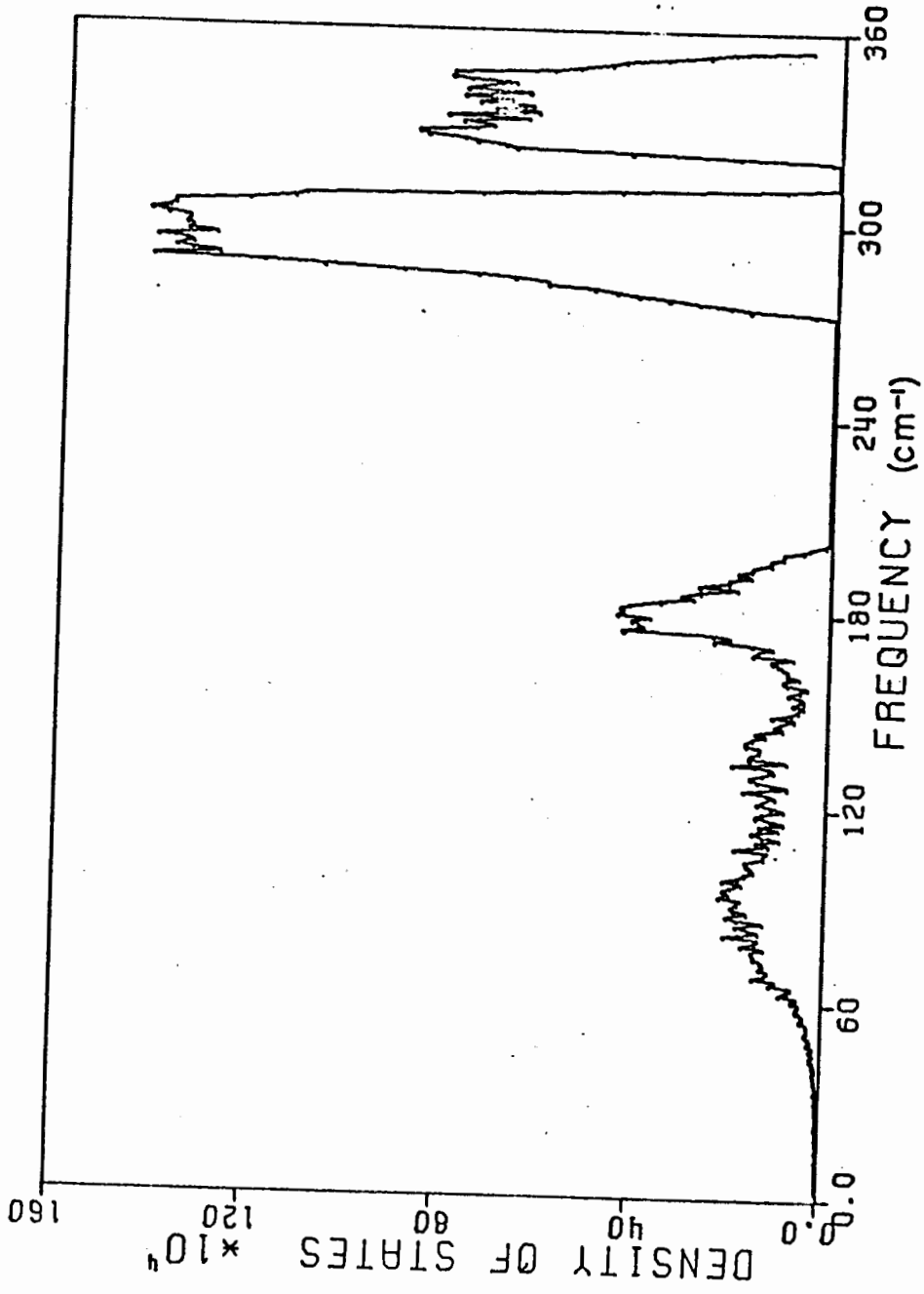

Figure 30 - The frequency distribution of vibrational modes in ZnS.

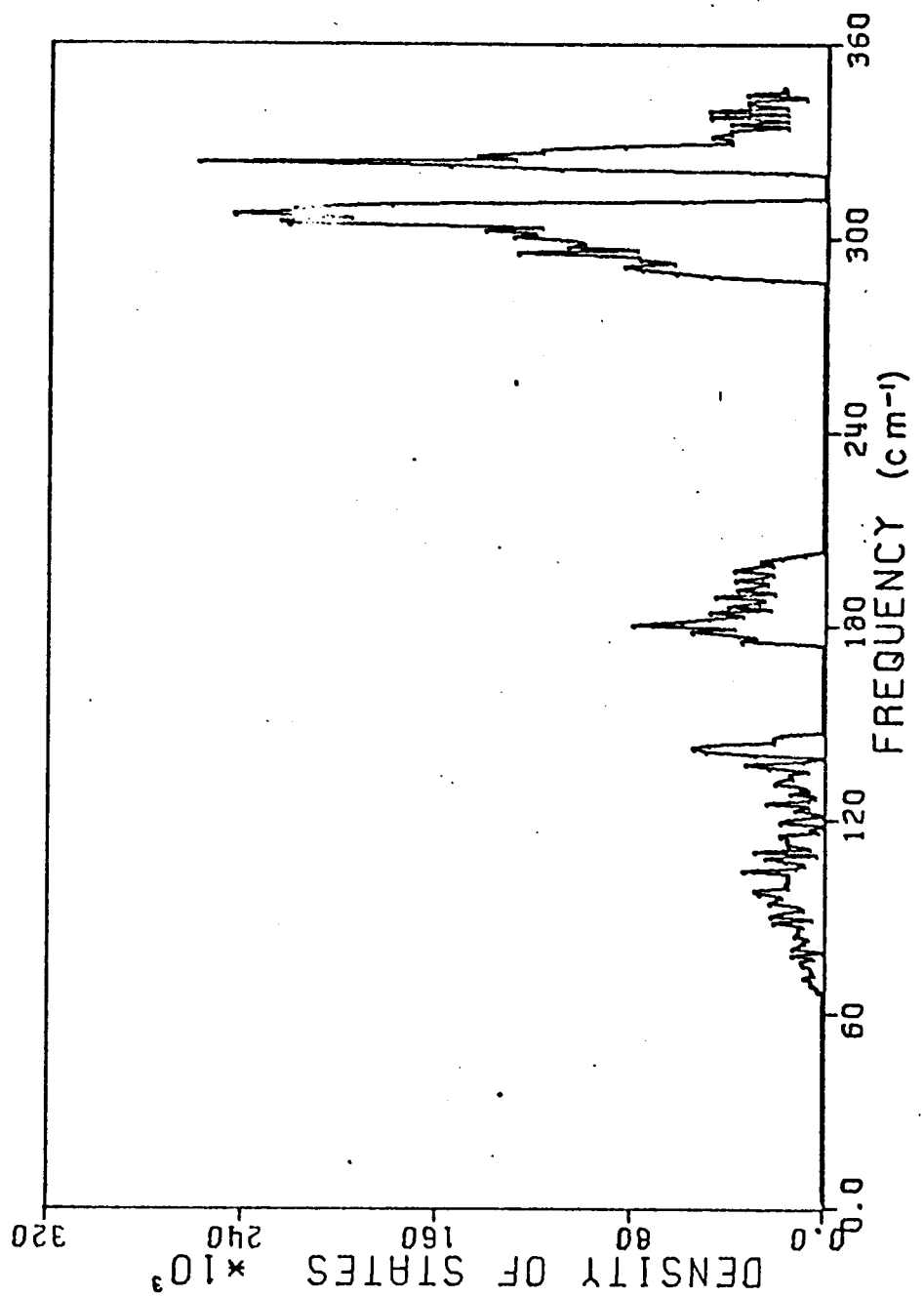

Figure 31 - The frequency distribution of the vibrational modes in ZnS with wavevectors near the B.Z. boundary.

8.4 The Specific Heat

The specific heat can be calculated from the density of states function $g(\nu)$ of the lattice modes. (Electron contribution to the specific heat is assumed negligible in the high resistivity semiconductors studied here.)

The thermal energy of a crystal is given by

$$E = \int g(\tilde{\nu})\, n(\tilde{\nu})\, hc\tilde{\nu}\, d\tilde{\nu}$$

where $$n(\tilde{\nu}) = \frac{1}{e^{\frac{hc\tilde{\nu}}{kT}} - 1}$$

and $$\int g(\tilde{\nu})\, d\tilde{\nu} = 6N$$

Here h is Planck's constants, k is the Boltzman constant, T is the temperature in °K, 6 is the number of modes per molecule or unit cell and N is Avogradro's number.

The specific heat for constant volume follows by differentiating the energy by temperature,

$$C_v = k \int g(\tilde{\nu}) \left(\frac{hc\tilde{\nu}}{kT}\right)^2 \frac{e^{\frac{hc\tilde{\nu}}{kT}}}{\left(e^{\frac{hc\tilde{\nu}}{kT}} - 1\right)^2}\, d\tilde{\nu}$$

and for purposes of numerical evaluation one can write

$$C_v = \frac{6Nk}{\eta} \sum_{\text{all modes}} \left(\frac{hc\tilde{\nu}}{kT}\right)^2 \frac{e^{\frac{hc\tilde{\nu}}{kT}}}{\left(e^{\frac{hc\tilde{\nu}}{kT}} - 1\right)^2}$$

where η is the total number of modes evaluated. Because all materials with the same number of modes per unit cell tend to the same value of specific heat at high temperatures it is advantageous for comparative purposes to express the specific heat $C_V(T)$ in terms of the Debye temperature $\Theta(T)$ of the material. The specific heat of a material with two atoms per unit cell is given in the Debye approximation by (Kittel, 1967)

$$C_v = 18\,N k \left(\frac{T}{\Theta}\right)^3 \int_0^{x_D} \frac{x^4 e^x}{(e^x - 1)^2}\, dx$$

where $$x_D \equiv \Theta/T \equiv \frac{hc\tilde{\nu}_D}{kT}$$

The frequency distribution of the vibrational modes is assumed to depend on the square of $\tilde{\nu}$ up to a cut-off frequency $\tilde{\nu}_D$ and is zero above. The specific heat for such a solid according to the Debye approximation is illustrated in Figure 32. For each temperature and material one can compare the calculated specific heat to that predicted by the Debye theory and obtain the corresponding Debye temperature $\Theta(T)$.

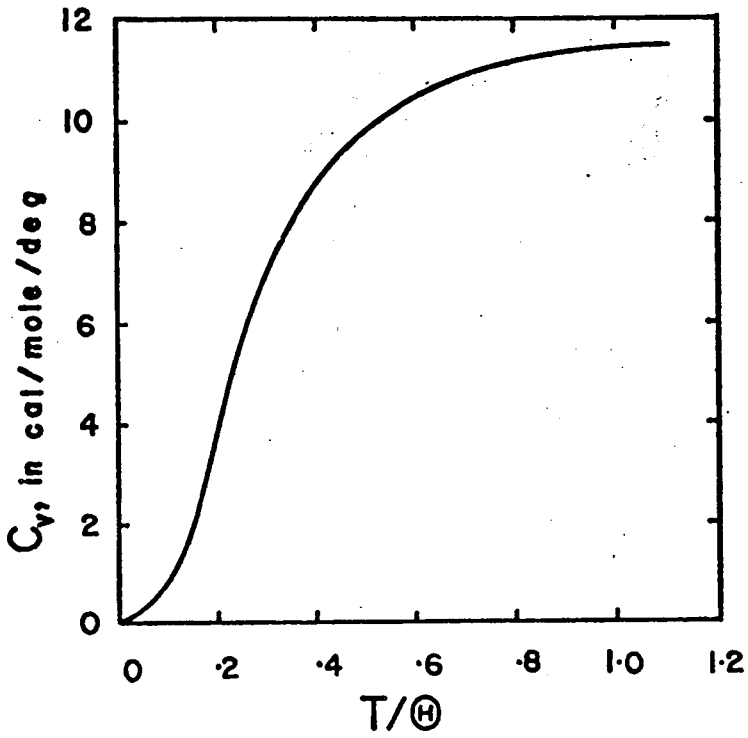

Figure 32 - The heat capacity of a solid with two atoms per unit cell, according to the Debye approximation.

The specific heat of each of the materials studied here have been calculated using the frequency distribution obtained from the S.N.I. model and has been expressed in terms of Debye temperatures in the range from 10°K to 500°K. The results are illustrated by the solid lines in Figure 33. Very little experimental data exists on the specific heat of these materials. In fact no experimental determination of the specific heat of GaP has been found. Experimental data for the other materials were added point by point in Figure 33.

The room temperature values of ZnTe and ZnS and the 80°K measurement of ZnSe are in strong disagreement with the calculated results. The data for ZnS taken from Gmelin (1956) fall reasonably well along the theoretical curve; but the room temperature determination by Schleiger and Webb (1968) for the same material falls 120K° below the calculated results. Gul'tyaev and Petrov (1959) report measured values of C_V for ZnTe and ZnSe with the associated Debye temperatures at 80°K. These values have been entered in Table XX with the results obtained here for comparative purposes.

TABLE XX

A comparison of the specific heats for ZnTe and ZnSe at 80°K.

	Gul'tyaev and Petrov		Here	
	C_V (cal/gm-atom/°K)	Θ (°K)	C_V (cal/mole/°K)	Θ (°K)
ZnTe	3.8	250	7.61	252
ZnSe	2.2	400	6.42	302

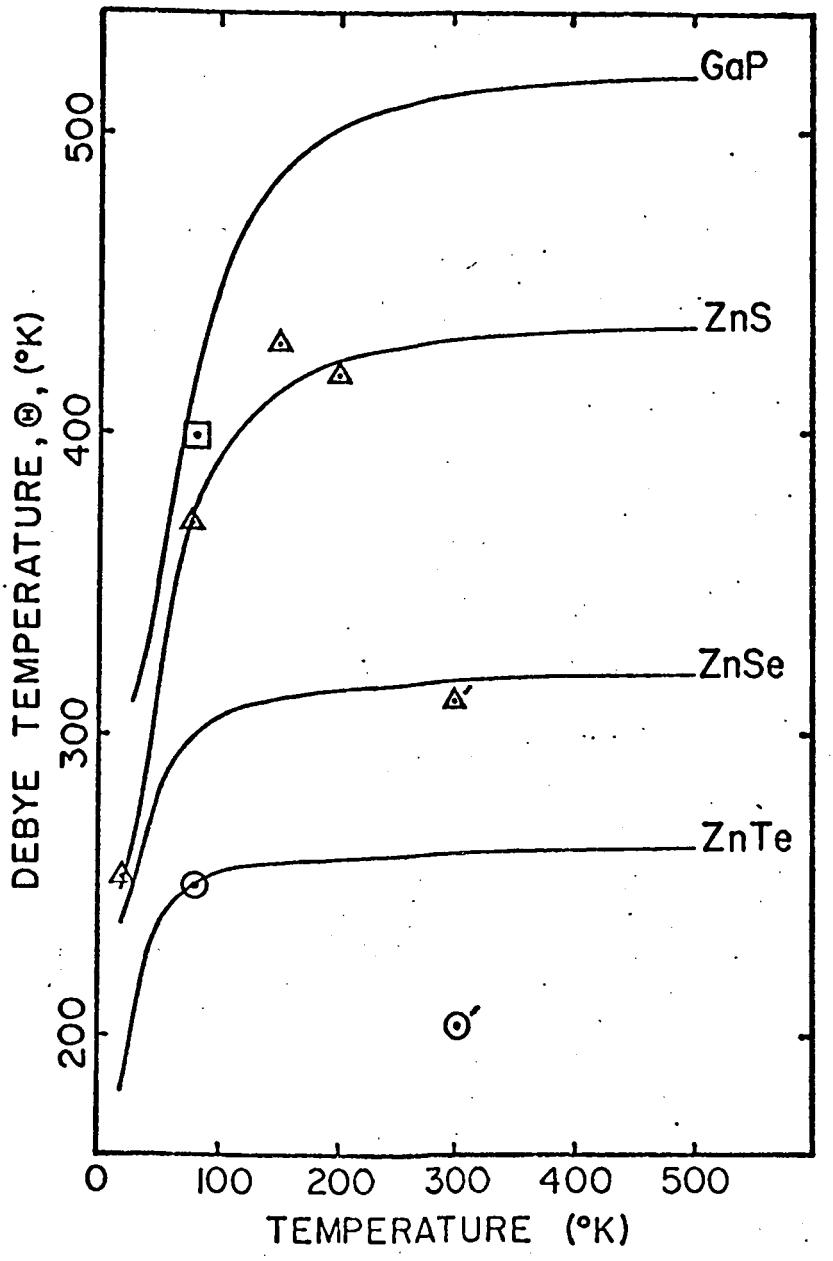

Figure 33 - The calculated and measured specific heats of ZnTe, ZnSe, ZnS and GaP. ▲ ZnS from Gmelin (1956); ◬ ZnS from Schleiger and Webb (1968); ⊙ ZnTe from Gul'tyaev and Petrov (1959); ⊙′ ZnTe from Kelemen et al. (1965) and ⊡ ZnSe from Gul'tyaev and Petrov (1959).

From Table XX it can be seen that the Debye temperatures agree for ZnTe; however the values of specific heat differ by a factor of two for the same measurement. This suggests that the meaning of the term "gm-atom" used by Gul'tyaev and Petrov differs by a factor of two from the meaning of "mole" used here. However, in the case of ZnSe there is no agreement either in the Debye temperature at 80°K or the specific heat even with consideration of a different meaning for "gm-atom". Similarly a large difference is observed between the room temperature determination of Θ for ZnTe obtained by Kelemen et al. (1965) and the calculated value obtained here.

The measurements of the specific heats of the materials studied here are few. Until recently, of the material studied here, only good crystalline samples of ZnS were available and for ZnS there is some agreement between the measured and calculated specific heats presented here. There has been poor agreement for the other materials probably due to a lack of high purity samples. The calculation of specific heats should not be sensitive to details in the phonon dispersion and it is expected that the theoretical calculations of specific heat should be accurate to about 10%. It is felt that the results presented here are closer to the real values of specific heat than those published measurements which disagree with these calculations.

CHAPTER 9

CONCLUDING REMARKS

9.1 Summary and Conclusions

A study of the Raman spectra of ZnTe, ZnSe, and GaP has been presented in this work. The spectra have been interpreted in terms of combinations and overtones from the critical points X, L, W, and Γ in the Brillouin zone. In addition the results have been analysed with the aid of the S.N.I. model which has been found applicable to zincblende materials (Banerjee and Varshni, 1969). For each material a set of critical point frequencies has been obtained that are consistent with both the theoretical model and the observed spectrum.

In the case of ZnSe it has also been possible to investigate the polarization properties of the second order spectrum. For a given crystal orientation and polarization of the incident and scattered light only certain combinations are allowed from the various critical points. These have been predicted from group theory by Krauzman, 1969 and Nilsen, 1969b, and the observed spectra have been compared to these predictions. It was concluded that the information obtained from polarization measurements was insufficient to be used alone in making mode assignments. However, the use of various polarizations and crystal orientations did aid in separating out the different contributions, and tended to verify the assignments made from the polycrystalline ZnSe spectrum.

As a further check on the reliability of the values obtained for the critical point frequencies the results were compared to regularities previously observed in the zone boundary frequencies of zincblende semiconductors (Mitra, 1963; Keyes, 1962 and Marshall and Mitra, 1964). In all cases good agreement was obtained and a number of previous inconsistencies were resolved.

The set of critical point frequencies in turn determined the parameters involved in the S.N.I. model and enabled a calculation of the phonon dispersion throughout the Brillouin zone. This calculation was carried out on an IBM 360 computer for four materials: ZnTe, ZnSe, GaP, and ZnS. Only in the case of GaP was it possible to make a detailed comparison with directly measured dispersion curves (Yarnell et al., 1968). In this case some discrepancies were found which exceeded the quoted error assignments. It is felt however that the error limitation of the GaP neutron results are somewhat optimistic in that the measurements were performed on a crystal that was fabricated from several small platelets. The only other zincblende semiconductor which has been investigated by neutron scattering in detail is GaAs (Waugh and Dolling, 1963). However the second order Raman spectrum has yet to be measured because of the lack of a suitable source and the weakness of the second order spectrum.

The frequency distribution of the vibrational modes and the specific heat as a function of temperature have been

calculated from the phonon dispersion curves for the four materials. A comparison was made with the limited amount of experimental information that is available (Gul'tyaev and Petrov, 1959; Kelemen et al., 1965; Schleiger and Webb, 1968 and Gmelin, 1956). However because of the lack of experimental specific heat data for these compounds no definitive conclusions could be drawn.

In conclusion it is felt that a method has been developed whereby reliable values can be obtained for critical point phonon frequencies in zincblende semiconductors. These values then enable one to obtain reasonably accurate (5%) estimates for phonon frequencies throughout the Brillouin zone by using an appropriate theoretical model. The results are of particular interest in the case of zincblende semiconductors where in general suitable crystals are not available for neutron scattering experiments.

9.2 Suggestions for Further Work

Obviously future experiments can be concerned with the investigation of other materials of the same class, of which there are many. However it is felt that more work should go into the further validation and improvement of the method described in this thesis. In line with this one should consider experiments on specific heat measurements. Large polycrystalline samples suitable for such experiments are now available and the results would be of general as well as particular interest.

The most accurate neutron work has been done on GaAs for which large single crystals are available. It would thus be of interest to perform scattering experiments on GaAs and to compare the results with the neutron data. Such experiments would provide a definitive test of the method and would provide information on the relative amounts of scattering that originates from critical points in the Brillouin zone. However, a source with about an 8500Å wavelength is required. It will perhaps be necessary to perform the experiments at fairly low temperatures using a GaAs laser as a source.

Finally it should be mentioned that the S.N.I. model probably does not constitute the ideal theoretical model. It is desirable to have a model with even fewer parameters which would give an even more exact description of the dispersion relations. Some work is being directed towards this end (Vetelino and Mitra, 1969) and hopefully a simple, reliable theoretical model will ultimately emerge.

APPENDIX

In this appendix the method used to obtain the selection rules for two phonon Raman processes is briefly outlined.

Consider the critical point X. The point group of the space group is D_{2d} and the reducible representation of the vibrational modes at this point is $X_1+X_3+2X_5$ (Poulet, 1955 and Parmenter, 1955) where X_1, X_3 and X_5 and irreducible representations of the group D_{2d}. X_5 is doubly degenerate and is associated with each of the optical and acoustical transverse modes. Group theory is unable to make a more precise assignment as to which of X_1 or X_3 is the optical or acoustical longitudinal so let X_1 designate the LA mode and X_3 the LO mode at X.

Similarly the point group at L is C_{3v} and the reducible representation of the vibrational modes at L is $2L_1+2L_3$. L_3 is a doubly degenerate irreducible representation and so is assigned to each of the transverse modes and L_1 to each of the longitudinal modes. At W the point group is S_4 and the reducible representation of the vibrational modes at W is $W_1+2W_2+2W_3+W_4$, where W_3 and W_4 are degenerate by time-reversal symmetry. These modes can no longer be divided into purely longitudinal or transverse polarized modes at the critical point W (Parmenter, 1955).

The point group of the space group of each critical point in the B.Z. (see Figure 3) is listed in column 2 of Table XXI. The character table for each of these point groups is found in Table XXII. The symmetry species of the lattice vibrations for each symmetry point in the B.Z. have been derived by Poulet (1965) and the reducible representation of these lattice vibrations for each of these critical points are listed in column 3 of Table XXI in terms of the irreducible representations of the appropriate point group of Table XXII.

TABLE XXI

The reducible representation of the point group at each critical point of the B.Z.

Symmetry Point	Point Group	Reducible Representations of Symmetry Species at Each Critical Point
Γ	T_d	$2\Gamma_{15}$
X	D_{2d}	$X_1+X_3+2X_5$
L	C_{3v}	$2L_1+2L_3$
W	S_4	$W_1+2W_2+2W_3+W_4$

TABLE XXII

The character tables of the point groups in zincblende.

Γ	T_d	E	$8C_3$	$6\sigma_d$	$6S_4$	$3S_4^2$
Γ_1	A_1	1	1	1	1	1
Γ_2	A_2	1	1	-1	-1	1
Γ_{12}	E	2	-1	0	0	2
Γ_{15}	F_2	3	0	1	-1	-1
Γ_{25}	F_1	3	0	-1	1	-1

L	C_{3v}	E	$2C_3$	$3\sigma_v$
L_1	A_1	1	1	1
L_2	A_2	1	1	-1
L_3	E	2	-1	0

X	D_{2d}	E	$2S_4(z)$	S_4^2	$2C_2$	$2\sigma_d$
X_1	A_1	1	1	1	1	1
X_2	A_2	1	1	1	-1	-1
X_3	B_2	1	-1	1	-1	1
X_4	B_1	1	-1	1	1	-1
X_5	E	2	0	-2	0	0

W	S_4	E	S_4	C_2	S_4^2
W_1	A_1	1	1	1	1
W_2	A_2	1	-1	1	-1
W_3	E	1	-i	1	i
W_4	E	1	i	-1	-i

The symmetry properties of the two phonon states can be derived from one phonon symmetry properties by reducing the direct product representation of the corresponding one phonon states. For example, consider the 2LO(L) overtone. The LO(L) mode has the irreducible representation L_1. The 2LO(L) state has the representation $L_1 \otimes L_1$. This representation is reducible in terms of the T_d point group to $\Gamma_1 + \Gamma_{15}$ so that the 2LO(L) phonon mode will have the symmetry species $\Gamma_1 + \Gamma_{15}$. For the zincblende crystal structure with its T_d point group symmetry, the polarizability tensor transforms as $\Gamma_1 + \Gamma_{12} + \Gamma_{15}$. In order that a two phonon process be Raman active, there must exist an irreducible representation corresponding to the irreducible representations of the polarizability tensor in the reduction of the direct product representation of the two phonon mode. Since the representation of the 2LO(L) phonon process is $\Gamma_1 + \Gamma_{15}$, it is allowed. In fact Birman (1963) finds that all two phonon processes are Raman active in the zincblende structure.

The selection rules are summarized in Table V. The reducible representation of the two phonon states at each critical point in the B.Z. have been derived and expressed in terms of the irreducible representations of the point group T_d (Birman, 1963 and Krauzman, 1969) and are listed in Column 6 of Table V. Similar results are shown for the second order infra-red absorption processes for the purpose of comparison.

LIST OF REFERENCES

Aten, A.C., Van Doorn, C.F. and Vinck, A.T., 1962. Proceedings of the International Conference on the Physics of Semiconductors, Exeter 1962 edited by A. C. Strickland (The Institute of Physics of The Physical Society, London), p. 696.

Aven, M., Marple, D.T.F., and Segall, B. 1961. J. Appl. Phys. 32, 2261.

Banerjee, R. and Varshni, Y.P. 1969. Can. J. Phys. 47, 45.

Barker, A.S. Jr. 1968. Phys. Rev. 165, 917.

Berlincourt, D., Jaffe, H., and Shiozawa, L.R. 1963. Phys. Rev. 129, 1009.

Birman, J.L. 1963. Phys. Rev. 131, 1489.

Blackman, M. 1937. Proc. Roy. Soc., A 149, 117.

Blackman, M. 1958. Phil. Mag. 3, 831.

Born, M. and von Kármán, T. 1912. Phys. Zeit., 13, 297.

Born, M. and Huang, K. 1954. Dynamical Theory of Crystal Lattices (Oxford University Press, New York) p. 255.

Braunstein, R., Herman, F. and Moore, A.R. 1958. Phys. Rev. 109, 695.

Brockhouse, B.N. 1961. Inelastic Scattering of Neutrons in Solids and Liquids, IAEA, Vienna, 113.

Brout, R. 1959. Phys. Rev. 113, 43.

Burstein, E. 1964. In Phonon and Phonon Interactions, edited by T.A. Bak (W.A. Benjamin, Inc. New York), p. 276.

Buyers, W.J.L. and Smith, T. 1966. Phys. Rev., 150, 758.

Cochran, W. 1959. Proc. Roy. Soc., A 253, 260.

Cochran, W. 1966. Phonons in Perfect Lattices and Lattices with Point Imperfections (Oliver and Boyd, Edinburgh) p. 153.

Cowley, R.A. 1962. Proc. Roy. Soc. (London) A268, 109, 121.

Cowley, R.A. 1969. Modern Solid State Physics, 2, (Gordon and Breach, New York) p. 43.

Dean, P.J. 1967. Phys. Rev. 157, 655.

Dick, B.G. and Overhauser, A.W. 1958. Phys. Rev., 112, 90.

Feldkamp, L.A., Venkataraman, G., and King, J.S. 1969. Solid State Communications 7, 1571.

Fray, S., Johnson, F.A., Jones, R., Kay, S., Oliver, C.J., Pike, E.R., Russell, J., Sennett, C., O'Shaughnessy, J. and Smith, C., 1969. In Light Scattering Spectra of Solids, edited by G.B. Wright (Springer and Verlag Inc., New York) p. 139.

Gmelin. 1956. Handbuch du Anorganischin Chemie. Zink. Weinheim, Verlag Chemie.

Gul'tyaev, P.V. and Petrov, A.V. 1959. Fiz, Tverd. Tela. 1, 368. (English Translation, Soviet Physics-Solid State 1, 330 (1959).)

Hobden, M.V. and Russel, J.P. 1964. Phys. Letters, 13, 39.

Hopfield, J.J., Thomas, D.G. and Lynch, R.T. 1966. Phys. Rev. Letters 17, 312.

Huntington, H.B., 1958, Solid State Physics, 7, 214.

Irwin, J.C. 1970. Can. J. Phys., 48, 2477.

Irwin, J.C. and La Combe, J.L. 1970a. J. Appl. Phys. 41, 1444.

Irwin, J.C. and La Combe, J.L. 1970b. Can. J. Phys. 48, 2499.

Iveronova, V.I., Parangtopo and Zvyagina, A.P. 1967. Soviet Physics - Solid State, 9, #6, 1265.

Johnson, F.A. 1965. Progr. Semicond. 9, 179.

Kaplan, H. and Sullivan, J.J. 1963. Phys. Rev. 130, 120.

Kelemen, F., Cruceanu, E. and Niculescu, D. 1965. Phys. Status Solidi, 11, 865.

Kellerman, E.W. 1940. Phil. Trans. Roy. Soc. London, A238, 513.

Keyes, R.W. 1962. J. Chem. Phys. 37, 72.

Kittel, C. 1967. Intro. to Solid State Physics (J. Wiley & Sons, Inc., New York) p. 178.

Kleinman, D.A. and Spitzer, W.G. 1960. Phys. Rev. 118, 110.

Krauzman, M. 1967. C.R. Acad. Sc. Paris B264, 1117.

Krauzman, M. 1969. Ph.D. Thesis. Faculty of Sciences of Paris, Paris, France.

Loudon, R.A. 1964. Advances in Physics 13, 423.

Lyddane, R.H., Sachs, R.G., and Teller, E. 1941. Phys. Rev. 59, 673.

Malm, H.L. and Haering, R.R., 1971. Can. J. Phys. (to be published).

Marple, D.T.F. 1964. J. Appl. Phys. 35, 539.

Marshall, R. and Mitra, S.S. 1964. Phys. Rev. 134, 1019.

Maskkevich, V.S. and Tolpygo, K.D. 1957. Zh. Eksperim i Teor. Fiz. 32, 520 (Translation: Soviet Physics - JETP 5, 435 (1957)).

Merten, L. 1958. Z. Naturforsch. 13a, 662, 1067.

Merten, L. 1962. Z. Naturforsch. 17a, 174, 216.

Mitra, S.S. 1963. Phys. Rev. 132, 986.

Mooradian, A. and Wright, G.B. 1966. Phys. Rev. Letters. 16, 999.

Nahory, R.E. and Fan, H.Y. 1967. Phys. Rev. 156, 825.

Narita, S., Harada, H. and Nagasaka, K. 1967. J. Phys. Soc. Japan, 22, 1176.

Nilsen, W.G. 1969a. Light Scattering Spectra of Solids, edited by G.B. Wright (Springer Verlag Inc., New York), p. 129.

Nilsen, W.G. 1969b. Phys. Rev. 182, 838.

Parmenter, R.H. 1955. Phys. Rev. 100, 573.

Phillips, J.C. 1956. Phys. Rev. 104, 1263.

Piper, W.W. and Polich, S.J. 1961. J. Appl. Phys. 32, 1278.

Pope, N.K. 1965. Lattice Dynamics, edited by R.F. Wallis (1963) (Pergamon Press, London) p. 147.

Poulet, H. 1955. Ann. Phys. (Paris) 10, 908.

Poulet, H. 1965. J. de Physique, 26, 684.

Riccius, H.D. 1968. J. App. Phys. 39, 4381.

Rosenstock, H.B. 1963. Phys. Rev. 129, 1959.

Rosenstock, H.B. 1965. Lattice Dynamics, edited by R.F. Wallis (Pergamon Press, Inc., New York), p. 205.

Rosenstock, H.B. and Blanken, G. 1966. Phys. Rev. 145, 546.

Russel, J.P. 1965. J. de Physique, 26, 620.

Schleiger, E.R. and Webb, L.A. 1968. Appl. Optics, 7, 33.

Smith, H.M.J. 1948. Phil. Trans. Roy. Soc. London A241, 105.

Szigeti, B. 1949. Trans. Faraday Soc. 45, 155.

Taylor, W. 1967. Physics Letters 24A, 556.

Tolpygo, K.B. 1961. Fiz. Tverd. Tela, 3, 943. (Translation: Soviet Physics - Solid State 3, 685 (1961).)

Ushioda, S., Pinczuk, A., Taylor, W., and Burstein, E. 1967 II-VI Semiconducting Compounds, 1967 International Conference edited by D.G. Thomas. (W.A. Benjamin Inc., New York) p. 1185.

Van Hove, L. 1963. Phys. Rev. 89, 1189.

Vetelino, J.F. and Mitra, S.S. 1969. Phys. Rev. 178, 1349.

Walker, C.B. 1956. Phys. Rev., 103, 547.

Waugh, J.L.T. and Dolling, G. 1963. Phys. Rev. 132, 2410.

Yarnell, J.L., Warren, J.L., Wenzel, R.G. and Dean, P.J. 1968. Neutron Inelastic Scattering, I.A.E.A. (Copenhagen Conference) 1, 301.